Chapter 6

Thermodynamic analysis of mechanisms controlling interfacial $Ce_{0.9}Gd_{0.1}O_{2-y}$ nanostructures formation

Experimental evidence has already been given in last chapter about structural details and kinetic distinctiveness between interfacial CGO nanodots and nanowires. It has been found that their particular crystallographic orientation is one of the most outstanding and distinguishing features determining their contrasted morphology and evolution path. However, despite some suggestions were pointed out, further theoretical analyses are required to understand the mechanisms governing the different behaviours observed. A thermodynamic study of the energetic contributions involved in the formation of interfacial nanoislands is going to provide further comprehension of the system, their differences and origin.

A general overview of the state-of-art of present knowledge and established background of islands' formation and evolution was already depicted in the introductory chapter. Up to now, these energetic models have been essentially applied to describe interfacial nanoislands in the semiconductor field; however, their generality also provides a functional tool to study strain-induced oxide nanostructures.

In this chapter, we base on approximate equations for the surface energy and the elastic relaxation energies of dislocation-free strained-islands derived from continuous elastic theory. The study of the total island's energy of (001) and (011)-oriented CGO nanostructures will provide information about their equilibrium shape and their sizes. At the end, several kinetic mechanisms are proposed to explain the ultrafast kinetics of (011)-nanoislands.

6.1 Energy of interfacial nanoisland's

The total energy E of an island can be calculated, accordingly to almost all the existing models, as the sum (see also chapter 1)

$$E = E_{surf} + E_{elast} + E_{edges} + E_{inter} \quad \textbf{Eq. 6-1}$$

where E_{surf} is the change in surface and interface energy, E_{relax} is the elastic relaxation energy, E_{edges} represents the short-range contribution of edges and E_{inter} is the interaction energy between islands [15, 31, 45].

Initially, we will focus on a very dilute array of islands, which will allow us to determine the equilibrium shape of a single island. This assumption implies that the interaction between islands is negligible and, consequently, last term in Eq. 6-1 can be omitted. Then, the change in energy of a single isolated island is just described as

$$E = E_{surf} + E_{elast} + E_{edges} \quad \textbf{Eq. 6-2}$$

Our study considers the change in energy as a result of the formation of a coherent 3D island on a bare substrate with respect to the energy of a 2D layer of the same volume. We use an energetic model which assumes constant island's height. This approximation accounts for the situation where atoms arriving to the island preferentially stick to lateral facets and very rarely diffuse to island's top and, thus, island grows much faster in lateral size D than in height h. Experimental results proved that the lateral size of CGO nanoislands effectively increases more rapidly than their height. For example, effective diameter $D=(ab)^{1/2}$ of (001)CGO nanodots increases more than three times faster than its height (Fig. 5-6), and the case of (011)-nanowires is even more exaggerated. Hence, considering kinetically-limited height growth seems a reasonable approximation. At the same time, this assumption makes calculation more tractable [28]. The substrate (i.e. LAO) plus a reservoir of CGO strained to match the substrate in x and y directions is taken as energy reference; whereas the island is supposed free to relax in z. From TEM strain analysis (chapter 5) we know that CGO nanoislands might grow semi-coherently because of the generation of misfit dislocations. However, this partial relief of stresses is not expected to modify thermodynamic results derived for the case of coherent islands beyond reducing the effective values of stress tensor.

For the sake of simplicity and generality, the island is assumed to be rectangular in shape, with height *h*, short axis of width *a* and long axis of length *b*; these two last dimensions defined at half the maximum height of the nanoisland. Edge facets corresponding to the short axes are tilt an angle δ with respect to the substrate, while long axes facets are bevelled an angle θ. The island is considered truncated, since this is the most frequently observed shape for CGO nanoislands (chapter 5), though the reason of this morphology is treated in detail in subsection 6.2.2 and 6.3.2. The reference thin film is supposed to be flat with constant thickness *t*. All

parameters describing the assumed island's shape are defined in Fig. 6-1, where the dashed line indicates the film with the same island volume.

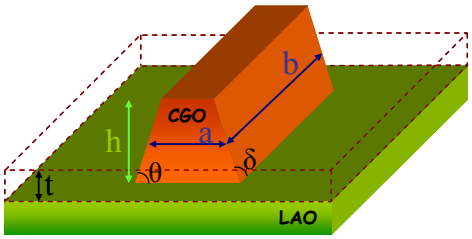

Fig. 6-1: Schematic picture of the assumed shape of a 3D island on a bare substrate. Dashed lines indicate a flat thin film with the same island volume.

Once defined the general picture of the strained island considered, let's look for the particular equations describing the energy of the island, i.e. surface energy, elastic relaxation energy and short-range contribution of edges.

6.1.1 Surface energy

As mentioned above, the surface energy term considers the change in surface energy due to the formation of a 3D island with respect to a 2D film. For the same material's volume, the surface extension is larger if material is distributed in islands than if it homogeneously covers the substrate (film). Thus, surface energy is expected to vary.

Surface energy of an island like the one drawn in Fig. 6-1 is computed as the sum of the energies corresponding to the distinct surfaces present in this configuration, where the island's volume is considered as V=abh. Then, following a similar approach to that proposed by Nie *et al.* [76]

$$E_{surf-island} = (\gamma_t + \gamma_i - \gamma_s)\,ab + \gamma_s \frac{h}{t} ab + h(-\gamma_t + \gamma_i - \gamma_s)\left[b\,cotg\theta + a\,cotg\delta\right] + 2h\left[\gamma_b\, b\,cosec\theta + \gamma_a\, a\,cosec\delta\right] \qquad \textbf{Eq. 6-3}$$

where γ_s and γ_t are the surface energy (per unit area) of the substrate and island's top facet, respectively; and γ_i is the island-substrate interfacial energy (per unit area). Lateral facets' surface energies of short and long sides are named γ_a and γ_b, respectively. No term corresponding to island's corners is considered.

If the same material volume was arranged as a 2D film of thickness *t*, its surface energy would be

$$E_{surf-film} = (\gamma_t + \gamma_i)\frac{h}{t} ab \qquad \textbf{Eq. 6-4}$$

Therefore, the change in surface energy is calculated as the difference between $E_{surf\text{-}island}$ (Eq. 6-3) and $E_{surf\text{-}film}$ (Eq. 6-4) resulting in the expression

$$E_{surf} = \gamma_1\left[\frac{h}{t}-1\right]ab + \gamma_2\left[b\,cotg\theta + a\,cotg\delta\right]h + 2h\left[\gamma_b\, b\,cosec\theta + \gamma_a\, a\,cosec\delta\right] \quad \textbf{Eq. 6-5}$$

where for compactness it is defined $\gamma_1 \equiv \gamma_s - \gamma_t - \gamma_i$ and $\gamma_2 \equiv \gamma_i - \gamma_t - \gamma_s$.

This equation can be rewritten in terms of island's effective diameter $D=(a\cdot b)^{1/2}$ and its lateral aspect ratio $c=(b/a)^{1/2}$. Consequently, the surface energy contribution is rearranged as the sum of the three terms

$$E_{surf} = E_{S-1} + E_{S-2} + E_{S-3} = \\ = \gamma_1\left[\frac{h}{t}-1\right]D^2 + \gamma_2\, hD\left[c\,cotg\theta + \frac{1}{c}cotg\delta\right] + 2hD\left[\gamma_b c\,cosec\theta + \gamma_a\frac{1}{c}cosec\delta\right] \quad \textbf{Eq. 6-6}$$

where the first term (E_{s-1}) represents the change in surface energy of flat surfaces, whereas the second (E_{s-2}) and third (E_{s-3}) terms reflect the change due to the creation of island's facets. Both Eq. 6-5 and Eq. 6-6 are very general expressions, applying to both (001) and (011)-oriented CGO islands.

In subsequent analysis, LAO substrate is supposed to be LaO-terminated; so, $\gamma_s = \gamma_{LaO} = 1.37$ J/m^2 [177]. However, following results are not dependent on this particular value; equivalent results would be achieved if AlO-termination with $\gamma_s = \gamma_{AlO} = 1.79$ J/m^2 was considered. For CGO, data referring to CeO_2 relaxed surfaces were used since no large energetic differences are expect due to Gd-doping because nearly no change in the fluorite structure and lattice parameter turns out. CeO_2 surface energy values derived by Conesa *et al.* [248] based on molecular dynamics were used for coherence with LAO data obtained from similar methods. The energy density of an interface is commonly less than the sum of the free surfaces energies of the two materials bonded at the interface [11]. So, it is not expected to strongly modify parameters γ_1 and γ_2 and even less their sign. Consequently, in next analyses, interface energy is considered negligible respect to other energetic contributions. The energetic data used as well as island characteristics (lateral and top facet planes) defining (001) and (011)CGO nanoislands are summarized in Table 6-1. In agreement with experimentally determined island's sizes and densities (AFM, TEM), the equivalent deposited thickness is computed to be *t*~0.5 nm, value kept constant in all following studies.

Table 6-1: Edge angles and surface energy values of (001) and (011)-orientated CGO nanoislands [76, 248].

CGO-Island orientation	θ (°)	δ (°)	γ_{top} (J/m^2)	γ_b (J/m^2)	γ_a (J/m^2)	γ_1 (J/m^2)	γ_2 (J/m^2)
(001)	54.7	54.7	3.25	$=\gamma_{111}$ =1.54	$=\gamma_{111}$ =1.54	-1.88	-0.5
(011)	35	45	2.45	$=\gamma_{111}$ =1.54	$=\gamma_{001}$ =3.25	-1.08	-3.82

6.1.2 Elastic relaxation energy and short-range contribution of edges

In heteroepitaxial systems, owing to the discontinuity of the intrinsic surface stress tensor and the difference in lattice parameter between the two phases coherently conjugated, the island grows surrounded by a strain field. The island exerts a force on the surface which elastically deforms the substrate. Misfit between the island and the substrate results in elastic-force monopoles *f* along island's periphery. As a result, island's elastic energy decreases at expenses of strain increase in the substrate (see also chapter 1) [15, 42, 68, 264].

Tersoff and Tromp [28] derived a good approximation for the relaxation energy of an interfacial island considering that strain ε does not change in z direction within the island, i.e. $\varepsilon_{xz}= \varepsilon_{yz}=0$. That is a fine estimation provided that a>>h and b>>h, condition which applies to both CGO nanodots and nanowires. Taking the substrate plus a reservoir of deposited material strained to match the substrate in x-y directions as energy reference, the energy change due to elastic relaxation can be expressed as

$$E_{elast} = -\frac{1}{2}\int dx\,dx'\chi_{ij}(x-x')f_i(x)f_j(x') \qquad \textbf{Eq. 6-7}$$

where the elastic Green's function of the surface χ describes the linear response to the applied force densities $f_i=\partial_j\sigma_{ij}$ at the surface; x and x' are two-dimensional vectors. The 2D island stress tensor is given by $\sigma_{ij} = \sigma_{ab}\cdot h(x)\cdot\delta_{ij}$, where σ_{aa} and σ_{bb} are the xx and yy components of the bulk stress tensor of an island strained to fit the substrate x and y lattice parameter, and free to relax in z. Variations of σ as the island relaxes are higher-order effects which were neglected. The height of the island at position x is given by h(x). Tersoff and Tromp solved Eq. 6-7 considering an isotropic solid, i.e. $\sigma_{aa}= \sigma_{bb}$, which leaded to Eq. 1-6; terms involving corners were neither considered. However, in a generalized equation applying to both wires and dots we should consider a biaxial anisotropic stress, i.e. $\sigma_{aa} \neq \sigma_{bb}$. Therefore, we introduce the coefficient β to tune the anisotropy strain ratio between both in-plane growing directions. Thus, the elastic strain energy can be written as

$$E_{elast} = -\alpha\left\{a\,ln\left(\frac{b}{A_o}\right)+\beta\,b\,ln\left(\frac{a}{A_o}\right)\right\} \qquad \textbf{Eq. 6-8}$$

where A_o is a cut-off length in the range of some characteristic length of the system and proportional to the height of the island [28]. Whereas the anisotropic strain parameter β is a dimensionless coefficient measuring the relation between force monopoles along long and short axes, α has units of J/m and depends on island's height ($\alpha \sim h^2$) as well as on elastic parameters of the substrate such as Poisson's ratio ν or shear modulus μ.

For lattice-mismatched systems with edge-side facets, the always positive short-range contribution of edges must also be considered (see also chapter 1) [15, 43]. In literature, it was pointed out that this short-range contribution of the edges can be incorporated into the elastic relaxation energy equation through a renormalization of the length parameter A_o [15, 43, 76]. Hence, the elastic strain energy plus the short-range contribution of the edges takes the form

$$E_{relax} = E_{elast} + E_{edges} = -\alpha\left\{a\,ln\left(\frac{b}{A}\right) + \beta\, b\, ln\left(\frac{a}{A}\right)\right\} \qquad \textbf{Eq. 6-9}$$

where we consider the renormalized parameter A as a fitting parameter.

Eq. 6-9 can also be rewritten in terms of the island effective diameter $D=(ab)^{1/2}$ and its lateral aspect ratio $c=(b/a)^{1/2}$. Then, $E_{elast}+ E_{edges}$ is expressed as

$$E_{relax} = E_{elast} + E_{edges} = -\alpha\, D\left\{\frac{1}{c}ln\left(\frac{c\,D}{A}\right) + \beta\, c\, ln\left(\frac{D}{c\,A}\right)\right\} \qquad \textbf{Eq. 6-10}$$

From hereafter, the short-range contribution of edges will be implicitly included in the elastic relaxation energy.

6.1.3 Energy of an interfacial isolated island

Consequently, the total energy of a single island in a dilute array of islands can be expressed in terms of its lateral axes a and b as

$$E = E_{surf} + E_{relax} + E_{edges} = \gamma_1\left[\frac{h}{t} - 1\right]ab + \gamma_2\left[b\,cotg\theta + a\,cotg\delta\right]h$$
$$+ 2h\left[\gamma_b\, b\, cosec\theta + \gamma_a\, a\, cosec\delta\right] - \alpha\left\{a\,ln\left(\frac{b}{A}\right) + \beta\, b\, ln\left(\frac{a}{A}\right)\right\} \qquad \textbf{Eq. 6-11}$$

or as function of its effective diameter $D=(ab)^{1/2}$ and lateral aspect ratio $c=(b/a)^{1/2}$.

$$E = E_{surf} + E_{relax} + E_{edges} = \gamma_1\left[\frac{h}{t} - 1\right]D^2 + \gamma_2\, hD\left[c\,cotg\theta + \frac{1}{c}cotg\delta\right]$$
$$+ 2hD\left[\gamma_b\, c\, cosec\theta + \gamma_a\,\frac{1}{c}cosec\delta\right] - \alpha D\left\{\frac{1}{c}ln\left(\frac{c\,D}{A}\right) + \beta\, c\, ln\left(\frac{D}{c\,A}\right)\right\} \qquad \textbf{Eq. 6-12}$$

These general expressions apply to both (001) and (011)-oriented CGO nanoislands. However, a detailed analysis is required to distinguish how these crystallographic orientations can drive to distinct shapes and evolution behaviours.

6.2 Interfacial (001)CGO nanostructures

Let's initially focus on (001)CGO nanoislands on a LAO substrate, which are isomorphic square in shape (i.e. c=1) as it was experimentally observed in last chapter 5. One of the most striking features of these dots is that, in general, they remain isomorphic and with nearly constant volume at least for the explored annealing times under typical oxidizing atmosphere. Thus, first step is to investigate their in-plane equilibrium shape through thermodynamic analysis. Afterwards, coarsening behaviour will be studied.

6.2.1 Equilibrium shape of (001)CGO nanostructures

Study of the equilibrium morphology is rather complex if continuous exchange of atoms between islands is permitted, i.e. island's volume is not fixed. Therefore, we must focus on constant island's volume (i.e. D=ct., h=ct.). The study of island's energy as function of its lateral anisotropy $c= (b/a)^{½}$, i.e. curves E(c), provides information about in-plane configurations of lowest energy at constant island's volume.

In subsequent sections, we first analyze separately the dependence of surface energy and elastic relaxation energy on lateral aspect ratio c. Then, the total energy of the island is investigated in order to determine the equilibrium island shape given a fixed volume, assuming that diffusion within the island is not a problem to achieve this shape.

6.2.1.1 Surface energy as function of lateral anisotropy *c* for (001)-nanoislands

TEM images demonstrated that (001)CGO nanoislands are truncated pyramids with flat (001) top facet surface and (111) planes in all four lateral facets. Consequently, the surface free energy described in Eq. 6-6 simplifies since $\gamma_a= \gamma_b= \gamma_{111}$ and $\theta=\delta$,

$$E_{surf} = E_{S-1} + E_{S-2} + E_{S-3} = \\ = \gamma_1\left(\frac{h}{t}-1\right)D^2 + \gamma_2\, h\, D\, cotg\theta\left(c+\frac{1}{c}\right) + 2\,\gamma_{111}\, h\, D\, cosec\theta\left(c+\frac{1}{c}\right) \qquad \textbf{Eq. 6-13}$$

where γ_1=-1.88 J/m^2, γ_2=4.62 J/m^2, γ_{111}=1.54 J/m^2 and θ=54.7^o. Fig. 6-2 shows a generic curve of the surface energy dependence with lateral aspect ratio c of a (001)CGO nanoisland on a LAO substrate. The contribution of distinct terms E_{s-1}, E_{s-2} and E_{s-3} is also plotted. This specific example corresponds to an island of constant size D=20 nm and height h=6 nm; the same behaviour occurs for the other islands' volumes.

The most outstanding feature observed in Fig. 6-2 is that total surface energy is negative. In general, island's formation is associated to a decrease of elastic energy at the cost of surface energy increase with respect to a 2D film (i.e., $E_{surf}>0$) [12, 60, 191]. When the trade-off between these energetic contributions results into a total reduction of the energy of the system, islands are expected to form. Therefore, in the present case, $E_{surf}<0$ indicates that there is no surface energy impediment to surmount for island's formation to happen. A closer study of E(c) dependence shows that total surface energy essentially follows the behaviour of the first term E_{S-1} of Eq. 6-13. Since $E_{S-1}<0$, E_{surf} is also negative. This term mainly represents the change in surface energy of flat surfaces. Thus, besides the ratio between island's height and equivalent deposited thickness, just (001)-substrate surface energy and top (001)-CGO facet surface energy (and interface energy between both structures) are involved in this term. Hence, the use of highly dilute solutions (h/t>1) together with the particular combination of surface energies of (001)-LAO substrate and (001)-CGO result into a very singular system where total surface energy already favours island's formation. So, choosing the appropriate materials, i.e. substrate and deposited structure, the general extended idea that island's creation implies a cost of surface energy can be inverted and turn into a further reduction of total energy of the system. The possibility of surface energy gain through island formation was already considered by Shchukin et *al.* [15]; who described the case of a InAs pyramid with {101} side facets in Stranski-Krastanov configuration on (001)GaAs substrate.

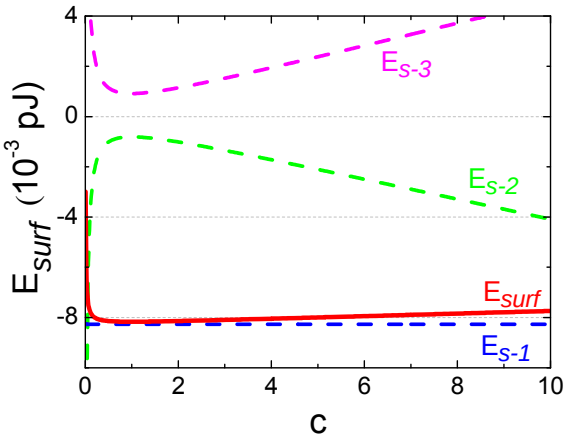

Fig. 6-2: Surface energy (—) as function of lateral aspect ratio $c=(b/a)^{½}$ for a (001)CGO nanoisland on a LAO single-crystal substrate. Different contributions to surface energy are also plotted: E_{S-1} (—), E_{S-2} (—) and E_{S-3} (—). Fixed island size D=20 nm and h=6 nm was considered.

In Fig. 6-2, it is also observed that there exists a surface energy minimum at $c_{eq}=1$ and, then, E_{surf} increases if (001)CGO nanoisland elongates (=c increase or decrease), independently of the in-plane direction. To easily observe this behaviour and to study in more detail the influence of E_{surf} on island's anisotropy, the dominating contribution E_{S-1} can be omitted, since it is not function of the lateral aspect ratio c. Fig. 6-3 shows the dependence of $E_{S-2}+E_{S-3}$ as

function of lateral anisotropy c for different islands' volumes. Distinct island's volumes were computed assuming a constant island height and different sizes D. The existence of a minimum of surface energy at c=1 independently of island's volume indicates that in-plane isomorphic shape (a=b) is the optimum morphology for (001)CGO nanoislands from a surface energy point of view. For any other configuration (c>1 or c<1), (001)-nanodots would increase their surface energy. The physical origin behind these results is the equivalence between the four (111) lateral facets of the (001)CGO truncated pyramid. Due to this symmetry, the system would not lower its surface energy through elongation. Let's recall that the presented model does not include any term corresponding to the corners.

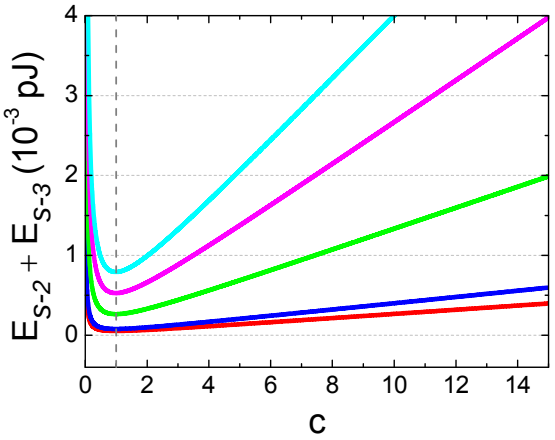

Fig. 6-3: $E_{S-2}+E_{S-3}$ dependence on lateral aspect ratio c of (001)CGO nanoislands of different sizes D= 10 (—), 25 (—), 50 (—), 100 (—) and 150 (—) nm; in all cases constant height h=6 nm was assumed. Dashed-line stresses that E_{surf} is minima at c=1 for all islands' volumes.

Hence, surface energy drives (001)CGO nanoislands on LAO substrates to an isomorphic (square) shape independently of their volume. Let's notice that despite plot in Fig. 6-3 seems to suggest that surface energy is lower for small island volumes, this behaviour is inverted when first term of Eq. 6-13 (E_{S-1}~$-D^2$) is also taken into account.

6.2.1.2 Elastic relaxation energy as function of lateral anisotropy *c* for (001)-nanoislands

(001)CGO nanoislands grow epitaxially on LAO substrates following the crystallographic orientation (001)CGO[110]||(001)LAO[100], which results in two equivalent in-plane growing directions. The lower mismatch of this epitaxial relation (ε~-1%) suggests a high coherence level. Consequently, these nanoislands grow under a cubic anisotropic strain. Just focusing on the in-plane growth along CGO[110]||LAO[100] and CGO[1-10]||LAO[010], nanodots grow under biaxial isotropic stress and, thus, force monopoles densities *f* can be considered equal along all island's periphery. This feature is introduced in Eq. 6-10 imposing

anisotropic strain parameter β=1. Therefore, elastic relaxation energy plus short-range contribution of edges takes the form

$$E_{relax} = -\alpha D\left\{\frac{1}{c} ln\left(\frac{c\,D}{A}\right) + c\, ln\left(\frac{D}{c\,A}\right)\right\} \qquad \textbf{Eq. 6-14}$$

This equation coincides with the case derived by Tersoff and Tromp (Eq. 1-6) [28], since stress tensor of (001)CGO nanoislands satisfies $\sigma_{aa} = \sigma_{bb} \equiv \sigma_A$. Thus, one can establish the equivalence

$$\alpha \approx \frac{\sigma_A^2(1-\nu)}{\pi \cdot \mu}\, h^2 \qquad \textbf{Eq. 6-15}$$

where ν is the Poisson's ratio and μ the shear's modulus. The exact value of the stress tensor is unknown; though, a rough estimation can be set as σ~Yε [15], where Y is the Young modulus and ε the lattice mismatch. Typical values for perovskite structures can be taken as ν ~ 0.3, μ ~ 80 GPa and Y~ 200 GPa [265-268]. All these considerations lead to the assessed values $\alpha \sim 10^{-9}$-10^{-10} J/m, estimation which includes typical nanoislands' height < 20 nm. The renormalized cut-off length A is considered within the range of 2-15 nm.

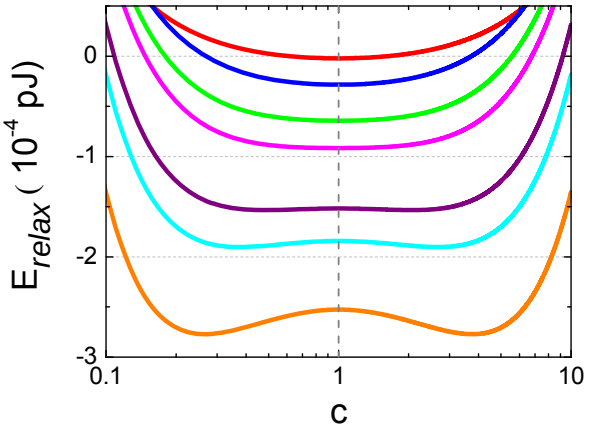

Fig. 6-4: Elastic relaxation energy plus short edge contribution of edges as function of lateral aspect ratio c for (001)CGO islands on LAO substrate. Different curves correspond to distinct island's sizes D= 10 (—), 25 (—), 40 (—), 50 (—), 70 (—), 80 (—) and 100 (—) nm; island's height was considered h=6 nm for all cases. Parameters $\alpha = 5 \cdot 10^{-10}$ J/m, β=1 and A=8 nm were used for the computation. Dashed line indicates isomorphic square shape c=1. Note that for the set of parameters considered E_{relax} enhances island's elongation for D>70 nm.

Generic curves of E_{elast} as function of lateral aspect ratio c for (001)CGO nanoislands are displayed in Fig. 6-4; distinct colour curves correspond to different islands' sizes D and constant height h=6 nm. For small sizes, the elastic relaxation energy as function of lateral aspect ratio c shows an energy minima at c=1; i.e. E_{relax} favours isomorphic shape. However, there exists a critical size D_c^{rel} above which E_{relax} promotes the elongation of the island in either of the two orthogonal directions with two degenerate minima at c and 1/c. The critical size at which $E_{relax}(c)$ drives the island from square to rectangular shape depends on the strain

(considered through parameter α), as well as on parameter A (which depends on island's height).

Hence, in contrast to surface energy, elastic relaxation energy initially favours isomorphic (square) islands' morphology and, above a critical size, E_{relax} drives the island to adopt a rectangular shape as a mechanism of strain relaxation. In-plane elongation promoted by strain relaxation energy has already been pointed out by some authors [28, 33, 66, 68]. The instigation of a spontaneous shape instability can be understood through island's perimeter [68]. In those systems where strain relaxation through vertical growth is limited, the most efficient strategy of strain relief bases on the force monopoles arising at island's periphery due to the discontinuity of the intrinsic surface stress tensor and lattice mismatch. For a given island's base area, rectangular shape ensures larger perimeter (periphery) than a square one. Hence, large islands with limited height growth can further relieve strain energy if they elongate. However, this behaviour just attains the elastic relaxation energy, and surface energy must also be considered to determine the final equilibrium shape of the interfacial nanoisland.

6.2.1.3 Total energy as function of lateral anisotropy *c* for (001)-nanoislands

After separately exploring the surface and elastic relaxation energy tendencies with respect to lateral aspect ratio c, it must be now investigated the balance between these two energy contributions in order to determine the optimum shape of (001)CGO nanoislands on LAO substrates. Fig. 6-5a shows the dependence of the total energy E *vs.* log c for a (001)CGO nanoisland of typical size D=25 nm and h=7 nm. In this plot, parameters $\alpha=5\cdot10^{-10}$ J/m, β=1 and A=8 nm were used in the computation. For this island's size and parameters α and A considered, the energy of the island shows a minimum at c=1, evidencing that isomorphic shape is the lowest energy configuration for these islands. From previous analyses, we know that for this island's size both the surface energy and the elastic relaxation energy drives the island to an isomorphic square shape.

Hence, the isomorphic shape of our (001)CGO nanodots has a thermodynamic origin. For such island's size (i.e. D=25 nm and h=6 nm), this optimum shape would be achieved at least within the parameter range 10^{-14} J/m^3< α < 10^{-7} J/m^3 and A>4. Moreover, we observe in Fig. 6-5b that the compromise between E_{surf} and E_{relax} leads to isomorphic square shape for a large range of islands' sizes. For example, for a 7 nm high island, the square shape is still the equilibrium one for lateral sizes $D=(ab)^{½}$=70 nm (dimension larger than those typically observed in (001)CGO nanodots).

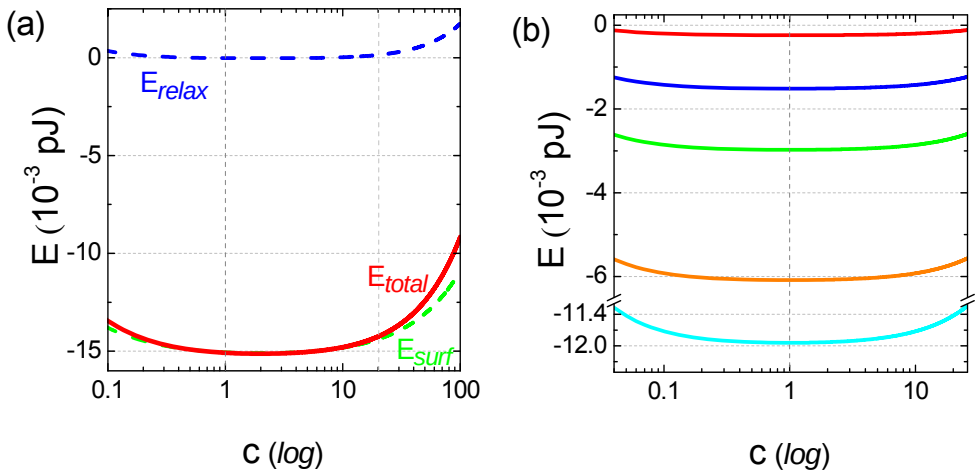

Fig. 6-5: Total energy (—) as function of the logarithm of lateral aspect ratio c of a typical (001)CGO island of D=25 nm and h=7 nm on LAO substrate; surface (---) and elastic relaxation (---) energy contributions are also plotted (a). E(c) for (001)CGO islands of sizes D=10 (—), 25 (—), 35 (—), 50 (—) and 70 (—) nm, and h=7 nm (b). Parameters $\alpha=5\cdot10^{-10}$ J/m, $\beta=1$ and A=8 were used.

Nonetheless, if some how the island can grow beyond a critical size D_c, the island would experience a spontaneous shape instability and elongation in any of the two equivalent directions would occur. Fig. 6-6 displays the energy as function of c of a (001)CGO nanoisland of size D=800 nm and h=10 nm; parameters $\alpha=2\cdot10^{-9}$ J/m, $\beta=1$ and A=8 nm were used. For this large island's size and parameters α and A considered, we observe that E(c) shows two degenerate minima and, thus, the equilibrium shape would correspond to a rectangular island with lateral aspect ratio either c (b>a) or c^{-1} (b<a). It has been observed that the lateral aspect ratio increases with increasing island effective diameter D.

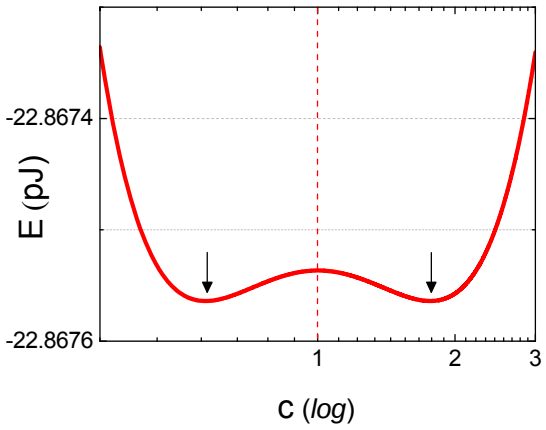

Fig. 6-6: Total energy of a (001)CGO nanoisland on a LAO substrate showing the existence of a strain-induced shape instability: elongation would occur in either of the two orthogonal directions with two degenerate minima at c=1.77 and c=0.57 (=1/1.77). This example correspond to a very large island of D=800 nm and h=10 nm; parameters $\alpha=2\cdot10^{-9}$ J/m, $\beta=1$ and A=8 nm were used for the computation.

Our experimental studies pointed out that the evolution of (001)CGO nanoislands is very slow, if not null. Moreover, there is neither continuous deposition of material in CSD-

derived system which could enable the growth of these islands beyond the critical size D_c. This is the general landscape of (001)CGO nanostructures in their standard conditions, i.e. oxidizing atmosphere and high temperature. Just under very particular growth conditions we could modify this situation. In section 5.4, nucleation of CGO nanoislands was carried out in O_2 so that most of nucleated islands were (001); further evolution was done in Ar-H_2. Despite no significant evolution was observed during first 5 h of annealing in reducing atmosphere, (001)CGO nanowires were suddenly formed after 10 h annealing. This astonishing result can now be explained because of the existence of a spontaneous shape instability after the growth beyond a critical size D_c, only possible after the heat treatment in such specific combination of growth conditions. Critical size D_c will be investigated in more detail later. Let's point out that the example displayed in Fig. 6-6 corresponds to a very large island with $D=(ab)^{1/2}$=800 nm, which illustrates the large sizes required for elongation. The strain energy is the responsible of the elongation of the islands for sizes larger than D_c. Because of the isotropy of surface energies of (001)CGO nanostructures, island adopts an isomorphic (square) shape at small sizes and would elongated for $D>D_c$. Contrasted situation will be observed for the case of (011)-nanowires, where island's surface energies are anisotropic.

Therefore, thermodynamic analyses indicate that the experimentally observed isomorphic shape of (001)CGO nanodots on LAO substrates corresponds to an energy minimum of the system for our typical islands' size and for a given set of α and A parameters. These particular parameters will be adjusted in detail in next section. So, (001)CGO nanodots seem to exhibit their equilibrium shape according to displayed sizes. We have to take into account that we are considering the energy of an isolated (001)-nanodot. Elastic interactions between islands should be studied as well to obtain a full description of the system, since they can also influence the equilibrium shape of strained islands. On the other hand, these thermodynamic analyses have also allowed us to explain the formation of extremely long (001)CGO nanowires. Nonetheless, let's remark that the formation of (001)-nanowires just occurred in a particular combination of growth atmospheres and does not represent the typical and general path followed by (001)CGO nanodots under standard conditions, which keep their isomorphic shape and fairly constant size. Thus, from now on, we will continuous to mainly focus on (001)CGO isomorphic nanodots.

6.2.2 Truncation of (001)CGO nanostructures

Analyses carried out till the moment assumed a flat ended island's shape with (001)-CGO top plane, which is in agreement with all (001)-nanodots observed in TEM cross-section images (section 5.1.1). However, in addition to results reported there, one may ask if dots are

truncated since nucleation or if flat top surfaces develop as island grows. To study this behaviour through thermodynamic analyses, dependence of elastic relaxation energy with island's height must be considered within the limits of dealing with a kinetically limited growth in h. Comparing Eq. 6-14 and Tersoff and Tromp calculations [28], one can establish the relations $\alpha=\eta h^2$ and $A=Kh$, where η includes the stress tensor and K is a fitting parameter of a typical length of the system. On the other hand, to compare the energy of non-truncated and truncated (001)-dots it must be taken into account the inexistence of flat surfaces at island's top for the former configuration, i.e. triangular cross-section. Therefore, the surface energy of a sharp-ended (001)-island limited by (111) lateral facets takes the form

$$E_{surf} = \left[\varphi_1 + \varphi_2 \frac{h}{t}\right] D^2 + hD_1 \left(\frac{1}{c} + c\right) \left[\varphi_1 \, cotg\theta + 2\,\gamma_{111}\, cosec\theta\right] \qquad \textbf{Eq. 6-16}$$

where $\varphi_1 \equiv \gamma_i - \gamma_s$ and $\varphi_2 \equiv \gamma_s - \gamma_t - \gamma_i$. According to Table 6-1 data, these parameters take the values φ_1=-1.37 J/m and φ_2=-1.88 J/m; $\eta \sim 10^7$ J/m^3 is the value corresponding to $\alpha \sim 10^{-9}$ J/m used in previous sections and determined considering $\sigma \sim Y\varepsilon$ and $\varepsilon \sim 1\%$.

Fig. 6-7 displays the total energy ($E_{surf} + E_{relax}$) dependence as function of height h of a (001)CGO nanoisland at a very initial stage of evolution; effective diameter D=4 nm was assumed. Both sharp (dashed line) and flat (solid line) configurations are plotted. Only for island's heights h < 3 nm, triangular cross-section is energetically more favourable than a flat ended island. This behaviour agrees with experimental TEM results, where the shortest observed (001)-nanodot of just 3.5 nm height is already truncated. Therefore, it justifies the assumption of considering (001)CGO nanodots as truncated islands.

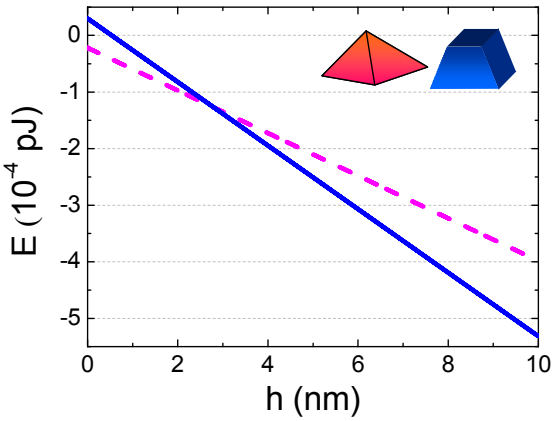

Fig. 6-7: Energy as function of height of a (001)CGO nanodot of D=4 nm and c=1 with triangular (--) and truncated (—) cross-section. Parameters $\eta=10^7$ J/m^3 and K=4 were considered.

6.2.3 Coarsening of (001)CGO nanostructures

We have proved that the isomorphic shape exhibited by (001)CGO nanodots on LAO substrates has a thermodynamic origin, i.e. it corresponds to the equilibrium shape. From

experiments, we also know that these nanoislands show pretty constant size under standard processing conditions (O_2). Therefore, we must still wonder if there exists an optimum island size. It corresponds to study the possible existence of coarsening phenomena; that is, determine if islands tend to continuously increase their volume in order to minimize the total energy of the system or not. To tackle this question we cannot restrict to a fixed island's volume; indeed, the change of energy as island's size increases has to be analyzed. Given the presented tools and without taking into account interaction between islands, one can study the dependence of the energy per unit volume (E/V) as function of the effective diameter $D=(ab)^{½}$. Since the total energy of the island computes the energy change with respect to a 2D film of the same volume, increase of islands' volume (for example, larger diameter D) simply corresponds to consider a 2D film with the same thickness (t=0.5 nm) but covering larger substrate area. The model used considers the case of kinetically-limited islands. Therefore, when studying the minimum of the energy density we are actually looking at the E/V minimum with respect to the base area.

6.2.3.1 Surface energy density as function of effective diameter *D* for (001)-nanoislands

Coarsening phenomena is in general observed to happen in particles whose surface energy is positive. Since the relation surface/volume decreases as particle's size increases, there is a continuous tendency to increase particles' volume to reduce the cost of surface energy. Although CGO/LAO is a quite particular system where $E_{surf}<0$, let's investigate if coarsening is promoted from a surface energy density point of view.

Estimating dots' volume as $V\sim hD^2$, the surface energy density of a single (001)-nanodot is

$$\frac{E_{surf}}{V}=\gamma_1\left(\frac{1}{t}-\frac{1}{h}\right)+\left[\gamma_2 cotg\theta+2\gamma_{111}cosec\theta\right]\left(c+\frac{1}{c}\right)\frac{1}{D} \qquad \textbf{Eq. 6-17}$$

Fig. 6-8 shows the dependence of E_{surf}/V with effective diameter D for different lateral aspect ratios c. For very small sizes (few unit-cells width), E_{surf}/V is positive. However, it rapidly becomes negative and continuously decreases as island's size D increases. Due to the equivalence between all four lateral facets, curve $E_{surf}/V(D)$ of an island with anisotropy c is the same of one with aspect ratio c^{-1}. Nevertheless, from previous analyses and experimental results we know that the optimum thermodynamic configuration of our (001)CGO nanodots is achieved for c=1; thus, we should restrict to this situation (green curve, plot Fig. 6-8). Isomorphic shape c=1 corresponds to the lowest E_{surf}/V configuration. Either for c>1 or c<1 the surface energy density is higher, confirming that surface energy favours an isomorphic shape. Hence, surface energy density contribution drives (001)CGO nanodots to experience infinite coarsening while keeping an isomorphic square shape.

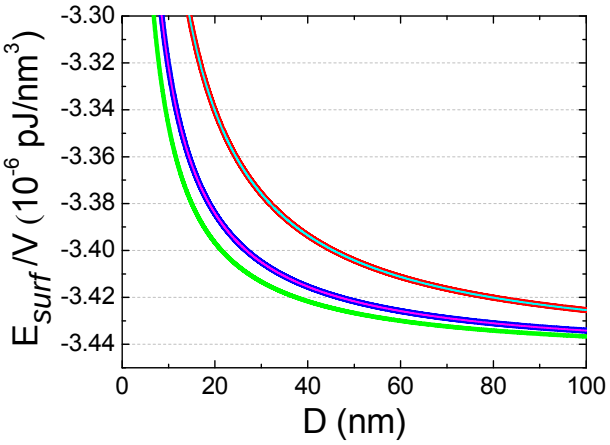

Fig. 6-8: Surface energy per unit volume as function of effective diameter D of (001)CGO nanodots on LAO substrates. Different curves correspond to lateral aspect ratios c= 0.25 (—), 0.5 (—), 1 (—), 2 (—) and 4 (—). Island height was kept constant at h=6 nm in all cases.

6.2.3.2 Elastic relaxation energy density as function of effective diameter *D* for (001)-nanoislands

The elastic relaxation energy plus short-range contribution of edges per unit volume can be written as

$$\frac{E_{relax}}{V} = -\frac{\eta\, h}{D}\left\{\frac{1}{c}ln\left(\frac{c\,D}{K\,h}\right) + c\,ln\left(\frac{D}{c\,K\,h}\right)\right\} \qquad \textbf{Eq. 6-18}$$

where β=1 is assumed. Dependences $\alpha = \eta h^2$ and A=Kh introduced in previous sections are also considered.

Fig. 6-9 shows the dependence of E_{relax}/V as function of D for different lateral aspect ratios c. Contrary to E_{surf}/V, elastic relaxation energy density shows an energy minimum given constant in-plane anisotropy c. So, island coalescence is not instigated from E_{relax}/V point of view; instead, E_{relax}/V tends to stabilize island's lateral size to an optimum size D_{opt}^{REL}

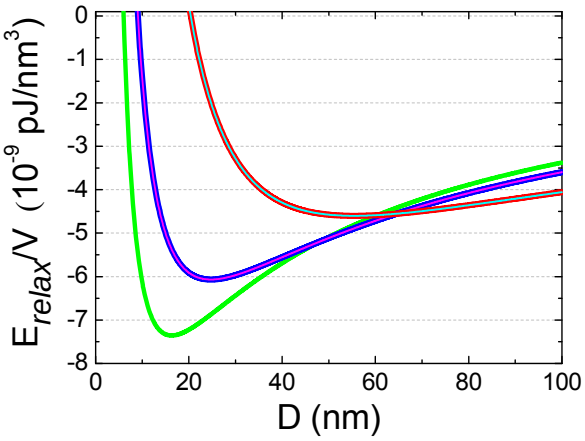

Fig. 6-9: Elastic relaxation energy density as function of effective diameter D of (001)CGO dots on LAO substrates. Different curves correspond to lateral aspect ratios of c=0.25 (—), 0.5 (—), 1 (—), 2 (—) and 4 (—). Island height was assumed constant at h=6 nm. Parameters $\eta=10^7$ J/m^3, β=1 and K= 1nm were used.

determined as the minima of elastic relaxation energy density. Given a fixed island's height, the configuration of lowest E_{relax}/V for (001)CGO nanoislands also corresponds to an isomorphic shape. Hence, elastic relaxation energy density acts against coarsening and favours a stable island size.

6.2.3.3 Energy density as function of effective diameter *D* for (001)-nanoislands

In previous sections we proved that surface energy density enhances coarsening phenomena whereas elastic relaxation energy density acts against them in (001)CGO nanoislands on LAO substrates. So, we must investigate the compromise between surface energy and strain to determine the behaviour of the system. Fig. 6-10 shows a typical curve of the total energy density of a (001)CGO dot on LAO substrate; since in standard conditions our (001)CGO nanoislands are square-based we focus on lateral aspect ratio c=1. Dots' size increases through coalescence mechanisms till they reach their equilibrium size D_{opt} and then coarsening is stopped; otherwise the system would not keep its configuration of lowest energy per atom. Hence, there exists an equilibrium island size for (001)CGO isomorphic nanodots of constant height.

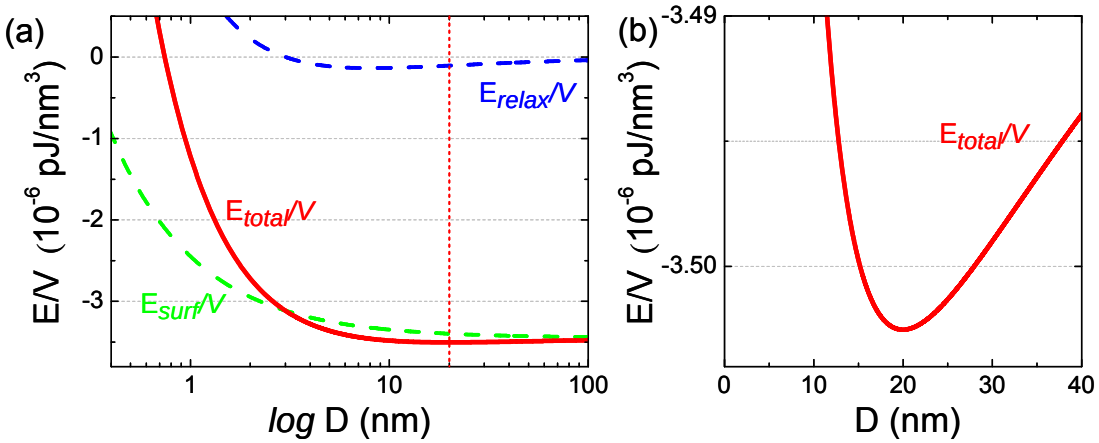

Fig. 6-10: Energy per unit volume as function of effective diameter *log* D for an isomorphic (001)CGO dot on LAO (a); and zoom of the same plot stressing the minima of energy density (b). The optimum size is determined D_{opt}=20 nm considering h=6 nm and β=1, and adjusting $\eta=10^7$ J/m^3 and K=0.5.

Experimentally, it was determined a typical (001)-dot size of D=20 nm. From our thermodynamic arguments and considering island's height of h=6.3 nm (as would correspond according to h-a relation displayed in Fig.5-6), this optimum dots' size D_{opt}=20 nm is obtained from E/V(D) curves using $\eta\sim9.3\cdot10^7$ J/m^3, and the fitting parameter K=0.5 (value of the order of CGO lattice cell). It corresponds to the plot displayed in Fig. 6-10. Considering typical perovskite values ν~0.3, μ~80 GPa and Y~200 GPa and relation σ~Yε, the corresponding lattice mismatch would be |ε|~3%. This misfit slightly differs from the value computed through the

difference of lattice parameters of CGO and LAO crystallographic structures (|ε|~1%). Distinct causes might lead to this disagreement. First of all, let's notice that we have neglected the interface energy of the CGO/LAO system and, evidently, it does not correspond to the real situation where it might play a significant role mostly taking into account that this interface is strongly defective (oxygen vacancies), as suggested by the observation of colossal interfacial ionic conductivity [159]. Other approximations made might as well influence the results. Estimation of stress tensor as σ~Yε is probably too rough and a more accurate expression would be required. Moreover, our model assumes kinetically limited nanoislands. So, minimization of energy density does not consider growth in h and relaxation in z is neither taken into account. Thus, exact dependence of elastic relaxation energy with islands' height should be explicitly calculated. Finally, let's point out that elastic and mechanical parameters considered are typical values of perovskites, but not specific of LAO single-crystal substrates.

Nonetheless, besides all these limitations and approximations, this basic and simplified model has allowed us to explain the stable uniform shape and size of isomorphic (001)-nanodots. All thermodynamic results indicate that (001)CGO nanodots on LAO substrates exhibit their equilibrium configuration. To definitely prove the stability of the array of uniform square-based (001)CGO nanoislands we should consider elastic interactions between islands. These calculations are out of the extent of the present work; even though some remarks will be pointed out in section 6.5.

6.2.4 Critical size of (001)CGO nanostructures

Isomorphic uniform-sized islands are the typical configuration observed for (001)CGO nanoislands on LAO substrates. However, our experimental results showed that under specific conditions these islands could grow beyond a critical size and adopt a highly anisotropic shape. Let's now roughly investigate the parameter region at which shape instability might occur.

Accordingly to our kinetically-limited height growth model, we can investigate the equilibrium shape at which shape instability occurs. Writing island's energy as function of ψ=arctan(b/a), because the total energy of the island is symmetric with respect to ψ, the critical size at which shape instability occurs is defined by the condition

$$\left.\frac{d^2E}{d\psi^2}\right]_{\psi=45^o} = 0 \qquad \textbf{Eq. 6-19}$$

which leads to

$$D_c = e^2 K \,\mathrm{h}\, \exp\left(-\frac{\Gamma}{\eta\,\mathrm{h}}\right) \qquad \textbf{Eq. 6-20}$$

where $\Gamma = \gamma_t \cot g\theta + \gamma_s \cot g\theta - \gamma_i \cot g\theta - 2\gamma_{111} \operatorname{cosec}\theta$, and isomorphic square (001)CGO island is considered.

Fig. 6-11 displays the calculated critical size D_c as function of h. For this example, parameters $\eta \sim 9.3 \cdot 10^7$ J/m^3 and K=0.5 determined in Fig. 6-10 were used. Continuous orange curve indicates the critical size D_c at which shape instability would occur for a given height. Below the curve, isomorphic shape is the lowest energy configuration and above it the strained island would elongate. For the specific set of parameters η and A considered, the model points out that island sizes greater than D>54 nm are at least required for a (001)CGO nanoisland of 5 nm height to experience a spontaneous shape instability. For shorter or higher islands, the critical size D_c increases. The shape of this curve is due to the dominance of the exponential part of Eq. 6-20 at lower heights, whereas for high island heights D_c is controlled by the linear h-dependence. These critical dimensions are much larger than those typically observed for the case of (001)CGO nanodots, which would explain why all our (001)CGO nanoislands grown in standard conditions are isomorphic. Let's remark that island's dimensions determined from AFM images are strongly influenced by convolution effects, specially in the case of those nanostructures with sizes similar or smaller to tip's radius. Thus, we must actually focus on nanodots' dimensions obtained from TEM images. The general lateral size D-to-height relationship experimentally determined from different TEM cross-section images is represented in Fig. 6-11 by the dashed-green line. It must be straight that this is a general D-h tendency and in fact only green star symbols at the left-bottom corner of the plot correspond to observed (001)-nanodots dimensions. For the case of $\eta \sim 10^7$ J/m^3 (corresponding to theoretically $\alpha \sim 10^{-9}$ J/m used in previous sections), the critical size would be shifted to much larger sizes (smallest $D_c \sim 340$ nm for a 16 nm high island), indicating that existence of a shape instability would be even more difficult to occur.

Hence, the lateral diameter of our (001)CGO nanodots is in general much smaller than the critical size required for shape instability to occur, pointing out why these (001)-islands always adopt an isomorphic shape since this is the equilibrium shape for typical sizes D<50 nm. Just very singular growth conditions allowed us to push the system further and drive the islands to grow beyond D_c, indicating the existence of a parameter region of unstable ripening for (001)CGO nanoislands. Elastic interactions between nanoislands should also be taken into account to definitely prove the stability of the array of uniform square-based (001)CGO nanodots. Kinetics of the system should as well be investigated.

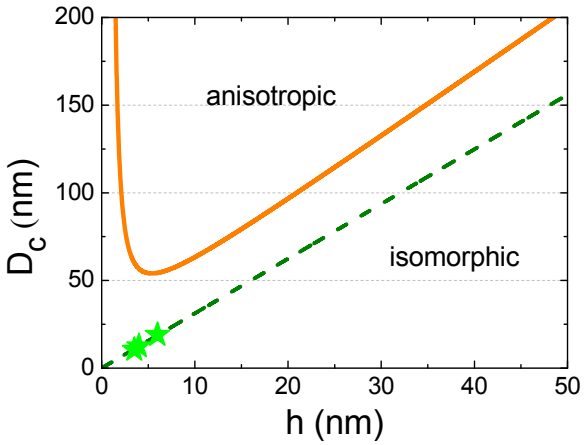

Fig. 6-11: Critical size D_c as function of height h for (001)CGO nanodots on LAO substrates; the orange continuous line indicates the dimensions above which island would experience a shape instability considering $\eta \sim 9.3 \cdot 10^7$ J/m^3 and K=0.5. The green line is the general D-h relation determined for our (001)CGO nanodots after the fitting of island's dimensions observed in TEM images (green stars).

6.3 Interfacial (011)CGO nanostructures

Let's study now (011)CGO nanoislands on LAO single-crystal substrates. As showed in chapter 5, these interfacial nanostructures are highly in-plane anisotropic and limited by (111)-lateral facets along long axes *b* and (001)-planes at short axes *a*. They arrange in two families orthogonally distributed within substrate's plane because of the two-fold symmetry of (011)CGO orientation, which results into two equivalent in-plane elongation directions, i.e. CGO[0-11]||LAO[010] and CGO[0-11]||LAO[100]. Due to their equivalence, just the former situation is analysed.

6.3.1 Equilibrium shape of (011)CGO nanostructures

Contrary to (001)-nanodots, (011)CGO nanoislands show extremely high lateral aspect ratios for all observed sizes. So, their equilibrium shape is initially investigated.

6.3.1.1 Surface energy as function of lateral anisotropy *c* for (011)-nanoislands

Accordingly to described shape of (011)CGO nanowires, long lateral facets *b* are characterized by surface energy $\gamma_b=\gamma_{111}$ and short ones *a* by $\gamma_a=\gamma_{001}$. These facets are bevelled $\theta=35^o$ and $\delta=45^o$ with respect to the substrate, respectively. These considerations yield to γ_1=-1.08 J/m^2 and γ_2=-3.82 J/m^2. Thus, the change in surface energy as function of lateral anisotropy for a (011)CGO nanoisland of fixed size is typically the one displayed in Fig. 6-12. In this example, an island of D=50 nm and h=6 nm was considered; different contributions to surface energy (distinct terms of Eq. 6-6) are also plotted.

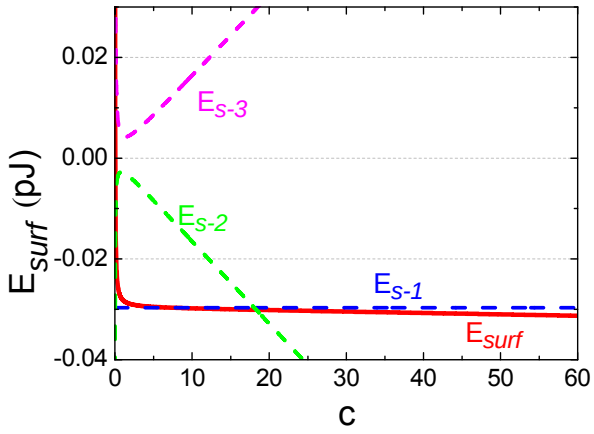

Fig. 6-12: Surface energy (—) as function of lateral aspect ratio c for a (011)CGO nanoisland of D=50 nm and h=6 nm on a LAO substrate. Different contributions to surface energy (Eq. 6-6) are also plotted: E_{S-1} (—), E_{S-2} (—) and E_{S-3} (—).

Like (001)CGO nanoislands, in the present case the change in surface energy E_{surf} is also negative; indicating that island's formation is favoured against 2D film growth from a surface energy point of view. The negative sign of E_{surf} mainly falls on the dominant contribution of term E_{S-1} (Eq. 6-6), which depends on the surface energy of planes (001)-LAO and (011)-CGO and on the relation between the equivalent thickness and the height of the islands. Therefore, as it was the case of (001)CGO nanodots, the deposition of very small amounts of material (h/t>1) and the particular relation between surface energies of substrate's surface and top plane of deposited material can overcome the commonly assumed idea that the creation of an island implies an energy cost due to the increase of the total area of the system.

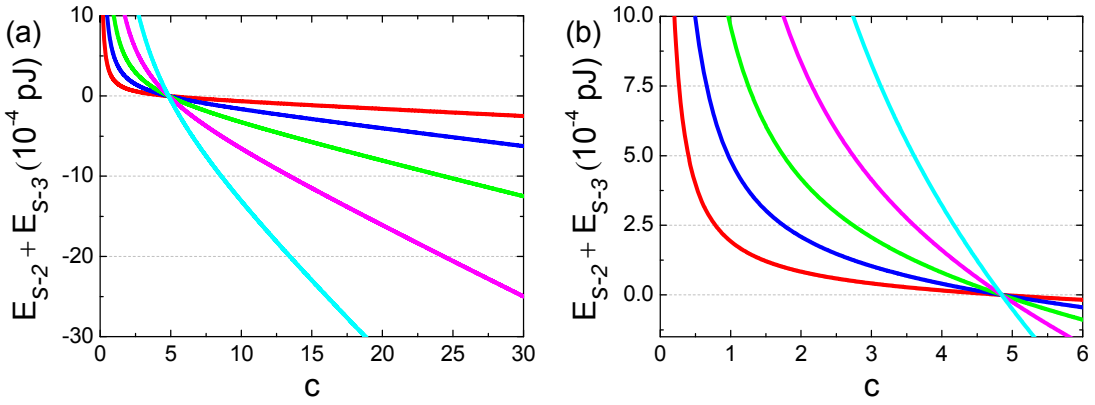

Fig. 6-13: E_{S-2}+E_{S-3} dependence with anisotropic parameter c of (011)CGO nanoislands on LAO substrates (a); different curves correspond to islands of size D=10 (—), 25 (—), 50 (—), 100 (—) and 200 (—) nm and height h=6 nm. A zoomed view of the same figure focusing on typically observed lateral anisotropies c<7 is also displayed (b).

Nevertheless, for (011)-nanoislands E_{surf}(c) dependence is even more singular. In addition to be negative, surface energy is continuously reduced if island elongates given a fixed island's volume. Such behaviour can be easily observed when omitting the dominant

contribution E_{S-1}, which is not function of lateral aspect ratio c. This is presented in Fig. 6-13, where the dependence of $E_{S-2}+E_{S-3}$ as function of c is shown for different island's volumes. Accordingly to our experimental results, the range c of relevance is $c=(b/a)^{½} < 7$, which corresponds to the maximum in-plane aspect ratio observed. Let's notice that the compute of $E_{S-2}+E_{S-3}$ is generally positive, but the negative sign of surface energy is reverted when considering again the dominant contribution of E_{S-1}.

Surface energy of (001)-CGO lateral facets is ~2.1 times larger than that of the other pair of side facets, i.e. (111) (Table 6-1). Therefore, fixed an island's volume, E_{surf} is continuously reduced if island elongates in the direction which increase (111) lateral facets, and maintains (001) surfaces at minimum. In Fig. 6-13, it is clearly appreciated that island reduces its E_{surf} when elongation satisfies c>1, which according to the assumed island's shape (Fig. 6-1) corresponds to b>a. This behaviour is in agreement with the experimentally observed shape anisotropy. For c<1 (i.e. a>b), surface energy would increase as island elongates because the expanding lateral facets would be the ones of higher surface energy, i.e. (001). Hence, in the case of (011)CGO nanostructures, E_{surf} drives the island to adopt a rectangular shape. This behaviour is in contrast to isomorphic shape promoted by E_{surf} in (001)CGO nanoislands. The anisotropy of surface energies is considered a key factor to determine the lateral aspect ratio of islands right after nucleation in heteroepitaxial systems [68]. Nonetheless, the biaxial anisotropic strain of (011)CGO nanoislands on LAO substrates relaxes this condition as we will see later on.

It is sometimes assumed that the equilibrium shape of nanoislands is determined by the ratio of surface free energies [19, 269-271]. Whereas this explanation could apply to some extent to (001)CGO isomorphic nanodots (all lateral facets are identical and $c_{eq}=1$), it does not stand for (011)-wires. Despite the relation $(\gamma_{100}/\gamma_{111})^{½}$~1.45, nanowires with lateral aspect ratios as large as $c= (b/a)^{½}$ ~6.6 are observed (chapter 5). In (011)-wires, no optimum aspect ratio is preset from surface energy considerations and elastic relaxation energy contribution must be taken into account. Therefore, these results confirm that the optimum shape of a 3D island cannot be merely determined considering surface energy contributions; and this opens questions to some island's shape analyses as those reported for metal nanocrystals on (001)STO surfaces in [21, 271, 272], where the elastic relaxation energy was not considered.

6.3.1.2 Elastic relaxation energy as function of lateral anisotropy *c* for (011)-islands

For (011)-nanoislands, lattice mismatch between CGO and LAO is known to be different depending on the in-plane growing direction (chapter 5). Lattice site model based on

the symmetry of cations sublattices predicts a compressive lattice mismatch ε~-1% along in-plane growth direction CGO[0-11]||LAO[010]. To describe the epitaxial growth along CGO[100]||LAO[100], domain matching epitaxy model was suggested as a good approximation (section 5.1.2). A 2/3 matching relation (i.e. two fluorite cells fitting 3 perovskite cells) plus a residual strain misfit ε~+5% and one misfit dislocation separating each domain seems to agree with TEM analysis. Therefore, nanowires are highly anisotropic strained when comparing in-plane growth along these two directions.

In accordance with Eq. 6-10, the stress anisotropy in our biaxial stressed model can be implemented through the strain anisotropy parameter β. It is an indicator of the ratio between the strength of the strains along CGO[100]||LAO[100] and along CGO[0-11]||LAO[010]directions. Fig. 6-14a shows the general dependence of elastic relaxation energy with lateral aspect ratio c for different values of the anisotropic strain parameter β for a fixed (011)-island volume (D=50 nm, h= 6 nm). All curves $E_{relax}(c)$ show an energy minimum at a given c_{eq}^{REL} which depends on β. In a broad extension close to c_{eq}^{REL} the elastic relaxation energy is negative. For β<1 (red curve), $c_{eq}^{REL}<1$ and elongation is favoured for a>b. According to assumed island's shape, β<1 indicates that misfit along *b* axis is higher than along *a* axis, which we know that is not the case of studied (011)- nanowires. β=1 (blue curve) corresponds to a biaxial isomorphic stressed media, and effectively, $c_{eq}^{REL}=1$. For β>1 (green curve), $c_{eq}^{REL}>1$ and elongation is enhanced satisfying b>a, which agrees with our experimental results. Nevertheless, the contribution of surface energy must also be considered to determine the lateral aspect ratio of the island and, particularly, if it will continuously elongate or there exists an equilibrium shape. In regime β>1, the elastic relaxation favours higher in-plane aspect ratio as larger is the island's volume as observed in Fig. 6-14b.

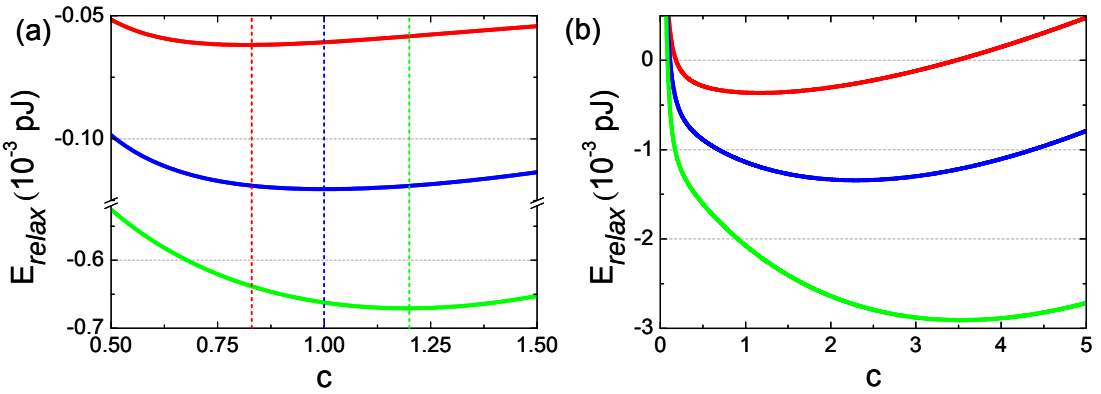

Fig. 6-14: $E_{relax}(c)$ for different anisotropic strain parameters β=0.01 (—), 1 (—) and 10 (—) for a (011)CGO nanoisland of D=50 nm and h=6 nm on a LAO substrate (a); $E_{relax}(c)$ for different (011)CGO nanoislands sizes D=50 (—), 100 (—) and 150 (—) nm and height h= 6 nm considering β=5. Parameters $\alpha=10^{-9}$ J/m and A=15 nm were used in both cases.

As mentioned above, it is commonly reported that strained islands exhibit a spontaneous shape instability induced by elastic relaxation energy [28, 68]. Reported systems and situations analyzed generally correspond to biaxial isotropic stressed islands, and the critical size at which elongation occurs is triggered by the anisotropy of surface energies. In the present case, the situation is different since we are dealing with biaxial anisotropic stress in addition to surface anisotropy. The result is that E_{relax} favours elongation for all islands' sizes. Implications of this stress anisotropy are clearly observed when comparing the behaviour of E_{relax} of (001) and (011)CGO nanoislands. For small island sizes, stress anisotropy shifts the square equilibrium island shape (Fig. 6-4, D<60 nm) to c>1 or c<1 depending on the misfit anisotropy (Fig. 6-14a). For large islands, strain energy makes the island elongate in either of the two biaxial directions isotropically stressed (Fig. 6-4, D>70 nm). This symmetry is again broken for the case of biaxial anisotropic strain, in favour of lowest misfit direction.

So, we have shown that elastic relaxation energy favours rectangular island shape in biaxially anisotropic strained (011)CGO nanoislands since nucleation, in agreement with the results reported in Fig. 5-17. Elongation in lowest mismatch direction enhances elastic energy relief. Furthermore, E_{relax} of (011)-nanoislands, in contrast to $E_{surf}(c)$, leads to an optimal lateral aspect ratio for each island's volume. Parameters α and β are explored in more detail in next section in relation to the final shape of the island.

6.3.1.3 Total energy as function of lateral anisotropy *c* for (011)-nanoislands

The total energy of a (011)CGO nanoisland is, then, the sum of E_{surf} and E_{relax}, as it is shown in Fig. 6-15. We observe that the trade-off between surface and elastic relaxation energy drives (011)-island to adopt an anisotropic rectangular shape. This particular graph corresponds to a (011)-nanoisland with D=50 nm and h=6 nm; parameters $\alpha=10^{-9}$ J/m, β=5 and A=15 nm were supposed. For this island's volume and parameters considered, the equilibrium shape corresponds to a rectangular island with a lateral aspect ratio $c_{eq}=2.8$, i.e. the wire elongates satisfying b>a in agreement with experimental results. Equivalent results were obtained for other island's sizes. The energy minima at c>1 comes from elastic relaxation term, but it is shifted to larger c values due to the contribution of surface energy; these contributions to the total energy of the island are also plotted in Fig. 6-15.

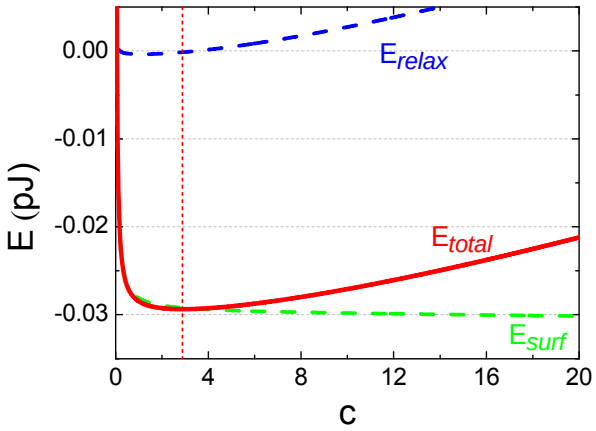

Fig. 6-15: Total energy (—) of a (011)CGO nanoisland on a LAO substrate as function of lateral aspect ratio c. This particular case corresponds to a fixed island volume of D=50 nm and h=6 nm; parameters $\alpha=10^{-9}$ J/m, $\beta=5$ and A=15 nm were assumed. Surface (--) and elastic relaxation (--) energy contributions are also plotted.

In order to explore island's behaviour as function of parameters α and β, which take into account different possible combinations of surface energy and elastic relaxation energy, we have constructed a phase diagram of island's response to distinct α and β values. A typical example is shown in Fig. 6-16, which corresponds to a (011)CGO nanoisland of D=52 nm and h=6 nm on a LAO single-crystal substrate. Equivalent diagrams were obtained for other sizes; specifically, effective diameters ranging from 30 to 124 nm were investigated.

For large α values and β<0.1 (diamond's painted region in diagram of Fig. 6-16), elastic relaxation energy has a dominant contribution to the total island's energy; and the minimum displayed by $E_{elast}(c)$ curves at c<1 becomes very relevant. Consequently, island lies in a parameter zone where its energy is minimized when it elongates satisfying a>b, and for each island volume there exists an equilibrium shape at $c_{eq}<1$. According to the island shape convention chosen (Fig. 6-1), i.e. a||[100]CGO and b||[0-11]CGO, and TEM results (chapter 5), this morphology does not correspond to the experimentally observed one.

For small α values (horizontal striped region in Fig. 6-16), (011)-nanoislands reduce their energy when b>a. For such small α values, contribution of elastic relaxation energy is negligible as compared to surface energy. Thus, in this region, for a given volume, islands would infinitely elongate dominated by E_{surf} contribution (see 6.3.1.1). However, the investigated nanowires might not belong to this region either: it was experimentally determined the existence of a relation between lateral anisotropy c and effective diameter D; as well as a link between wires' height h and its short axis a. Therefore, one may expect the existence of an equilibrium anisotropic shape c_{eq} for each island's size and not an uncorrelated behaviour leading to continuous island elongation.

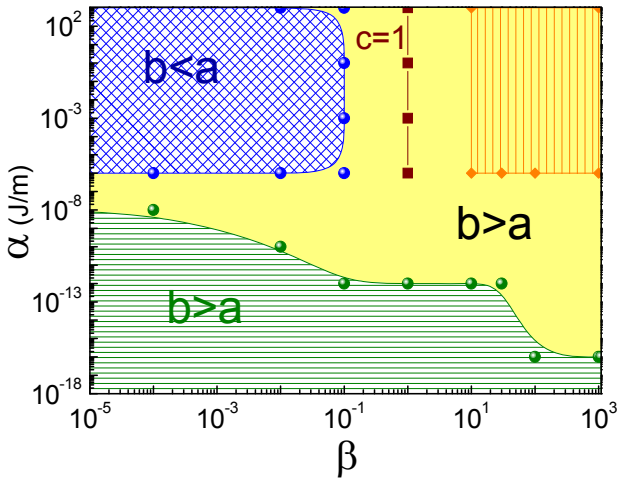

Fig. 6-16: Diagram showing the thermodynamically derived in-plane anisotropic shape of (011)CGO nanoislands on LAO substrates as function of α and anisotropic strain parameter β. Different behaviours are distinguished depending on parameter region. Island size D=52 nm and h=6 nm, and A=15 nm was used in the computation.

In yellow parameter region, nanostructures elongate satisfying b>a and there exists an equilibrium shape for each island size, c_{eq}. For β=1, the equilibrium morphology corresponds to an isomorphic (c=1) square island, as corresponds to a biaxial isotropic strain media. For large α and β values (upper right region signalled with vertical lines), the equilibrium shape is independent of elastic strains and of island's volume. However, in this region, smallest α is 10^{-6} J/m, which would result into a lattice mismatch |ε|>50% along the lowest misfit direction CGO[0-11]||LAO[010], accordingly to the estimation σ~Yε. Thus, it is not surmised that our (011)-nanowires lie in this zone since lattice site model leads to a mismatch |ε|~1% along this direction.

In the intermediate α-β region, there exists an equilibrium shape c_{eq}>1 which is function of anisotropy β. We believe that this is the region where our (011)CGO nanowires might belong. Avoiding extremely large and small anisotropic parameter β values, this region is characterized by α~10^{-12}-10^{-6} J/m, range which includes the values computed and adjusted for the case of (001)-nanoislands. Anisotropic parameter β<1 corresponds to the case where force monopoles acting perpendicular to lateral facets (111) are smaller than those normal to side facets (100). Since force monopoles and stress tensor are related through $f_i=\partial_j\sigma_{ij}$, this would be equivalent to say that misfit is minor along in-plane growth direction CGO[100]||LAO[100] than in CGO[0-11]||LAO[010]. Specifically, β=0 indicates the situation where wires grow completely incoherently along this first direction, i.e. f_i=0. Hence, for the case of (011)CGO nanowires we must focus on β>1; particularly, values 1<β<20 can be considered reasonable.

Fig. 6-17 presents the dependence of total energy of the system with island's lateral aspect ratio for different nanowires' size in the region $\alpha \sim 10^{-12}$- 10^{-6} J/m and $\beta>1$. Specifically, $\alpha=10^{-9}$ J/m was considered after stress tensor estimation. Domain matching epitaxy model arose as a good approach to describe our CGO[100]||LAO[100] interface with a residual strain $\varepsilon \sim +5\%$; therefore, we will focus our theoretical analyses on the situation $\beta=5$. Let's remark that β parameter does not directly correspond to the strain and it is merely a parameter to tune the biaxial anisotropic stress between the two in-plane growth directions. In these plots (Fig. 6-17), it is observed that the equilibrium lateral aspect ratio c_{eq} increases as island's size increases (left to right). So, as larger is the island's size, larger would be the equilibrium island's anisotropy resulting from the trade-off between surface and elastic relaxation energy. The energy minimum originates from elastic relaxation energy; and the increase of equilibrium lateral aspect ratio occurs because E_{relax} becomes more relevant to the total island's energy as island's size increases. Moreover, let's point out that strain favours an optimal aspect ratio different from that merely derived from surface energy ratio, i.e. $(\gamma_{001}/\gamma_{111})^{½}= 1.45$. However, we need to analyse the energy per unit volume to know if formation of larger islands is enhanced or not; these analyses will be carried out in following section 6.3.3.

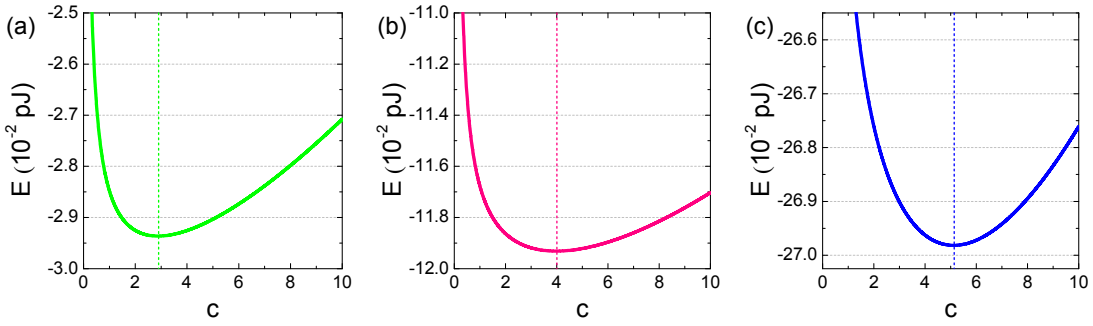

Fig. 6-17: E(c) dependence for (011)CGO nanoislands on LAO substrates of sizes D=50 (a), 100 (b) and 150 (c) nm and h=6 nm. Parameters $\alpha=10^{-9}$ J/m, $\beta=5$ and A=15 nm were used. Dotted line indicates the c value at which the energy is minima for each size, i.e. the equilibrium shape.

In this parameter region (and assuming that interface energy is negligible compared to other characteristic energies), equilibrium shapes c_{eq} determined through thermodynamic analyses can fit pretty well the experimental nanowires' sizes measured from TEM images. We know that the model used does not consider growth in h; thus, for each island size we took the height value determined from the relation h(a/2) established in Fig. 5-15. The agreement between both data is clearly observed in Fig. 6-18, where the equilibrium shape is represented as function of the effective diameter for both experimentally (open symbols) and thermodynamically (close symbols) derived data. Calculated c_{eq} data corresponds to the energy minima of E(c) curves of each island size. Pretty good fitting between measured and calculated data is achieved for $\alpha=10^{-9}$ J/m and $\beta=5$, and adjusting A within the range 3-9 nm.

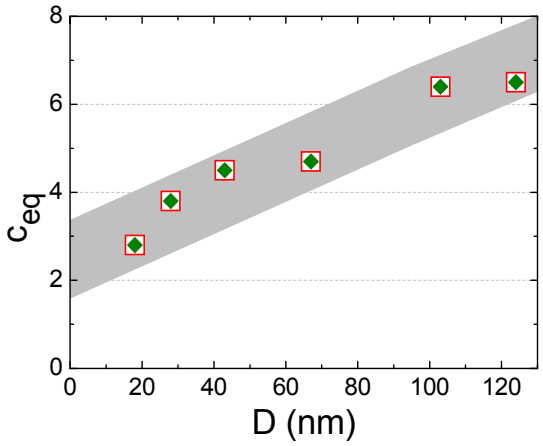

Fig. 6-18: Equilibrium anisotropic shape c_{eq} of different effective diameters D of (011)CGO nanoislands on LAO substrates. Open symbols (□) correspond to experimentally observed dimensions, and close ones (♦) refer to thermodynamically derived data. Good agreement is achieved using parameters $\alpha = 10^{-9}$ J/m and $\beta=5$, and adjusting fitting parameter A within the range 3-8 nm. Grey band indicates the general $c_{eq}(D)$ tendency.

Requirement of adjusting A to each specific nanowires' volume can be explained through the relation of parameter A with islands' height h. In last section 6.2.2 it was already established the correspondence A=Kh after comparison of our equation of elastic relaxation energy (Eq. 6-8) with the one derived by Tersoff and Tromp [28]. In Fig. 6-19 we represent the A values required in Fig. 6-18 to fit the experimental dimensions of (011)-nanowires, i.e. values used to obtain the experimental c value as the energy minima of E(c) curves given an experimental set of D and h dimensions. A linear dependence is clearly observed between the fitting parameter A and nanowires' height, A=Kh. So, the need to modify A for each islands' volume is justified. Let's notice that for a more accurate simulation the dependence of parameter α with h should also considered. Moreover, recalculations of the fitting parameter A should be as well carried out once known the interface energy of (011)CGO||(001)LAO.

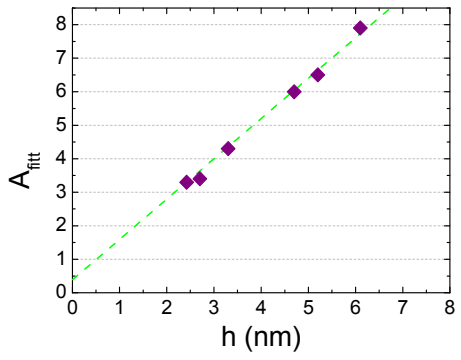

Fig. 6-19: Dependence of fitting parameter A with islands' height. A values are the ones required in Fig. 6-18 to fit thermodynamic calculations to experimental data, considering $\alpha=10^{-9}$ J/m and $\beta=5$. Height was determined from h-a relation displayed in Fig. 5-15.

Moreover, it is interesting to notice in Fig. 6-18 that the extrapolation of the $c_{eq}(D)$ values to D=0 do not cross c=1. Hence, it indicates that (011)CGO nanoislands already nucleate

anisotropic and no critical size is required for elongation to happen. In heteroepitaxial systems, the spontaneous shape instability is expected to occur once islands grow beyond a critical size D_c [28, 68]. This is the case of interfacial nanostructures with isotropic surface energies. However, the anisotropy of surface energies drives the island to adopt a rectangular shape since nucleation [68]. In the present (011)CGO||(001)LAO system, anisotropic shape of the islands is further promoted by the biaxial stress anisotropy, which acts in addition to anisotropic surface energies and strain. Elongation along lowest misfit direction coincides with the direction that enlarges lateral facets of lowest surface energy. As a result, lengthen in this direction guaranties the simultaneously minimization of both surface and elastic relaxation energy in (011)-islands. Thus, these anisotropic surface and strain contributions break the symmetry of elongation observed for the case of (001)CGO dots; and only elongation along CGO[0-11]||LAO[010] occurs for (011)CGO nanowires. Let's recall that if two orthogonal families of wires are observed in nanostructured templates is due to the two-fold symmetry of (011) orientation.

Hence, thermodynamic analyses have pointed out that the basal rectangular morphology of (011)CGO nanoislands corresponds to their equilibrium shape. Particularly, these studies indicate that these islands are anisotropic since nucleation and they satisfy the condition b>a. This rectangular shape ensures both, minimization of side facets of higher energy (i.e. (001)) and elongation in the direction of smaller misfit strain. Moreover, it has been proved that the optimum in-plane shape anisotropy increases when the island coarsens. So, within the scope of the proposed model larger nanoislands are longer. In conclusion, our work has shown that a new road is possible to the formation of nanowires oriented along crystallographic directions, based on designing anisotropically strained epitaxial nanoislands.

6.3.2 Transition from triangular to truncated (011)CGO nanostructures

TEM images (Fig. 5-15) evidenced that small size CGO nanowires have a pyramidal cross-section: lateral facets sharply meet at island's top. However, for large sizes, island truncates and new (011)-surfaces appear at the top. As it has been done for (001)-nanodots, the dependence of elastic relaxation energy with island's height can be introduced following Tersoff and Tromp calculations [28] as $\alpha \sim h^2$ and $A \sim Kh$. The surface energy of a (011)CGO nanoisland with triangular cross-section is

$$E_{surf} = \left[\varphi_1 + \varphi_2 \frac{h}{t}\right] ab + \varphi_1 \left[b\,cotg\theta + a\,cotg\delta\right] h + 2h\left[\gamma_b\, b\,cosec\theta + \gamma_a\, a\,cosec\delta\right] \quad \textbf{Eq. 6-21}$$

where $\varphi_1 = \gamma_i - \gamma_s$ and $\varphi_1 = \gamma_s - \gamma_t - \gamma_i$.

Fig. 6-20a shows a generic curve of the energy dependence as function of height h for both height terminations of (011)CGO nanoislands. The example displayed corresponds to an island of effective diameter D=18 nm and lateral anisotropy c=2.8, dimensions obtained from TEM planar-view images. At small heights, the total energy of the island is minor if it exhibits a triangular cross-section instead of a truncated pyramid cross-section. However, if the island continues to grow in z direction, truncation of island's crests is energetically favourable. This transition is indicated by a vertical dotted line in the plot. To better observe this transition Fig. 6-20b displays the difference between the energy of the non-truncated and truncated (011)-island. Once the nanoisland reaches a critical height (h_{crit}~4 nm in this particular example), the apparition of a flat surface at island's top becomes energetically favourable. Hence, the experimentally observed shape transition experienced by (011)-nanoisland's vertical termination is consequence of minimizing the island's total energy.

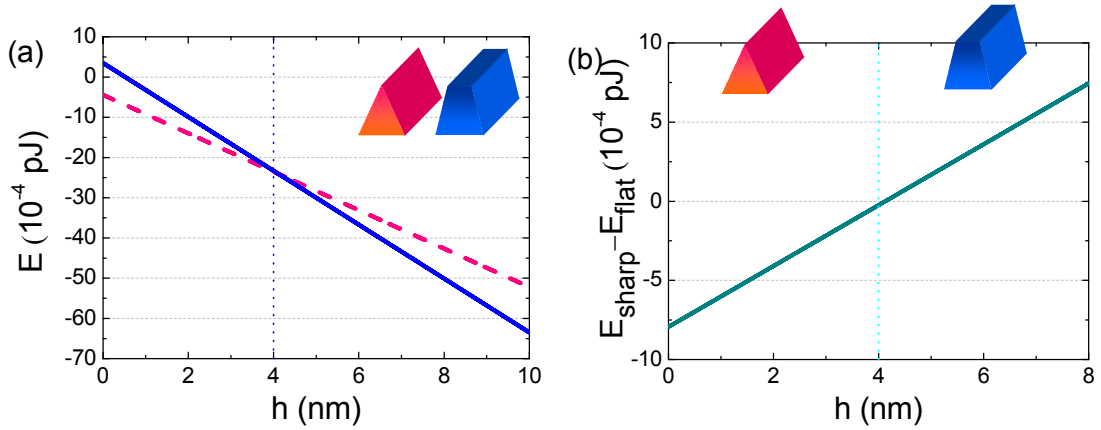

Fig. 6-20: Energy as function of height for a (011)CGO nanoisland with triangular (--) or truncated pyramid (—) cross-section (a); for a better visualization, difference (—) between these two energies is also plotted (b). The vertical dotted lines indicate the transition height from a non-truncated to a truncated shape. These examples correspond to an island of D=18 nm and c=2.8; parameters $\alpha=10^{-9}$ J/m, $\beta=5$ and K=1.5 were used.

6.3.3 Coarsening of (011)CGO nanostructures

It is just demonstrated through thermodynamic arguments that (011)-wires elongate in accordance with b>a to satisfy minimum energy requirements given a fixed islands' volume. It must be now investigated if islands remain with the given volume or coarsening mechanisms are active minimizing the energy of the system even more. With this purpose and as done with (001)-dots, the changes in the energy per unit volume as island size D increases are investigated for a given anisotropy c. Nanowires' volume is estimated through the rough approximation $V \sim hD^2$.

6.3.3.1 Surface energy density as function of effective diameter *D* for (011)-nanoislands

Recalling Eq. 6-6, the change in surface energy per unit volume due to the formation of a 3D island instead of a 2D thin film can be written as

$$\frac{E_{surf}}{V}=\gamma_1\left[\frac{1}{t}-\frac{1}{h}\right]+\frac{\gamma_2}{D}\left[c\,cotg\theta+\frac{1}{c}cotg\delta\right]+\frac{2}{D}\left[\gamma_b c\,cosec\theta+\gamma_a\frac{1}{c}cosec\delta\right] \qquad \textbf{Eq. 6-22}$$

Dependence of surface energy density with effective diameter D is shown in Fig. 6-21 for different fixed anisotropies c. In all cases, constant island height h=8 nm was considered. Given a fixed lateral aspect ratio c, $E_{surf}/V(D)$ is negative, though two differentiate behaviours can be distinguished depending on the degree of anisotropy. For aspect ratios larger than c>7, E_{surf}/V increases with D; it corresponds to dashed curves in Fig. 6-21. However, since in general lateral aspect ratios no larger than $c=(b/a)^{½}=6.5$ are experimentally observed for (011)-wires, we can restrict to the situation c<7. In these cases, E_{surf}/V endlessly decreases as effective diameter D increases. Particularly, E_{surf}/V is lower as larger is the corresponding lateral aspect ratio. It agrees with previous E_{surf} analyses where it was proved that, given a constant island's volume, the surface energy decreases as island elongates. The highest surface energy corresponds to the case c=0.5<1, which is known to not apply to our experimental results. So, surface energy density favours infinite coarsening of (011)-nanowires and, thus, continuous increase of their volume in order to minimize the energy of the system.

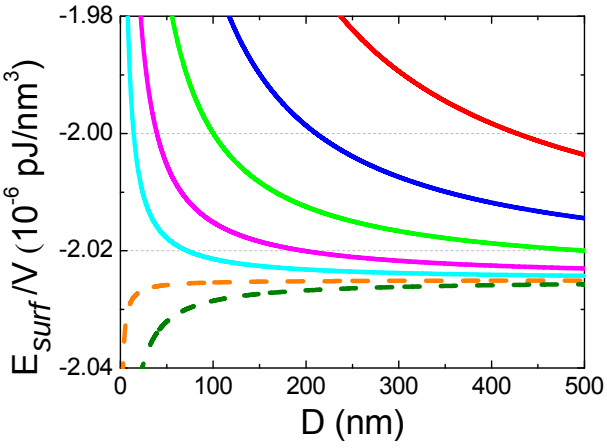

Fig. 6-21: Surface energy density as function of effective diameter D of (011)CGO islands on LAO substrates. Curves correspond to fixed lateral aspect ratios c=0.5 (—), 1 (—), 2 (—), 4 (—), 6 (—), 8 (--) and 10 (--). In all cases, a constant height h=8 nm was assumed.

6.3.3.2 Elastic relaxation energy density as function of effective diameter *D* for (011)-nanoislands

The energy per unit volume due to elastic relaxation energy and short-range contribution of edges of (011)-nanoislands is

$$\frac{E_{relax}}{V} = -\frac{\alpha}{hD}\left\{\frac{1}{c}ln\left(\frac{cD}{A}\right)+\beta c\, ln\left(\frac{D}{cA}\right)\right\} \qquad \textbf{Eq. 6-23}$$

When localizing in the adequate α-β parameter region determined in the diagram exhibited in Fig. 6-16 ($\alpha \sim 10^{-8}$-10^{-12}J/m, $1<\beta<20$), E_{elast}/V shows an energy minimum as function of effective diameter D given a fixed shape anisotropy c. This behaviour $E_{elast}/V(D)$ is shown in Fig. 6-22; different curves correspond to distinct lateral aspect ratio values. For each lateral aspect ratio c, the elastic relaxation energy density is minima at specific size D_{opt}^{REL}. Particularly, it is found that higher the anisotropy c, larger is the corresponding equilibrium size D_{opt}^{REL}, if b>a is satisfied. Again, the highest energy values correspond to the situation where the island would elongate satisfying a>b, which is the case never observed to happen to our nanowires. Hence, contrary to surface energy density, the contribution E_{relax}/V acts against coarsening once the optimal diameter D_{opt}^{REL} is reached, i.e. E_{relax}/V favours an equilibrium rectangular island's size.

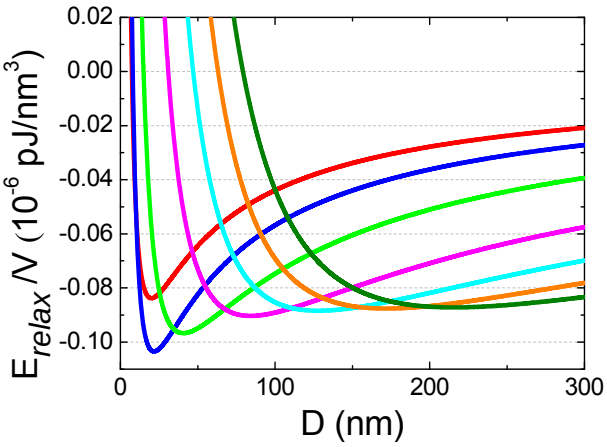

Fig. 6-22: Elastic relaxation density as function of effective diameter D for (011)CGO islands on LAO substrates. Curves correspond to fixed lateral aspect ratios c=0.5 (—), 1 (—), 2 (—), 4 (—), 6 (—), 8 (—) and 10 (—). In all cases, a constant height h=8 nm was assumed. Parameters $\alpha=3\cdot10^{-9}$ J/m, β=5 and A=8 nm were used for the calculation.

6.3.3.3 Total energy density as function of effective diameter D for (011)-nanoislands

Consistently with presented energy contributions (E_{surf}, E_{relax}), the total energy of (011)CGO nanoislands on LAO substrate is minimized at a characteristic island effective diameter D_{opt} (Fig. 6-23). Equilibrium size D_{opt} is found to be different for each aspect ratio c. The existence of a minimum is due to the elastic energy density contribution, but the corresponding energy is lower to that reported in Fig. 6-22 because of the negative contribution of surface energy density. Thus, there is an optimum island size D_{opt} for each anisotropy c. In Fig. 6-23, the dependence E/V(D) is plotted for different c values.

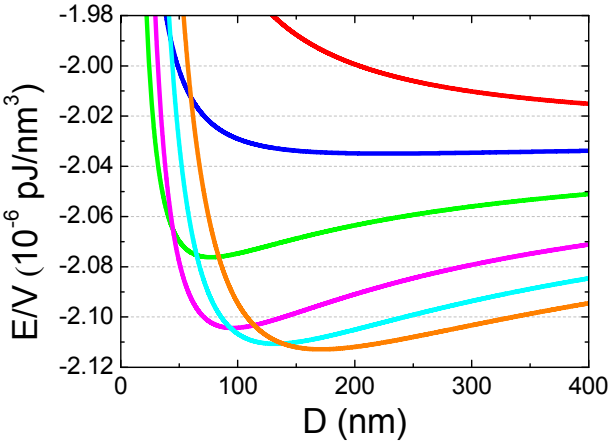

Fig. 6-23: Total energy density as function of effective diameter D of (011)CGO nanoislands on LAO substrates. Curves correspond to fixed lateral aspect ratios c=0.5 (—) 1 (—), 2 (—), 4 (—), 6 (—), 8 (—). In all cases, constant height h=8 nm and parameters $\alpha=3\cdot10^{-10}$ J/m, β=5 and A=8 nm were used.

Upon these results, one could imagine that, consequently, coarsening between (011)-wires is not favoured once the optimum size D_{opt} is reached. However, as reported in last section for studies based on fixed islands' volumes, we know that as larger is the nanowire, higher is the equilibrium lateral aspect ratio c. Hence, for a specific anisotropy c, once the wire reaches its optimum size D_{opt}, it will not grow more in volume but it will start to elongate. Thus, a new lateral aspect ratio c_2 will be set and, as a result, the island energy will be described by a new $E_{c2}(D)$ curve in Fig. 6-23. Since D_{opt} increases as anisotropy does, the wire will then be able to increase its volume at the same time that minimizes its energy to reach the new equilibrium size D_{opt-2}. This process will be non-endlessly repeated. As a result, the energy of the system is continuously lowered by reaching a subsequent D_{opt} as the anisotropy c increases. The continuous decrease of the energy per unit volume as function of the equilibrium size is shown in Fig. 6-24a for fixed island's height h=8 nm; the plot besides (Fig. 6-24b) gives the

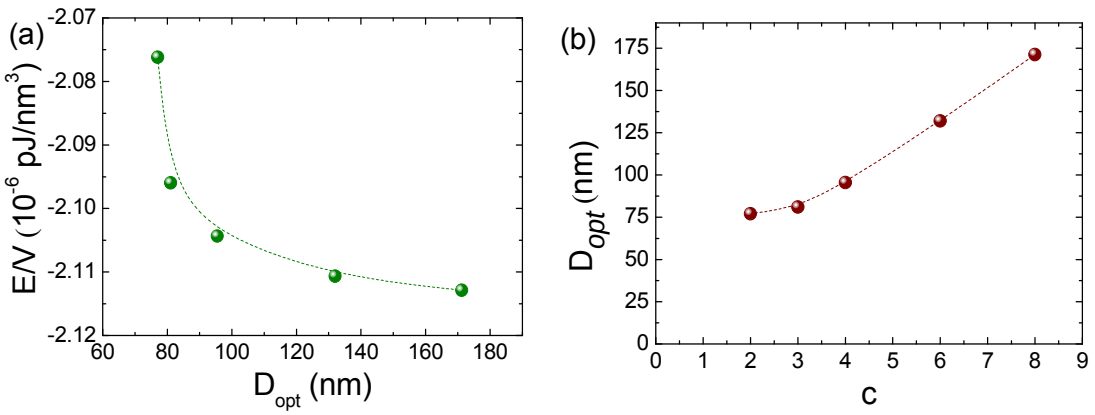

Fig. 6-24: Total energy per unit volume corresponding to each equilibrium size D_{opt} of (011)CGO wires on LAO (a). Relation between D_{opt} and anisotropy is also displayed (b). Island's height h=8 nm and parameters $\alpha=3\cdot10^{-9}$ J/m, β=5 and A=8 were used in the calculations.

D_{opt} corresponding to each lateral aspect ratio c investigated. That is, for a fixed lateral aspect ratio c we determine the D_{opt} in Fig. 6-23 (correlation plotted in Fig. 6-24b); the E/V corresponding to this D_{opt} in Fig. 6-23 is the one plotted in Fig. 6-24a. Therefore, we have demonstrated that coarsening phenomena are effective in kinetically-limited (011)CGO nanoislands on LAO substrates, which tend to infinitely grow in volume at the same time that they continuously elongate.

6.4 Thermodynamic comparison between (001) and (011) CGO nanoislands on LAO

The main key points driving (001) and (011) CGO nanostructures to such distinct shapes and sizes have been settled through detailed thermodynamic analyses of the energies involved in the formation and coarsening of interfacial CGO nanoislands on LAO substrates.

For a given island volume, the path towards energy minimization drives (011)CGO nanoislands to continuously increase their lateral aspect ratio as their effective diameter increases. In contrast, lowest energy requirement makes (001)-nanostructures remain isomorphic for typical observed sizes, i.e. D<50 nm. These differences lie in the symmetries and asymmetries of lateral facets and strain misfits which characterize (001) and (011) CGO nanostructures, respectively, which result into distinct dependences of surface and elastic relaxation energies. The growth of islands under biaxial isotropic stress ((001)CGO islands) yields to the existence of a spontaneous shape instability in the case of isotropic surface energies once a critical size D_c is reached. Below D_c islands adopt an isomorphic square shape and, above it, it would have a rectangular base. Nearly all (001)CGO nanodots grown belong to the first situation $D<D_c$. In the case of anisotropic surface energies of strained-islands, nanostructures are anisotropic since nucleation. This behaviour is even stressed in the case of (011)CGO nanoislands because of the biaxial anisotropic stress. Elongation in the direction of lowest misfit direction coincides with the shape that enlarges lateral facets of lower surface energy. So, high lateral aspect ratios ensure the minimization of both surface and strain energies of (011)-nanoislands given a fixed island's volume. Distinct equilibrium shapes of (001) and (011) CGO nanostructures on LAO substrates are appreciated in Fig. 6-25, where $c_{eq}(D)$ dependences are presented for experimental and calculated data. Good agreement between both data is achieved for both isomorphic and anisotropic nanoislands, indicative that island's morphology corresponds to its equilibrium shape in each situation.

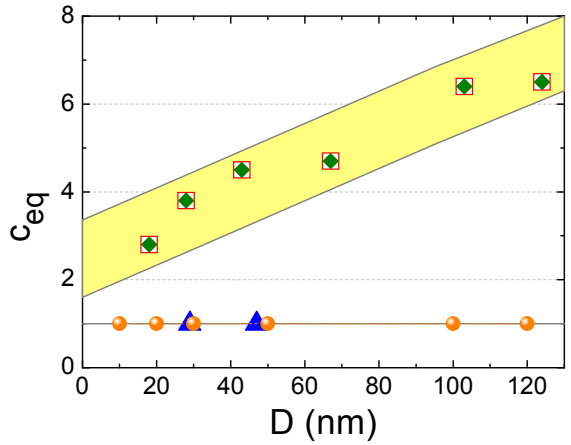

Fig. 6-25: Comparison of thermodynamically derived in-plane equilibrium shape c_{eq} as function of size D for (001)CGO dots (●) and (011)CGO wires (♦) on LAO substrates. Relation $c_{eq}(D)$ experimentally determined from TEM images is also plotted for both dots (▲) and wires (□). Parameters $\alpha=5\cdot10^{-10}$ J/m, $\beta=1$ and A=4 nm were considered for the case of (001)-nanoislands, whereas $\alpha= 10^{-9}$ J/m, $\beta=5$ and fitting parameter A within the range 3-10 nm were used for (011)-nanowires (see Fig. 6-19).

Referring to their behaviour with respect to coarsening, reduction of the total energy per unit volume is observed to occur in (011)-wires as their size increase. Thus, coarsening phenomena makes nanowires to continuously increase their volume. This explains the tendency of wires to always reconstruct into larger ones. However, isomorphic (001)-nanoislands stabilize their size at relatively small volume, and no further growth in effective diameter D takes place since it would imply an increase of the total energy per unit volume. Reaching a stable size seems to be the main cause of the lack of evolution of (001)CGO nanodots; just special conditions could drive these islands to grow beyond the critical stable size. Consideration of elastic interactions between islands is required to definitely prove the stability of (001)CGO. Comparison of E/V dependence with size D_{opt} is shown in Fig. 6-26, where opposite behaviours of E/V for (001) and (011) CGO islands are clearly distinguished. Let's

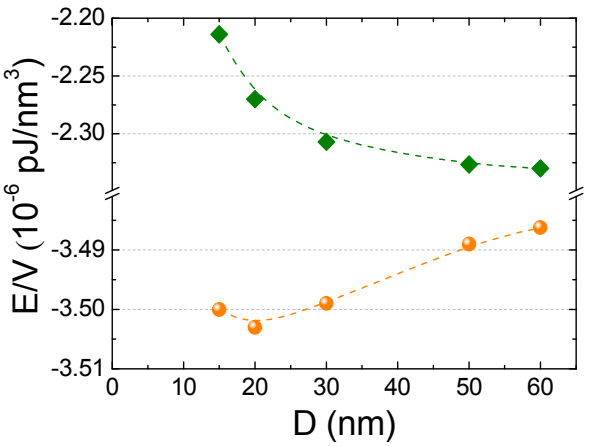

Fig. 6-26: Total energy per unit volume as function of island's size D of (001)CGO dots (●) and (011)CGO wires (♦) of constant height h=6 nm on LAO substrates. Parameters $\eta=9.35\cdot10^{7}$ J/m^3, K=0.5 and $\beta=1$ for (001)-islands and $\beta=5$ for (011) were used in the computation.

remark again that these results derive from a model assuming kinetically-limited growth in h and, thus, these E/V(D) plots corresponds to islands of constant height.

In summary, both the square shape of (001)CGO nanoislands and the rectangular shape of (011) ones correspond to the equilibrium morphology of these strained CGO nanostructures for the observed sizes. The size stability of (001)-dots or the tendency to continuously coarsen of (011)-wires can also be explained from thermodynamic arguments. Hence, despite the approximations made (interface energy neglected, kinetically-limited vertical growth, stress tensor, elastic parameters of the substrate, T=0 K, etc.), the model used has allowed us to explain the main and representative features of these two kinds of CGO nanoislands on LAO substrates.

However, it still remains as an open question why both (001) and (011) CGO nanoislands can nucleate in such similar growth conditions. Similar interface energy values could be the cause. Fig. 6-27 shows the total energy per unit volume of (001) and (011)CGO nanoislands using same α and A parameters. Small differences observed between the energy of both sort of islands suggest that their nucleation energy might be very close; however, ab initio calculations should be carried out to prove it. These energetic differences can even be reduced considering higher interface energy γ_i for the (011)CGO||(001)LAO configuration than for (001)CGO||(001)LAO. For example, dashed lines in Fig. 6-27 indicate the E/V(D) of (011)-nanoislands considering γ_i = 0.5 and 1 J/m^2.

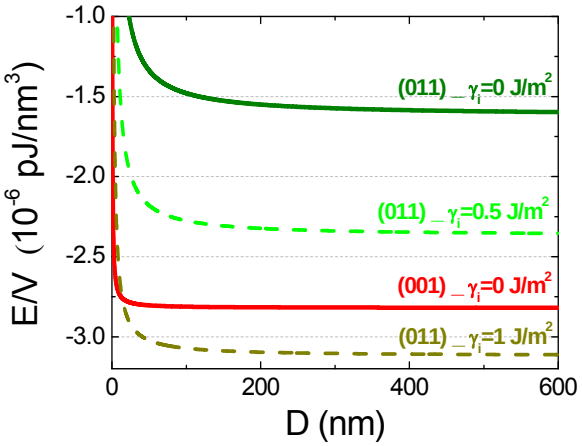

Fig. 6-27: Total energy density of (001)CGO (—) and (011)CGO (—) nanoislands on LAO; parameters η=10^7 J/m^3, K=1, γ_i=0, h=2 nm, c=1 and β=1 (for (001)) and β=5 (for (011)) were used in the computation. Dashed lines corresponds to E/V of (011)-islands for the case of γ_i=0.5 J/m^2 (---) and γ_i=1 J/m^2 (---).

6.5 Interaction between CGO nanoislands

In general, CGO nanoislands are not isolated but surrounded by many other islands. Therefore, consideration of interaction energy is required to complete the thermodynamic analysis of CGO interfacial nanoislands' formation and growth (Eq. 6-1). These advanced

theoretical studies are out of the scope of the present work. However, analyses of the experimental results can give us some hints about the phenomena going on.

The most outstanding features arise again between the distinct behaviour observed among nanodots and among nanowires, respectively. Fig. 6-28 displays two templates, one with (001)-nanodots (a) and the other with (011)-nanowires (b). The former was processed 8 hours in oxidizing atmosphere, whereas the latter was just treated 30 minutes in Ar-H_2 reducing atmosphere; both of them at 1000^{o}C. The amount of deposited material was the same in both cases (0.005 M, same deposition conditions). However, the volume of a single (011)-nanowire is typically at least more than six times larger than the average volume of a (001)-nanodot. Therefore, these different islands' sizes as well as template's landscape suggest distinct mechanisms of interaction among nanodots and among nanowires, objecting or enhancing coarsening, respectively.

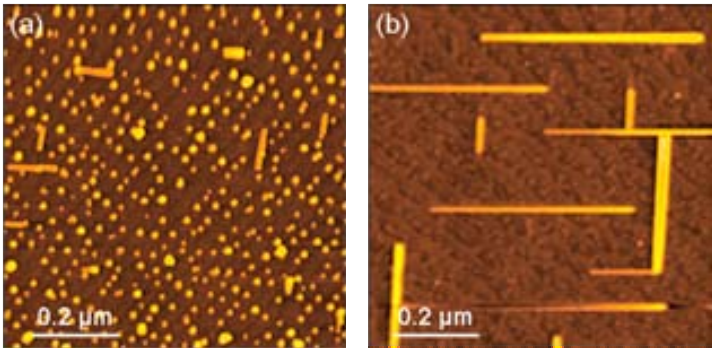

Fig. 6-28: CGO/LAO templates mainly characterized by (001)-nanodots (a) and (011)-nanowires (b), respectively. Nanodots were processed 8 hours in oxidizing atmosphere, whereas nanowires were just treated 30 minutes in reducing atmosphere; both of them at 1000^{o}C.

Thermodynamic studies of isolated (001)CGO nanoislands have already predicted the existence of a stable size for our nanodots at a given constant height (section 6.2.3). Moreover, the lack of coarsening phenomena observed in a dense array of dots in standard processing conditions (O_2) (Fig. 6-28a) suggests the existence of repulsive interaction among this kind of islands. This behaviour would explain the homogenous separation between nanodots in a single terrace. Distribution of nanodots into rows seems to be mainly consequence of the confining power that lattice steps exerts on nanodots (section 5.2.1), despite repulsive interaction might also occur as suggested by the local 2D order (Fig. 5-22).

As mentioned previously, when an island grows it exerts a force on the substrate which reduces island's elastic energy and causes the deformation of the substrate. Distortions propagate through the substrate and long-range elastic interactions constitute the mechanism of interaction between islands [15, 41, 46]. At first approximation, the interaction energy is the energy of a dipole-dipole elastic interaction (Eq. 1-10). After the consideration of all energetic terms involved in Eq. 6-1, Shchukin *et al.* [44] demonstrated the existence of a parameter region

where the formation of stable nuclei was favourable against Ostwald ripening (see also section 1.2.6.1). Particular combination of the contribution of edges to elastic relaxation energy, renormalized surface energy and repulsive interaction energy might result in a stable 2D periodic square lattice array of islands with optimum size L_{opt}. All our experiments seem to indicate that (001)CGO nanodots lay in this particular region, where self-assembling and self-organization is maintained during long annealings, i.e. 8 h. Moreover, theoretical studies [44] pointed out that the square lattice is the minimum energy configuration for a 2D array of pyramid islands. This energy minimization is due to the cubic anisotropy of the elastic module of the medium and due to the square base of the islands, both conditions satisfied by (001)CGO nanodots. This could explain the local tendency to 2D order of dots. However, let's recall that the influence of lattice steps on nanodots should be considered to fully describe the arrangement of (001)-nanodots [258]. Hence, periodic distribution of dots along a single step seems to be explained by repulsive interaction between them.

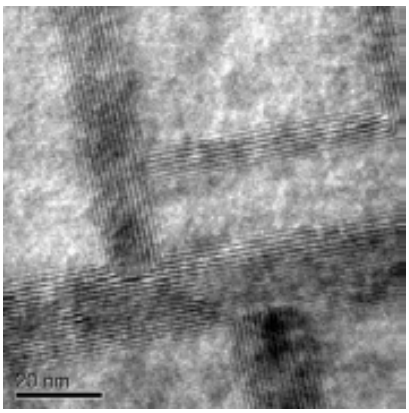

Fig. 6-29: TEM planar-view showing the formation of an intricate labyrinthine group after the junction of orthogonal nanowires.

On the other hand, we suggest attractive interaction between (011)CGO nanoislands as one clue to explain the formation of extremely long nanowires in brief periods of heat treatment, i.e. < 30 min (Fig. 6-28b). Despite the rareness and unusual phenomenology of this type of interaction, many examples presented in chapter 5 push towards this behaviour among specific islands' sides. Otherwise, the continuous formation of nanolabyrinthine structures after the junction of perpendicular (011)-wires would be difficult to explain, especially in those cases were highly dilute solutions were used (Fig. 5-29). Junction between orthogonal nanowires is repeatedly observed. Particularly, a remarkable tendency of wires to join through their ends in 90^{o} configuration is very often appreciated, suggesting that attraction is stronger at nanowires' ends. Contrary, two nanowires lying parallel are never observed to join in spite of being at distances as close as 20 nm. This fact suggests that along this direction the interaction among nanowires is very likely repulsive. Fig. 6-29 displays an example of an intricate maze-like group of (011)-nanowires.

The force that an island exerts on the substrate, and so substrate's distortion, depends on the lattice mismatch ε (and the discontinuity of the intrinsic surface stress tensor) (section 1.2.4). A compressive strained island induces substrate compression in substrate free surface adjacent to island's edges [26, 41], and extension for tensile systems. Fig. 6-30 shows the contour plots of radial strain ε_{rr} determined using finite element simulations for a cone-shaped islands [26]; in the figure it is observed that the ε_{rr} changes sign in the free substrate regions adjacent to the strained island. So, in the case of (011)-nanowires, theoretical analyses of interaction among islands become highly complex due to the anisotropy in strain and the distinct lattice mismatch sign, i.e. ε~-1% along CGO[0-11]||LAO[010] and ε~+5% along CGO[100]||LAO[100]. Basic calculations of the interaction between two facets of two distinct islands should consider the elastic constants of the system and the misfit of the two crystallographic orientations involved [15]. These computations should extend among all facets of islands implied in the interaction. To our knowledge, these specific and complex calculations have not been carried out.

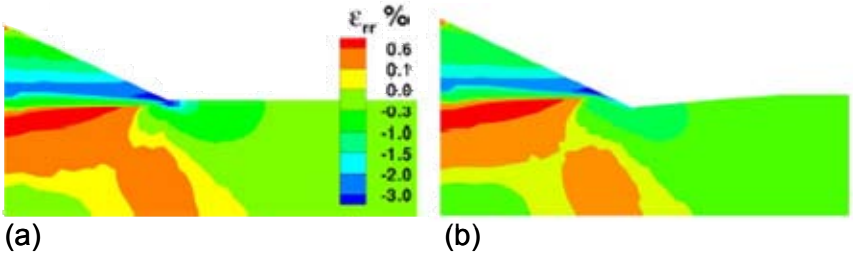

Fig. 6-30: Contour plots of distribution of radial strain ε_{rr} for a cone-shaped island without (a) and with trench (b) [26]. Notice that the ε_{rr} changes sign in the free substrate regions adjacent to the strained island.

For a simpler system with strong elastic anisotropy (i.e. mostly III-V and II-VI semiconductors) and biaxial isotropic misfit strain ε, it has been pointed out the existence of attractive interaction between islands whose directions are aligned in a narrow interval close to substrate soft axes [100] and [010] [15] (section 1.2.4, Eq. 1-11). As a result of this attractive interaction, islands might order in chains along these directions. Experimentally, preferential arrangement of InAs quantum dots in rows parallel to elastically soft <100> directions has been observed [273]. Despite the simplicity of this model with respect to our real system, the important feature is that it considers the possibility of attractive interaction among islands. The sign of this interaction is not usual, since it is normally assumed that interactions between islands are of repulsive nature. Additionally, the particular disposition of (011)-nanowires (i.e. long axis aligned with [100] or [010] LAO directions) also suggests that attractive interaction might occur along [100] and [010] substrate soft axes. Therefore, for the junction of (011)-wires, the whole nanowire should diffuse along these soft substrate axes. Since there exist two degenerate in-plane orientations of (011)CGO nanostructures, diffusion would occur along both

substrate soft axes resulting in a high probability of nanowires' impingement. So, attraction between nanowires along these directions could explain the formation of clusters of multiple orthogonal (011)-nanowires. Besides the reconstruction of these clusters into long wires aligned along <100>LAO, the union of nanowires along a single substrate direction <100> has also been observed to lead to the formation of chains of nanoislands larger than ~ 2 μm (see for example Fig. 6-34c and d), as predicted to happen for the case of attractive interactions proposed in [15]. Quick engulfment of (001)-nanodots by (011)-wires also hints attractive interaction between these types of islands.

So, from our experimental results we can suggest a simple classification of the interactions taking place among CGO nanoislands on LAO substrates. For an easiest description of the distinct configurations, we refer to the in-plane axis of the islands along the interaction direction. The growth of (001)-nanodots, CGO[110]||LAO[100], is characterized by low mismatch, i.e. ε_L; the same mismatch exists along (011)-nanowires' long axis [110]. Contrary, short axis of (011)-nanowires [100] has high lattice mismatch, i.e. ε_H. So, we can associated island's [110] axis with ε_L and [100] of (011)-nanowires with ε_H. Schematic representation of the interactions suggested is depicted in Fig. 6-31.

On one hand, experimental results point out the existence of repulsive interaction between the axes [100] and [100] of neighbour islands. This would explain the non-coalescence of parallel (011)-nanowires in the direction perpendicular to their long axis. This behaviour also applies to the interaction between (001)-nanodots. Both situations are sketched in Fig. 6-31a and b, respectively. In this case, confronted island's edges have the same misfit sign and, thus, elastic repulsion is expected.

On the other hand, attractive interaction seems to happen between islands' [100] and [110] axes. This would be the case between (011)-nanowires aligned along orthogonal directions (i.e., between [100] and [110] directions of nanowires axis) (Fig. 6-31d) and among (001) and (011)-islands along the direction perpendicular to nanowires' long axis (i.e. [100] axis of the nanowire and [110] of the isometric (001)-dot) (Fig. 6-31e). For these two configurations, edges faced show opposite lattice mismatch sign. Substrate must expand close to one island, whereas in regions adjacent to the other it must compress. As a result, attractive interaction among these island's edges seems reasonable.

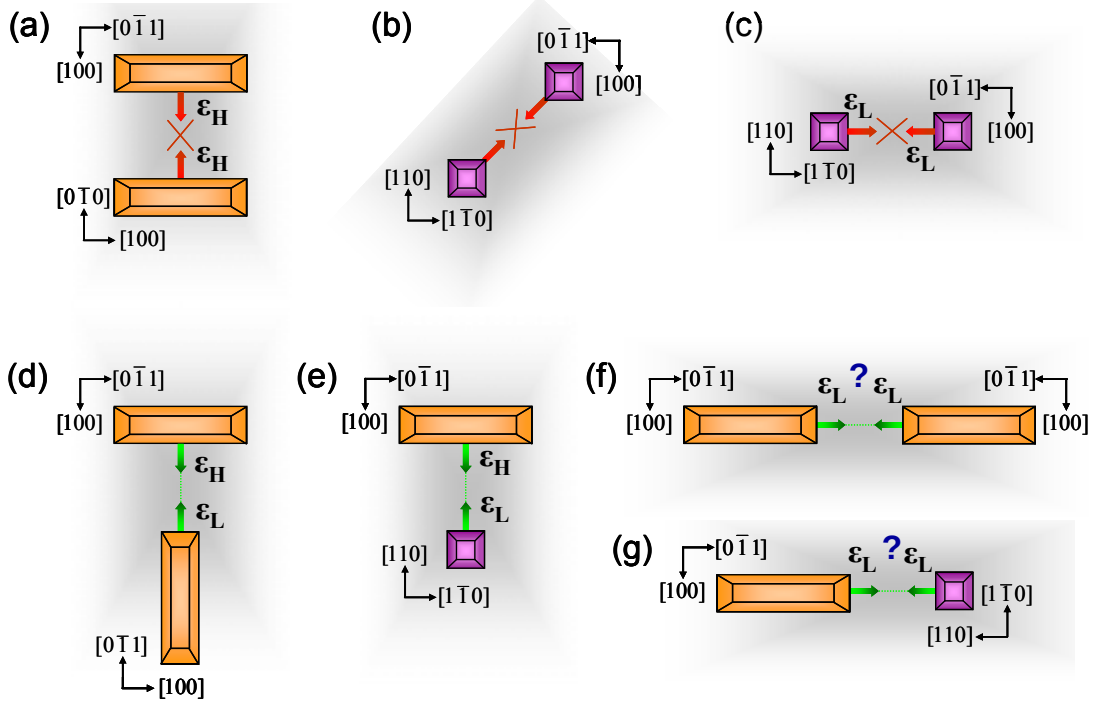

Fig. 6-31: Suggested interaction between interfacial CGO nanoislands on LAO substrates. Repulsive interaction between [100] axes: (011)-nanowires in the direction perpendicular to their long axis (a) and between (001)-nanodots (b); and repulsive interaction also between [011] axes among (001)-dots (c). Attractive interaction between [100] and [110] axes: among orthogonal (011)-nanowires (d) and among (001) and (011)-islands along the direction perpendicular to nanowires' long axis (e). Attractive interaction might also occur between [100] axes of wires aligned parallel in a single direction (f) and among (001) and (011)-islands along the direction parallel to nanowires' long axis (g). ε_L indicates the low mismatch along [110]CGO||[100]LAO, and ε_H the high mismatch along [100]CGO||[100]LAO.

Despite not so often observed, some snapshots could also suggest attraction between (011)-nanowires aligned parallel to a single direction (Fig. 6-31f). In this case, attractive interaction would take place between islands' [110] axis. This behaviour would also explain interaction among (001) and (011)-nanoislands along the direction parallel to nanowires' long axis (Fig. 6-31g). However, this attractive interaction between [110] axis seems to not apply among (001)-nanodots (Fig. 6-31c), otherwise it could be difficult to explain the formation of arrays with self-organized stable nanodots (section 5.2.1). Interaction along [110] islands' axes involves island's edges of same misfit sign, which open questions to the attractive interaction according to substrate's distortions expected [41]. However, what differentiates systems with (011)-wires from those with exclusively (001)-dots is that substrate distortion (compression/extension) changes at each wire's "edge-corner". Nanodots are embedded in a biaxial isotropic strained medium; thus, the lack of strain modulation would not favour attraction between islands. Moreover, thermodynamic analysis proved the stability of an isomorphic square (001)CGO nanoisland, and the existence of an optimum island size. On the other hand, it must be noticed that (001)-wires also grow under biaxial isotropic strain and, thus, attractive interactions between them are not expected. This would explain the formation of (001)-wires as long as 30 μm, which merely happen to get in contact with other orthogonal

wires by chance since there is no driving force. Repulsive interaction seems to exist at least between parallel (001)CGO wires, since parallel wires do not coalesce despite being aligned as close as 20 nm.

All these interactions are proposals to explain the experimental observations in a very simple manner. Complex theoretic analyses are required to prove them. Nonetheless, some additional experimental evidence supporting this assertion has been obtained from TEM analyses. The TEM planar-view exhibited in Fig. 6-32 seems to illustrate that some important modification of strain at the substrate is occurring as consequence of the presence of interfacial CGO nanoislands. The mean separation D between Moiré's fringes changes at (011)-wires' extremes, indicative of different strain in this region of the wire with respect to its central part. An arrow in the inset points to a discontinuity in the Moiré fringes. The presence of a (001)-nanodot could be the cause of a distortion in the substrate which is propagated through it and finally affects the nanowire. In any case, existence of strain modification at nanowires' ends is clearly derived from this image. Assuming that (011)CGO nanowires are completely relaxed (i.e. lattice parameter a_{CGO}=5.41 Å), the Moiré pattern at wire's end could be reproduced ($d=a_{CGO}\cdot a_{subst}/a_{CGO}-a_{subst}$; Eq. 5-3) if substrate lattice parameter was 3.93 Å instead of a_{LAO}=3.79 Å as would correspond to LAO single-crystal (and as applies to Moiré pattern in the middle of the observed wire). This ~3.5% difference between substrate lattice parameter in these two regions of the (011)-nanowire (end, middle) suggests that the strain field is different at wires' ends.

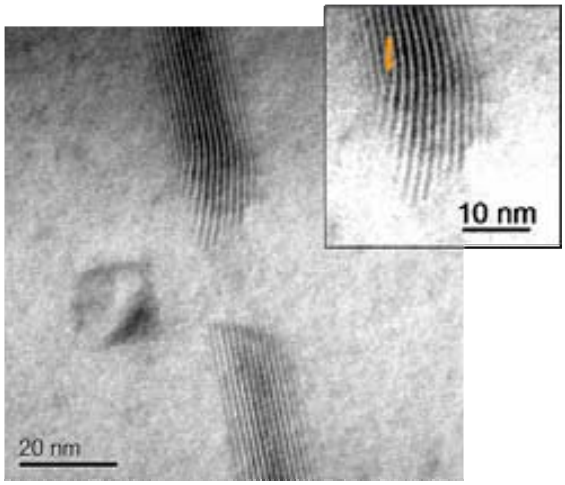

Fig. 6-32: TEM planar-view where bending of Moiré's fringes at the ends of (011)-nanowires' is observed. These modifications can be attributed to the presence of the isomorphic (001)-island, which may probably induce a long-range elastic deformation of the substrate. The mean separation between fringes also changes; the inset shows a zoomed viewed where the discontinuity of a fringe is indicated.

Summarizing, repulsive interaction has been proposed among (001)-nanodots as one of the clues of the absence of coarsening in dense arrays of this kind of CGO nanoislands and to

explain the homogeneous distribution of nanodots along a single terrace, with the concomitant tendency towards observation of 2D local order. Order of nanodots into rows seems to be mainly guided by steps of vicinal substrate (section 5.2.1) [258]. Repulsive interaction has also been proposed between (011)-nanowires' long axes, since union of wires in this configuration has never been observed. Contrary, attractive interaction between (011)-nanowires and (001)-dots and among (011)-nanowires could explain, in part, the ultrafast kinetics at high temperature and reduced oxygen pressure experienced by those systems with interfacial (011)-nanoislands. Despite conventional wisdom generally assumes repulsive interaction between interfacial nanoislands, possibility of attractive interaction has already been predicted [15], and our experimental analyses suggest that this may indeed occur.

6.6 Kinetic evolution of (011)CGO nanostructures

Thermodynamic arguments have proved to explain the equilibrium shape of both (001) and (011) CGO nanostructures on LAO substrates; that is, their respective isomorphic and anisotropic morphology has a thermodynamic origin. Their distinct coarsening phenomena have also been thermodynamically derived. Moreover, distinct interaction mechanisms have been proposed to explain the behaviour of CGO dots and wires. Nonetheless, evolution towards equilibrium must be necessarily associated to kinetic mechanisms pushing the system towards this situation.

Mobility of (001)-nanodots is limited, most likely because they rapidly achieve their stable configuration and do not evolve to other states. Just very singular treatment conditions could drive (001)-nanoislands to grow beyond its uniform isomorphic shape. The formation of extremely long (001)CGO nanowires under particular growth conditions could open the possibility to kinetically-limited nanodots evolution. Self-limited growth and formation of stable arrays of islands has been observed and interpreted in the semiconductor field [12, 56]. Long treatments of (001)-nanoislands in Ar-H_2 could be a way to surmount coarsening barriers through generation of oxygen vacancies. However, the fact that thermodynamics yields to isomorphic (001)-island as the equilibrium shape for sizes D<50 nm hints that under present conditions the shape and size of (001)-nanodots is effectively thermodynamically-controlled. The formation of wires indicates that there exist other growth conditions where unstable ripening might occur and which deserve being investigated. It has been pointed out that the stability and equilibrium shape of semiconducting pyramids and domes is broken above a critical temperature where ripening continuously occur [60]. Notice that all thermodynamic analyses presented refer to T=0 K case, and divergences arising from temperature dependence might take place. For example, surface energies might strongly depend on temperature [69].

Hence, another approach to investigate coarsening phenomena and possible kinetic limits of (001)CGO nanoislands could base on oxidizing heat treatments at T>1000ºC.

Formation of very long (011)-wires (~ μm) within short annealing periods (<30 min) is difficult to explain without considering extremely high mobility of atoms in the present system. Attractive interaction between nanowires has been proposed as a mechanism enhancing mobility of (011)-nanowires. Experimentally, enhancement of atomic diffusion was proved to occur through high temperature annealings in reducing atmosphere (section 5.3 and 5.4). These two growth conditions, together with the presence of (011)CGO nanoislands and the probable attraction between them, seem to lead to a particular landscape where ultrafast mobility is rapidly achieved. These might be the driving forces, but we should still investigate the particular kinetic mechanisms taking place. Particularly, we propose to explain ultrafast mobility as a result of the simultaneous performance of different coarsening phenomena. The observation of the time evolution of nanostructures with different shape (assumed (001) and (011)) (especially section 5.2.2.1) allows us to propose more than six different kinetic paths that can occur at the same time. These different coarsening mechanisms can be mainly classified into two groups.

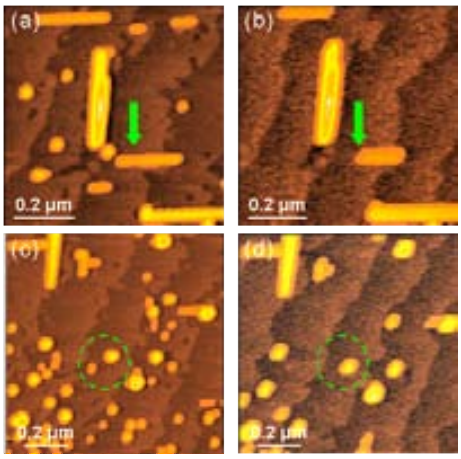

Fig. 6-33: Examples of asymmetric Ostwald ripening between (011)-nanowires (a,b); and conventional Ostwald ripening between (001)-nanodots (c,d). Each pair of snapshots is separated by 5 min anneal at 1000ºC in Ar-H_2.

First, Ostwald ripening mechanisms are continuously taking place. It implies the dissolution of smaller (011) and (001) islands towards larger (011) nanoislands without previous contact. However, in the present system, this mechanism is probably accelerated by the existence of anisotropic strain media. Prove of that are the asymmetries detected in the dissolution of islands, as it is illustrated in the AFM images of Fig. 6-33a and b. Notice in this two consecutive snapshots that the dissolution of the "horizontal" wire occurs faster close to the orthogonal wire than in the opposite end, as indicated by the arrow. These observations support our conclusion about the existence of attractive fields among (011)-nanowires. It must also be

noticed that, according to previous analyses and, contrary to conventional Ostwald ripening, we are not dealing with a typical system where surface energy must be reduced to minimize the total energy. Instead, the goal is to make (011)-nanowires longer to reduce the total energy of the system, as determined thermodynamically. On the other hand, a typical Ostwald ripening mechanism seems indeed to describe the evolution of the isomorphic (001)-nanoislands formed at the first evolution stages during annealing under Ar-H_2 atmosphere, and prior to being engulfed by (011)-nanowires, as it is illustrated for instance in Fig. 6-33c and d.

Second, dynamic coalescence between nanoislands might also occur. This mechanism consists of the diffusion of the whole island across the substrate till it collides with other islands and coalesces; and it has been previously described for example in homoepitaxial (001)Ag growth [49]. Experimental observations suggest that this behaviour can occur via distinct paths. Nanolabyrinthine clusters formed after the junction of perpendicular nanowires hint dynamic coalescence of orthogonally in-plane oriented nanowires. Wire's formation after the impingement of smaller wires aligned along a single particular direction is another possibility. Dynamic coalescence of both wires and dots along a single direction might as well result into elongated islands in that direction. Distinct images suggesting these processes are displayed in Fig. 6-34. Notice that the lack of homogeneous height witness that the long nanowires have originated from several individual smaller nanoislands which have assembled together; they are in a situation of "quasi-equilibrium" which will result in homogeneously high nanowires in the equilibrium. Dynamic coalescence could also explain the diffusion of (001)-dots towards (011)-wires observed, for example, in Fig. 5-35. Attractive interaction between islands could be the driving force for dynamic coalescence.

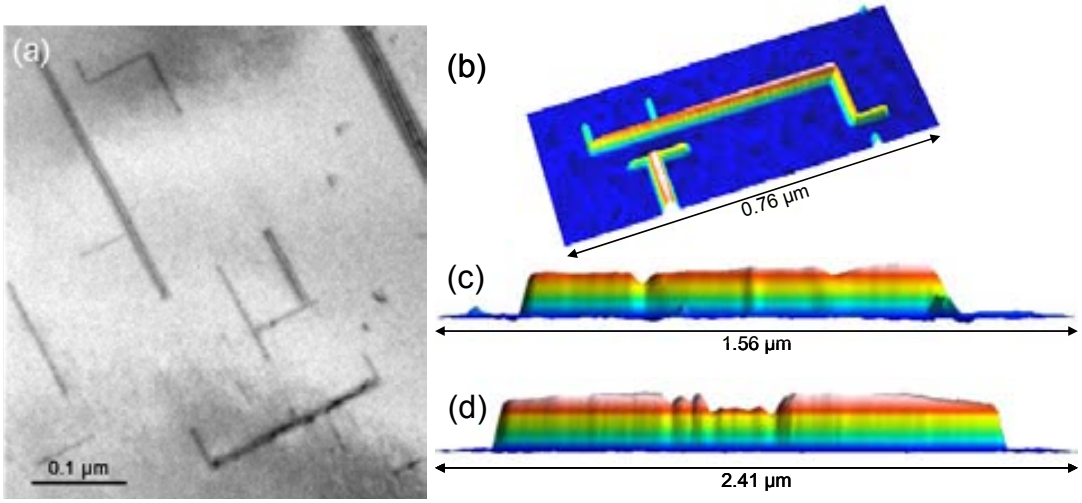

Fig. 6-34: TEM planar-view (a) and AFM images (b,c,d) suggesting dynamic coalescence of nanowires oriented orthogonally (a,b) and parallel to a single <100> direction (c,d). Heigh modulation in 3D profiles (c,d) suggest that these elongate nanostructures are formed after the junction of several nanoislands.

An intermediate situation between atomic or island diffusion can also be suggested after the observation of Fig. 6-35a, where mass transport between islands seems to occur through the flux of nanometric islands. However, this snapshot could also signal dissolution of a previous existing orthogonal nanoisland towards neighbouring islands.

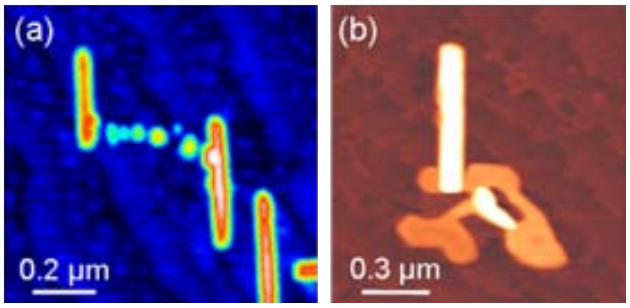

Fig. 6-35: Mass transport between wires as nanometric islands (a). Reconstruction of coalesced wires based on the complete distruption of the smaller wire (b).

Moreover, modified static coalescence can neither be neglected. As nanowires elongate, the probability to collide between each other is not null at all. We refer to this mechanism as modified static coalescence because interfacial nanoislands do not grow from supersaturation but they get in contact with each other owing to elongation processes arising from the particular thermodynamics of the island. These processes might explain nanolabyrinthine structures of (001)-nanowires, where there is not attraction-based driving force yielding to their coalescence.

Independently of the mechanism followed, after the incorporation of atoms or attachment of a whole island, the nanowire in "quasi-equilibrium" configuration reconstructs to achieve the configuration of lowest energy corresponding to the new island's volume. Interfacial atomic diffusion arises as the most common mechanism to achieve that. As a result, a unique homogeneous (width, height) larger nanowire is generally formed when the annealing time is long enough to achieve the equilibrium shape for the corresponding island's volume. For orthogonal (011)-wires, however, another possible reconstruction path is suggested by image in Fig. 6-35b, based on the complete disruption of the smaller nanowire to attach to the largest one. This process, though, probably involves a significant surface energy on the intermediate state and hence it might have a low probability to occur.

Actually, the kinetic evolution of impinged nanowires is more complex and it is influenced by the local structure of the interfaces. TEM details of orthogonal (011)-nanowires reveal that lateral impingement with partial penetration may occur, as exhibited in Fig. 6-36a. As a result, 45^{o} grain boundaries joining (100) and (110) CGO planes of both (011)-nanowires would form this interface. This configuration should be fairly energetic and, thus, deeply

unstable. However, for the case of two orthogonal nanowires attached through their vertex, the interface actually is formed at 45° and, hence, they join through the same (111) planes (Fig. 6-36d, e and f). So, there is no grain boundary in this orthogonal configuration which means that the interface energy is null. This feature could explain the observation of so many nanowires impinged through their vertices in a 90° configuration, as illustrated in Fig. 6-34a. Let's notice that for (001)CGO nanowires the impingement in either of these two orthogonal configurations yields to interfaces formed by the same family of planes, (110) or (100), which results in no grain boundary in both cases. Hence, the null interface energy for these two configurations for (001)-wires is another example of the lack of driving forces leading their reconstruction, which might explain the achievement of such extraordinary lengths.

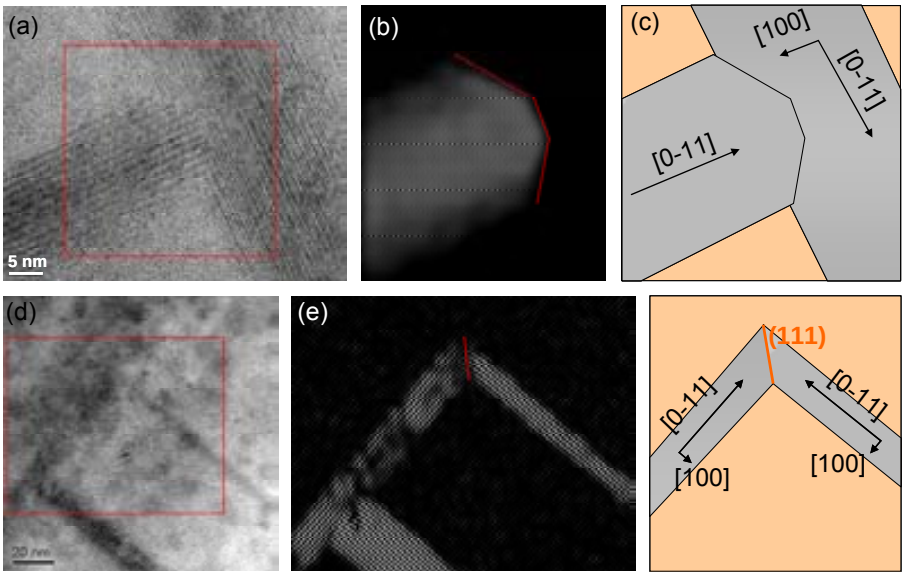

Fig. 6-36: TEM planar-views showing the impingement of orthogonal (011)-nanowires joined together through their short and long axes (a) and through their short axes in a 90° configuration (d). Corresponding IFFT (b,e) images and schematic draws (c,f) help to visualize these configurations.

Hence, the ultrafast mobility leading to the formation of extremely long (011)CGO wires in brief annealing periods in Ar-H_2 can be attributed to the additive effect of the different coarsening mechanisms, the acceleration associated to the attractive interactions and, finally, the island reconstruction to minimize the total energy. Notice that these processes do not apply to (001)CGO wires. To conclude we have proposed different kinetic mechanisms extracted from a large number of static snapshots signalling the evolution of CGO nanoislands. To achieve a thorough understanding of the kinetic processes involved, it would be required the use of more advanced experimental tools, such as in-situ high temperature real time STM or AFM facilities [274-277], or calculations based on kinetic Montecarlo methods [278]. In-situ analyses face the difficulty to work at the high temperatures required for the formation and evolution of these oxide nanostructures, i.e. 800°C - 1000°C. Montecarlo algorithms would yield to the correct

evolution of a non-equilibrium system by accepting and rejecting transitions with a determined probability. Assuming the existence of an already nucleated island and a collection of processes with a determined rate to happen (i.e., attachment of surrounding atoms, interaction with fields generated by other islands, etc), one could study the evolution of the system and analyze the relevance of different processes to the observed landscape.

6.7 Conclusions: *requirements for the formation of nanowires*

The analyses of the presented results for CGO nanoislands' growth on LAO substrates allow us to prepare a general layout of the requirements that we have observed that must be fulfilled for the formation of elongated CGO nanostructures on LAO substrates. They can be summarized in the following points:

1) Surface energy cannot be a handicap for island's elongation; particularly, it is highly interesting that the extra surface energy decreases as lateral aspect ratio c increases. On the other hand, anisotropic surface energies are as well important to promote elongation, since maximization of lateral facets of lower surface energy would be enhanced. These conditions can be satisfied by choosing the appropriate materials (ratio between surface energy of the deposited material and substrate), as well as selecting the crystallographic orientation of the islands. In our case, the selection of the crystallographic orientation of islands is achieved through the modification of growth conditions; but the exact mechanism leading to the nucleation of one or other orientation is unknown. Close interfacial energies of the (001) epitaxy and (011) domain epitaxy could be a key feature for this phenomenon. Some works have related the nucleation of different crystallographic orientations to distinct reconstructions of the substrate surface. For example, this origin has been attributed to the different orientations in the Pd/(001)STO system [21]. The reconstruction of substrate's surface might change the relative stabilities of interfacial planes and, thus, interfacial energies.

2) Elastic relaxation has to favour elongation. Thus, anisotropic epitaxy is required, since force monopoles arising due to misfit will promote elongation along lower lattice mismatch direction. Strain can be tuned through lattice mismatch by selecting materials to achieve the desired misfit, but through crystallographic orientation as well.

In principle it could not be essential that both energetic contributions (E_{suf}, E_{relax}) favours elongation. Actually, it could be enough that the trade-off between them points in that direction. Nonetheless, a system where elongation along lower misfit strain direction simultaneously enlarges the facets with lower surface energy enhances the formation of nanowires with high lateral aspect ratios.

3) Coarsening phenomena might also enhance elongation. The decrease of energy density as islands' volume increases, together with higher equilibrium lateral aspect ratio as volume increases, help to maximize elongation processes.

4) High atomic mobility is important; kinetic mechanisms cannot limit the evolution of the system towards its equilibrium structure. Despite the existence of very long islands, atoms must be able to easily diffuse along wires. Particularly, it has been proved that generation of atomic vacancies and high temperature treatments are distinct ways to promote enhanced kinetics. Simultaneous performance of many distinct kinetic mechanisms also favours coalescence and, thus, reconstruction of nanowires into longer ones. Moreover, interfaces of two dissimilar structures may also help because of vacancies that are formed as defects.

5) Attractive interaction between islands is also a potential way to increase the kinetics of the system in evolution. Though not a requirement, the attractive interaction among nanoislands definitively fosters a strong acceleration of the nanoislands' coarsening and, hence, of the nanowire's in-plane growth.

All these requirements apply to our model system CGO/LAO. Recalling results presented in section 6.3, it is clear that (011)-nanowires satisfies all five conditions. (011)CGO nanowires exhibit anisotropic surface energies and are biaxial anisotropic strained. Thus, both surface energy (which shows its energy minimum at $c=\infty$) and elastic relaxation energy promotes island's elongation since nucleation as a mechanism of energy minimization. Anisotropic shape of nanowires has a thermodynamic origin. There exists also continuous coarsening. High mobility is also guaranteed by the high number of oxygen vacancies generated through the use of reducing atmosphere and heat treatments at high temperature and the dissimilar perovskite-fluorite structures involved, in addition to Gd-doping. The singular attractive interaction proposed among specific nanoislands is a key issue for the fast growth observed. Moreover, ultrafast kinetics of the system as a result of the simultaneous action of distinct processes also seems to be a key point.

In contrast, the symmetry of lateral facets and strains in (001)-islands do not allow to satisfy first and second conditions; and coarsening is neither favoured. All these arguments favour isomorphic shape. Actually, thermodynamic-based calculations have proved that isomorphic in-plane shape corresponds to the lowest energy morphology for (001)-CGO nanoislands with $D \leq 50$ nm; and we have also demonstrated the existence of an equilibrium nanodots' size. Concerning kinetics, (001)-nanodots exhibit very limited evolution under typical oxidising conditions, probably associated to their thermodynamic stability and the existence of repulsive interaction between islands. Just above a critical size D_c, strain energy of (001)-dots might drive the islands to adopt a rectangular elongated shape. Experimentally, just very singular treatments could drive (001)-islands to grow beyond D_c, indicative of the existence of

growth conditions where unstable ripening might occur and which are worthy of being investigated in more detail.

These are the conditions found to take place in the rapid formation of highly anisotropic (011)CGO nanowires on LAO substrates. Maybe they are not all of them essential; perhaps in some cases ones can compensate the others. For example, we have also observed that under particular growth conditions (001)-nanowires might also develop. Nevertheless, these set of conditions establish a starting point for the requirements that must be considered for the formation of elongated structures in other systems.

Chapter 7

Vortex pinning in interfacial nanostructured YBCO thin films

Epitaxial YBCO thin films present high critical current densities (J_c), one or two order of magnitudes higher than any other form of the material [134]. These high critical current densities are due to the great variety and quantity of defects present in thin films, which are naturally generated during the film growth process itself and act as effective centres for vortex pinning. Each kind of defect acts preferentially in a specific range of temperature T and magnetic field H and, in general, their effectiveness decrease at high temperature as consequence of thermal activation [279, 280]. This represents an important handicap for applications of superconducting thin films which requires high J_c at high temperatures and high magnetic fields [128, 281]. Furthermore, naturally generated defects have the drawback that cannot be easily tuned to act efficiently in the H-T range required in specific applications. Therefore, one of the main goals in YBCO thin films is to look for strategies of nanoengineering to design materials with great performance in the chosen magnetic field and temperature region. Particularly, one of the great challenges is to improve vortex pinning at elevate temperatures and high magnetic fields by introducing artificial pinning centres, now that coated conductors are a reality [132, 281]. Several approaches have been investigated to generate artificial arrays of defects within the superconducting matrix: compositional modifications with second phase $BaZrO_3$ (BZO) [140-142, 144, 282] or $BaSnO_3$ [283, 284], multilayered YBCO with second phase materials [139, 143, 285], rare earth doping [286, 287], nanostructuration of the substrate prior to deposition [115, 116, 147, 288], etc. Most of these strategies are based on vacuum related growth techniques (i.e. PLD), but distinct approaches based on chemical solutions arises as reliable low-cost alternatives. For example, through the generation of nanodots of BZO [144] or $BaHfO_3$ [289] within the YBCO matrix, the so called MOD nanocomposites. In particular, the nanocomposites of BZO [144] grown from chemical solutions have demonstrated to exhibit the highest critical current densities and pinning forces with no angular dependence in any superconducting material.

In addition, the knowledge of the pinning landscape induced by the overlap of defects is essential if one intends to provide powerful information for the design of materials with high pinning performance. Hence, new routes for the improvement of vortex pinning and the theoretical comprehension constitutes two major challenges for further development of YBCO films and coated conductors.

In this work, a new strategy for the preparation of CSD nanostructured YBCO thin films is presented, based on the growth of YBCO films by MOD-TFA on the solution-derived CGO/LAO nanostructured templates studied in this thesis. It is expected that nanoislands induce extra defects in the superconductor film which enhance pinning efficiency. This strategy constitutes an innovative strategy to nanoengineer YBCO thin films, above all because we are dealing with an all-chemical approach. In vacuum deposition techniques it has been proved that interfacial oxide nanoislands such as Y_2O_3 [117], CeO_2 [116] and $SrTiO_3$ [147] improve the performance of YBCO thin films grown on top, usually generating additional correlated pinning along c-axis direction. The presence of PLD-grown Y_2O_3 nanoislands (with equivalent thickness of 0.2 nm) enhance J_c from 1.8 to 2.7 MA/cm^2 at self-field and from 0.06 to 0.10 MA/cm^2 at H||c=5 T since nearly all yttria nanoislands generated an artificial pinning centre in the PLD-grown YBCO matrix [117, 145, 290]. The high J_c peak observed for H||c in YBCO-PLD films on annealed CeO_2 buffer layers with dots has been related to threading dislocations probably induced by CeO_2 nanoislands and to egg-shaped nanometric precipitates elongated along c-axis of YBCO [116, 291]. The appearance of outgrowths on STO buffer layers when changing PLD deposition conditions induce tilt grain boundaries in YBCO films as thick as 5 μm which yield to an extra-correlated pinning along c-axis, resulting into better in-field performance for H||c but decrease of J_c at self-field [147, 292]. Decrease of J_c for H||ab has also been observed in these samples and related to buckling of ab planes close of intergrowths. Combined YBCO-PLD deposition on top of chemically-processed interfacial MgO or BZO nanoislands have also resulted into significant improvement of flux pinning capabilities [288]. In this case, the increase of J_c for all field orientations indicates that pinning improvement is fairly isotropic. TEM cross-section images point out distortion of YBCO planes around interfacial nanoislands and a number of stacking faults and intergrowths within the YBCO film, whereas preferential c-axis defects has not been detected. Equivalent results have been observed for the case of sputter deposited particles on STO substrates [146, 288].

In this chapter, a brief introduction to vortex pinning in YBCO thin films is initially presented followed by a basic characterization of prepared interfacial nanostructured YBCO-TFA films. Then, a deep experimental analysis of vortex pinning mechanisms is pursuit for a wide range of temperatures, magnetic fields' intensities and orientations. Finally, a study of the

vortex pinning properties as function of thickness is carried out by designing a thinning process based on Focused Ion Beam (FIB). The evolution of the vortex pinning properties as getting closer to interfacial oxide nanoislands is analyzed.

7.1 Vortex pinning in YBCO thin films

The naturally generated defects during YBCO thin film growth are usually the main responsible for the large critical currents displayed by these films. Nature and origin of these defects is varied, including for example oxygen vacancies, non-superconducting precipitates, dislocations, twin boundaries, grain boundaries, staking faults or intergrowths [132]. Hence, the pinning behaviour of YBCO thin films with temperature and magnetic field depends on the combined performance of the distinct kinds of pinning centres present. There exist a large variety of models to explain vortex pinning. However, each model describes the behaviour of the system in accordance with one particular sort of defect, and there still does not exit a model capable of describing the behaviour of multi defects which actually is what our system has. Thus, a general classification is needed to facilitate comprehension and further design of the whole pinning landscape of real materials. A common categorization is based on the dimension of the pinning sites: point defects (size ~ coherence length ξ) [122], extended linear or planar (correlated) defects (1 dimension ~ ξ) [124] and extended point defects (size > ξ). Oxygen vacancies (0D) are a sort of point defect, dislocations (1D) or stacking faults (2D) are examples of extended defects, and precipitates are examples of extended point defects. It is well-established that the point defects follow the intrinsic mass anisotropy of the material whereas extended ones do not. Therefore, one can classify them into isotropic and anisotropic pining centres [293, 294]. Isotropic defects are those whose vortex pinned length does not depend on the relative orientation of the magnetic field (i.e. follow the intrinsic mass anisotropy); point defects are the most representative example. Contrary, anisotropic defects are those whose vortex pinned length indeed depends on the orientation of the magnetic field; linear defects such as ion irradiated columnar tracks are a typical example [138].

In accordance with experimental measurements, and despite the diversity of models owing to the high complexity of real materials, all them coincide with the existence of three distinct regimes in the behaviour of critical current density as function of the applied magnetic field, $J_c(H)$ [122]. These regimes essentially depend on the relative importance of vortex-defect and vortex-vortex interaction in each case, despite they can be strongly influenced by thermally activated processes specially when working at high temperatures.

At low magnetic fields, the vortex-defect interaction dominates over the vortex-vortex interaction. In this regime, the critical current density is independent of the number of vortices,

i.e. J_c does not depend on the applied magnetic field. Thus, this regime is characterized by the critical current at self-field, $J_c(H) \sim J_c(sf)$. This behaviour, known as single vortex pinning, applies to point [122], extended [124] and extended point defects [295]. For linear defects, the system can be modelled assuming the interaction of one flux line with one linear defect. Then, the critical current is obtained by equalling Lorentz-like force to the pinning force

$$J_c B = n f_p \qquad \textbf{Eq. 7-1}$$

where f_p is the pinning force per unit length between a vortex and a defect and $n=1/a_o^2$ is the area density of pinned vortices, being a_o the lattice parameter of the vortex lattice. Taking into account that the applied magnetic field and vortex flux quantization are related as $B=n\Phi_o$, the critical current density is given by

$$J_c = \frac{f_p}{\Phi_0} \qquad \textbf{Eq. 7-2}$$

Thus, the critical current density results to be independent of the applied filed, $J_c \neq J_c(H)$. This behaviour is maintained while vortex density in the superconductor is sufficiently low. As applied magnetic field increases, vortex density also augments. At the applied field H^*, vortices are close enough so that interactions between them are no longer negligible, and vortex-vortex interaction becomes dominant over vortex-defect interaction. The cross-over field H^* depends on the density of defects present in the sample as well as on the pinning strength [122, 296].

In region $H>H^*$, critical current density is typically described by a power law dependence, $J_c(H) \sim H^{-\alpha}$. Theoretical models explain the appearance of the power law dependence through considering the effective elasticity of the vortex lattice in interaction between vortices, i.e. by introducing elastic constants and the ability of each defect to pin distinct vortices [122]. The exponent α can be an index of the type of pinning mechanism; thus distinct values have been proposed depending on the model. For example, it has been suggested that for a pinning mechanism dominated by point defects the exponent α takes the value α=0.5 [297], in a model dominated by extended point pinning centres α=0.6 [295] and in a system characterized by lineal defects α=0.5 or α=1 depending on the mean separation between vortices and defects [124, 296]. Once more, it must be taken into account the high complexity of real materials, which makes difficult to summarize the large variety of pinning centres in just a unique exponent α. Hence, the established models explain efficiently the $J_c(H)$ dependence of those materials where there exists essentially one relevant type of defect. Additionally, it must be noticed that most of the experimental works describing the behaviour of J_c as function of pinning centres and, thus, the related theoretical models, correspond to thin films prepared by vacuum deposition techniques. Thus, literature referring to CSD-prepared YBCO thin films is

limited. This constitutes an added difficulty when dealing with chemically-grown YBCO thin films, since film microstructure is strongly linked to the growth technique. Films grown by PLD show a columnar growth which induces the formation of dislocations which might act as strong pinning centres. Instead, TFA-films are characterized by laminar growth where stacking faults are one of the most representative induced defects [298].

Finally, the third regime is encountered at high magnetic fields where J_c starts to rapidly decrease as the magnetic field increases as consequence of the proximity to the irreversibility line. Thus, critical current density cannot be described any more by a power law dependence. This regime starts at a magnetic field which we call H_2^* [299].

It must be considered that vortex motion is potentially thermal activated, especially in high temperature superconductors due to the large thermal energies involved [279, 280]. Therefore, the ideal E-J relation in type II superconductors shown in Fig. 7-1a is rounded by thermal processes, as depicted in Fig. 7-1b. Three distinct regimes of resistivity can be distinguished depending on the current density considered. For currents densities $J<<J_c$, the system is considered in equilibrium and the electrical field is proportional to the current density; this regime is referred to as thermally activated flux flow. For $J\sim J_c$, the electrical field increases exponentially with current; this regime is known as flux creep regime and it is characterized by an attempt frequency of vortex hopping from one to another pinning centre. For $J>>J_c$, the pinning force is much weaker than the driving force for motion and the flux flows steadily, being called flux flow regime.

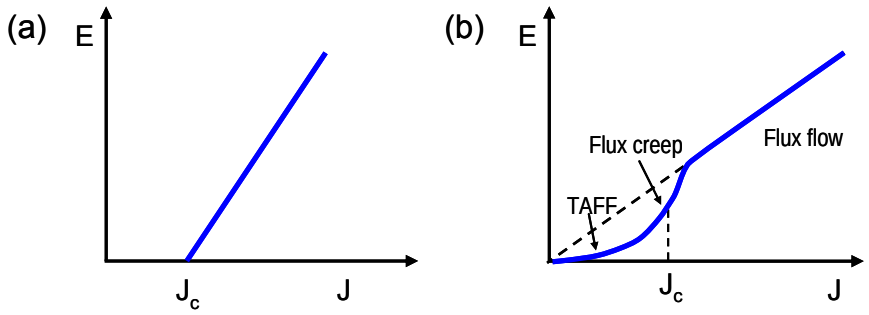

Fig. 7-1: Schema of the electric field as function of the current density in type II superconductors at T=0 K (a) and in the presence of thermal activation depinning (b).

Fig. 7-2 shows a log-log plot of the typical dependence $J_c(H)$ at several temperatures of a standard YBCO-TFA thin film of ~275 nm thick grown on a LAO single-crystal when the field H is applied parallel to the crystallographic c-axis of the film. We will refer to this sample as TFA_{std}. The three distinct $J_c(H)$ regimes described above are clearly distinguished at all temperatures; grey dotted lines delimit each region. For example, at 77 K the critical current density at self-field, $J_c(sf)=3$ MA/cm^2, holds till $\mu_o H^*=0.015$ T. Then, for $H>H^*$ till $\mu_o H^*\sim 0.8$ T,

J_c can be fitted with a power law $J_c(H) \sim H^{-\alpha}$ with α=0.75; which is observed as a linear dependence in the log-log plot. For MOD-TFA YBCO films grown at ICMAB, it has been proved that the defects responsible of J_c at self-field are isotropic pinning centres [294].

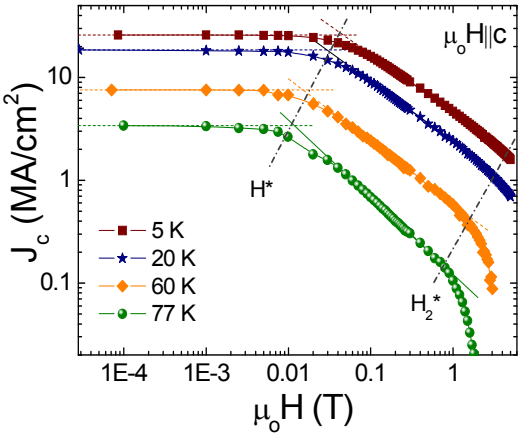

Fig. 7-2: Inductive SQUID-measurements showing the dependence of the critical current density J_c with magnetic field H applied parallel to c-axis at 5 K (■), 20 K (★), 60 K (♦) and 77 K (●) for the standard sample TFA_{std}. Distinct $J_c(H)$ regimes are separated by dotted lines indicating H* and H_2^*; and colour dashed lines shows the power law fit at each temperature.

This basic behaviour of $J_c(H)$ dependence in YBCO thin films is observed all over the range of temperatures of superconducting state, though characteristic parameters such as power law exponents α or cross-over fields H^* are function of temperature, among other features. Therefore, further information of vortex pinning landscape can be extracted from the behaviour of $J_c(H)$ with temperature.

The dependence of critical current density with temperature $J_c(T)$ enables to classify defects as function of their strength as vortex pinning centres [293, 294], since $J_c(T)$ dependence is heftily related to the thermal activation energy associated to these defects [279, 280]. A very fast $J_c(T)$ decay is observed when thermal activated processes are very active, i.e. thermal activation of vortices from pinning sites is very important. That is the case of point defects, an example of weak defect. On the other hand, thermal activation energy is reduced for the case of extended defects (linear, planar) because they are able to pin a larger length of vortex, making more difficult to depin vortices from these defects. Consequently, $J_c(T)$ decay is smoother for strong pinning centres.

In the frame of weak vortex pinning [122], each magnetic flux line is considered to elastically deform to accommodate itself within many point-like defects, such as oxygen vacancies. This pinning mechanism leads vortex motion in the absence of strong pinning; and, as mentioned above, J_c dependence with temperature is strongly related to classical flux creep. Models describing the behaviour of YBCO thin films under the presence of defects acting as weak pinning centres predict a dependence of critical current density with temperature as

$$J_c^{wk}(T) \approx J_c^{wk}(0)\,\exp\left(-\frac{T}{T_o}\right) \qquad \textbf{Eq. 7-3}$$

where $J_c^{wk}(0)$ is the weak pinning contribution to J_c at T=0 K and T_o is the characteristic temperature which fixes the range of energies of weak pinning centres. The temperature and magnetic field range of applicability of this model is up to 60 K and 6 T, respectively [122].

For a vortex pinning mechanism due to correlated defects such as columnar or planar defects like bulk dislocations or twin boundaries, Bose glass theory is the model describing the dependence of critical current density with temperature [124]. According to this theory, $J_c(T)$ is given by

$$J_c^{str}(T) \approx J_c^{str}(0)\,\exp\left[-3\left(\frac{T}{T^*}\right)^2\right] \qquad \textbf{Eq. 7-4}$$

where $J_c^{str}(0)$ is the critical current density at T=0 K and T^* is the characteristic pinning energy of vortex pinned in correlated defects. The region of applicability of Eq. 7-4 comprises temperatures $T< 0.76T_c$ (i.e. T~70 K for YBCO) and magnetic fields below $B_\Phi \approx n_i\Phi_0$, where n_i is the area density of correlated defects. Let's notice that $J_c(T)$ dependence of strong pinning sites exposed in Eq. 7-4 effectively decreases smoother with temperature than Eq. 7-3 referring to weak defects.

Nonetheless, due to the complexity that characterize real materials, both contributions are in general required to describe the dependence $J_c(T)$ in YBCO thin films. Fig. 7-3 shows a typical inductive measurement of J_c dependence with temperature of the standard TFA_{std} thin film at $\mu_oH||c$=0.7 T. Successful fit of $J_c(T)$ experimental data is achieved taking into account both contributions, i.e. weak and strong pinning centres. Weak pinning contribution governs the critical current density at low temperatures, whereas strong pinning contribution dominates at high temperatures.

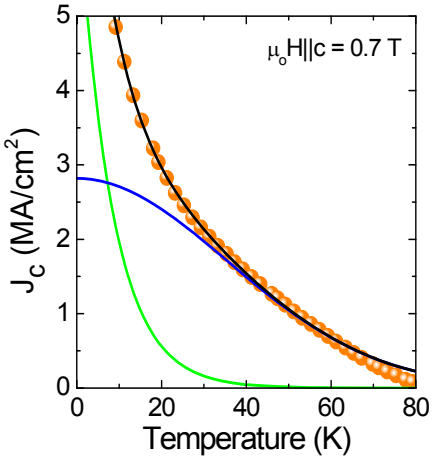

Fig. 7-3: Inductive SQUID measurements of critical current density J_c dependence with temperature at $\mu_oH||c$=0.7 T for the standard TFA_{std} thin film. Green line is a fit to Eq. 7-3, blue line is a fit to Eq. 7-4 and black line is the fit resulting from the sum of both pinning contributions.

A new methodology has been developed at the ICMAB superconducting group to classify the vortex pinning centres existing in YBCO thin films according to its dependence with magnetic field orientation and to its strength as pinning sites [157, 293]. This method based on transport $J_c(\theta,H,T)$ measurements (where θ is the angle between the crystallographic c-axis and the applied magnetic field) will be introduced in detail and used in following sections.

7.2 Interfacial nanostructured YBCO-TFA thin films

In the present work, interfacial oxide nanostructured templates are used as a template for the growth of YBCO thin films in order to induce defects in the superconducting matrix which are expected to act as effective vortex pinning sites. In subsequent studies, (001)LAO single-crystal substrates with interfacial CGO nanoislands (either dots or wires) are used as templates; control and reproducibility on the preparation of these nanostructures has been widely proved in previous chapters. As will be pointed out later, both nanostructures (dots and wires) lead to the same pinning landscape characteristics. With the aim to look for an all-chemically prepared nanostructured thin film, YBCO was grown following the MOD-TFA route described in chapter 3. The typical film thickness of resulting YBCO-TFA thin films is ~(275±50) nm, whereas the height of interfacial nanoislands is typically h~8 nm. Schematic representation of this interfacial nanostructured YBCO thin films configuration, i.e. YBCO/CGO islands/LAO, is depicted in Fig. 7-4.

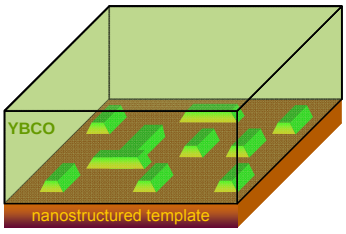

Fig. 7-4: Schematic representation of an interfacial nanostructured YBCO thin film superconductor: YBCO/interfacial oxide nanoislands/substrate.

Fig. 7-5a displays a typical XRD^2 diffraction pattern of an interfacial nanostructured YBCO-TFA thin film with interfacial (011)CGO nanowires, i.e. YBCO-TFA/ CGO-nanowires/ LAO. We refer to this sample as TFA_{WIRES}. Due to the small amount of CGO present in the template, it is not possible to detect it through standard XRD^2 measurements. The peaks appearing at 23.4^o and 47.9^o belong to the (00ℓ) reflections of LAO single-crystal substrate. The other sharp peaks correspond to the (00ℓ) reflection of YBCO, indicating that the superconducting film grows c-oriented on top of nanostructured template. Moreover, the lack of diffraction rings in the 2θ-χ patterns and Φ-scan of (102)-YBCO (Fig. 7-5c) point out an epitaxial (00ℓ)YBCO orientation.

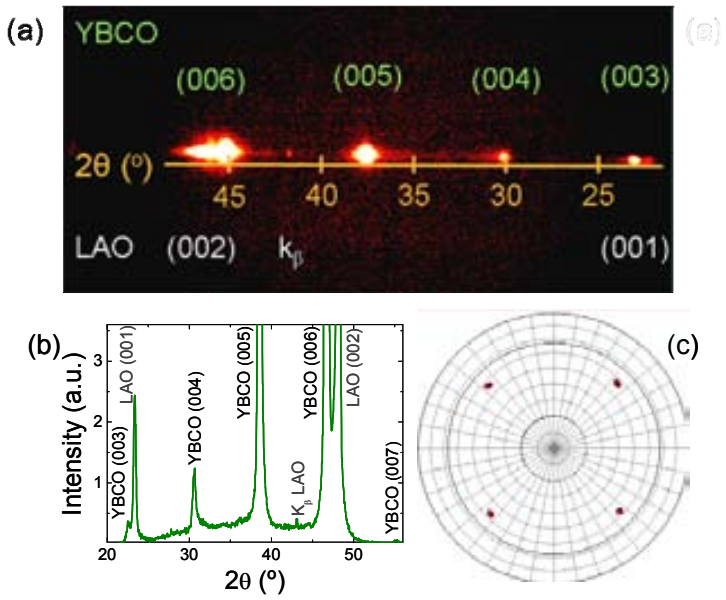

Fig. 7-5: XRD^2 measurements of the interfacial nanostructured YBCO-TFA thin film TFA_{WIRES}: 2θ-χ frame (a), where the horizontal axis corresponds to 2θ and the vertical one to χ; corresponding integration in χ (b); and ϕ-scan of (102)-YBCO represented in polar coordinates (c).

However, SEM images show that interfacial nanostructured YBCO-TFA thin films present a high amount of ab-planes indicated by the elongated white needles in Fig. 7-6, which corresponds to SEM images at different magnification of sample TFA_{WIRES}. From these images it is also derived that nanostructured YBCO films are very dense since just few pores are observed close to ab-grains.

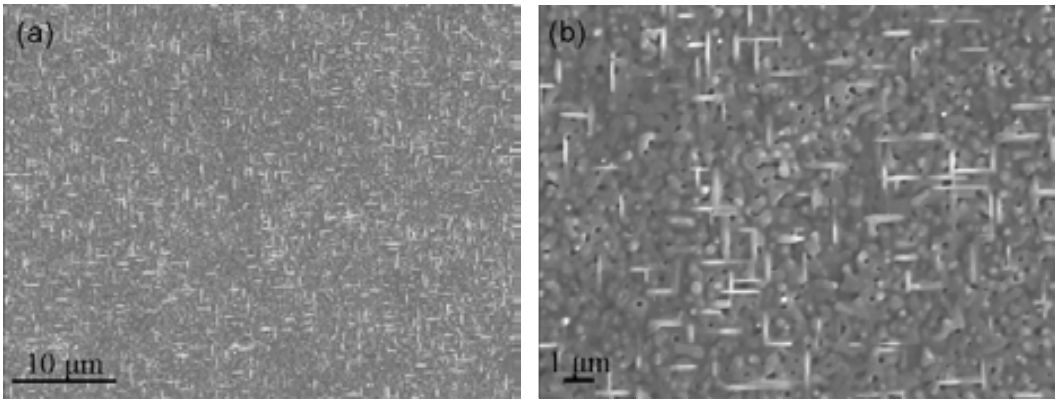

Fig. 7-6: SEM images of the interfacial nanostructured YBCO-TFA sample TFA_{WIRES}. Images correspond to magnifications x2000 (a) and x6000 (b).

To deeply investigate the presence of ab-grains, XRD^2 measurements were carried out centred at $\chi=35^o$. This configuration enables to simultaneously detect the (102)-YBCO reflections from c-axis oriented grains and ab-oriented ones. The corresponding 2θ-χ frame is displayed in Fig. 7-7a. The intense peak observed at $2\theta=27.9^o$ and $\chi\sim56^o$ corresponds to the (102) reflection of grains (00ℓ)-YBCO. At same 2θ, a second peak is detected at $\chi\sim32.2^o$. It corresponds to the population of ab-grains present in interfacial nanostructured YBCO thin

films. Integration of the diffraction intensity reveals that YBCO domains with (ℓ00) or (0ℓ0) planes parallel to the substrate (001)LAO represent at maximum ~16% of the total film volume, whereas the remaining volume corresponds to (00ℓ)YBCO||(001)LAO domains. Estimation at maximum is due to the poorer quantification of the intensity of reflection peaks detected at borders of 2D detector with respect to those detected at the centre. The existence of ~16% of ab-planes in interfacial nanostructured YBCO-TFA thin films will not deteriorate the superconducting properties, as we will see in following results.

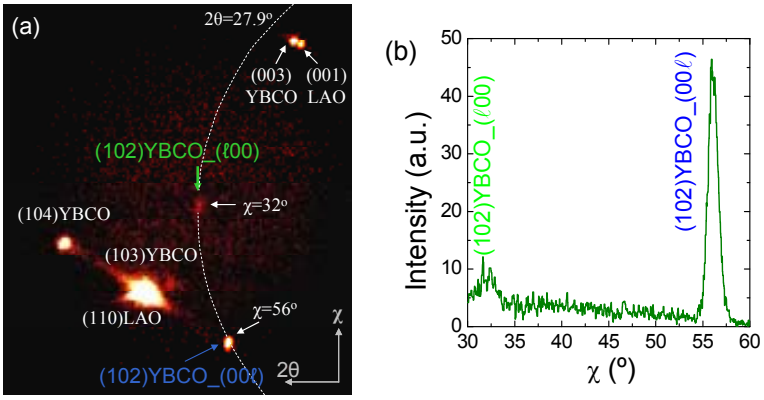

Fig. 7-7: XRD[2] diffraction pattern centred at χ=35º to simultaneously detect the (102) reflections of c- and ab-oriented YBCO grains (a); corresponding integration over 2θ evidencing the difference in intensity between both (102) YBCO reflections (b).

The critical current density as function of temperature is shown for sample TFA_{WIRES} in Fig. 7-8a. These measurements were performed using a SQUID magnetometer and J_c values were calculated from measured magnetic moment applying critical state model [155, 156]. J_c(5K)~15 MA/cm^2 and J_c(77K)~2 MA/cm^2 at self-field indicates the good quality of the interfacial nanostructured YBCO-TFA films and proves the compatibility between chemically-grown interfacial oxide nanostructures and YBCO deposition by the chemical TFA-route even though a fraction of ab-grains is present in these samples. Furthermore, resistivity measurements displayed in Fig. 7-8b show a sharp transition from normal to superconductor state at T_c~91.3 K with ΔT_c~1 K, and reasonable values of ρ(300 K) and ρ(0 K) [215]. So, nanostructured YBCO thin films have the expected critical temperature for YBCO and, thus, T_c is not depressed because of the presence of interfacial CGO nanoislands and the existence of ab-planes.

The values reported referring to J_c at self-field, critical temperature, presence of ab-planes, etc. are representative of all the interfacial nanostructured YBCO-TFA films that we have grown. It is important to remark that the good superconducting properties of these all-chemically grown interfacial nanostructured YBCO-TFA thin films prove not only the capability of CSD to prepare nanostructured superconductors, but also show the potential of this chemical route towards the generation of low-cost coated conductors.

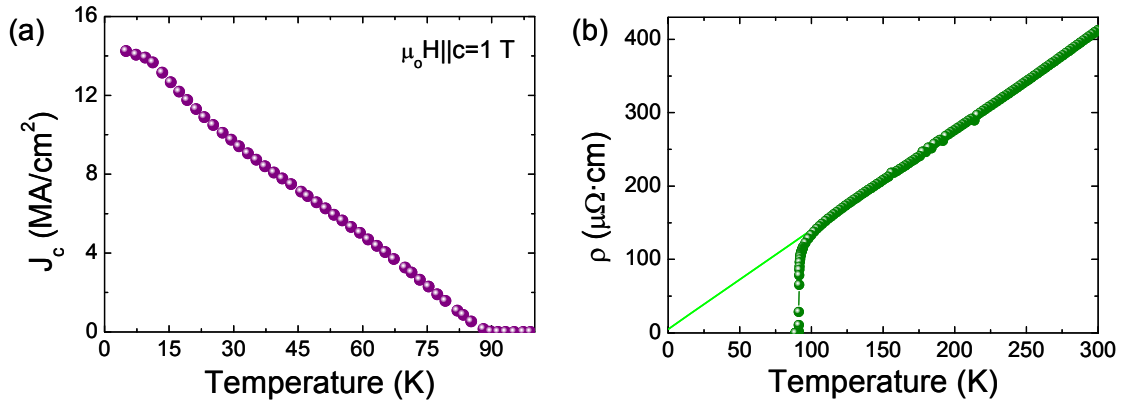

Fig. 7-8: $J_c(T)$ dependence at self-field (a) and resistivity as function of temperature (b) of interfacial nanostructured sample TFA_{WIRES}.

7.3 Vortex pinning of interfacial nanostrucured YBCO-TFA thin films

A critical temperature of ~90 K and the high critical current densities at self-field demonstrate that the presence of interfacial CGO nanoislands has not depressed the basic properties of YBCO thin films. However, it is required to investigate the performance of these nanostructured films in different magnetic fields and temperatures in order to determine the influence of defects induced by oxide interfacial nanostructures on superconducting properties. Consequently, a study of $J_c(H)$ dependence for H||c based on either inductive or electrical transport measurements is presented next. Then, the $J_c(\theta,H,T)$ dependence is examined to complete the vortex pinning analysis.

7.3.1 Critical current density dependence for H parallel to c-axis: Inductive $J_c(H,T)$ measurements

Fig. 7-9 shows a log-log plot of the typical dependence of the critical current density with magnetic field applied parallel to the c-axis for the interfacial nanostructured sample TFA_{WIRES} at different temperatures. Measurements for H||c where performed using a SQUID magnetometer. The three distinct $J_c(H)$ regimes described beforehand are distinguished in the whole investigated temperature regime.

At lower magnetic fields $H<H^*$, the critical current density shows a *plateau* in the log-log plot $J_c(H)$. Thus, this regime is characterized by the critical current at self-field $J_c(H)\sim J_c(sf)$, indicative of a single vortex pinning regime. This behaviour holds till the cross-over field H^*, where there is a gradual transition to a regime ($H^*<H<H_2{}^*$) where J_c starts to decrease with the magnetic field. In this region, $J_c(H)$ is described by a power law $J_c(H)\sim H^{-\alpha}$. For magnetic fields close to the irreversibility line ($H>H_2{}^*$), the critical current density decreases rapidly as magnetic field increases moving away from the power law dependence. Gray dashed lines in Fig. 7-9 indicate the fields where the regime transition takes place, i.e. H^* and $H_2{}^*$.

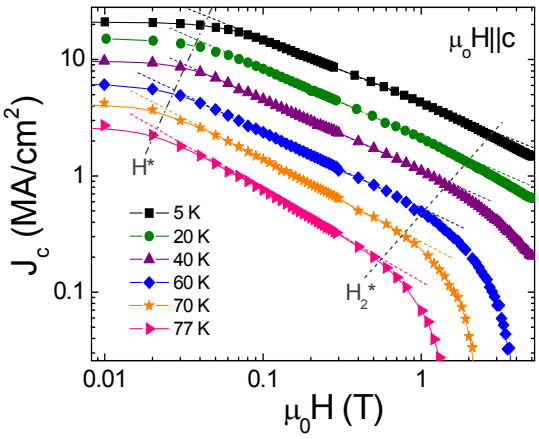

Fig. 7-9: Critical current density dependence with applied magnetic field $\mu_o H||c$ of TFA_{WIRES} at 5 K (■), 20 K (●), 40 K (▲), 60 K (♦), 70 K (★) and 77 K (►). Gray lines indicate the cross-over fields H* and H_2*; and colour dashed lines shows the power law fit at each temperature.

We define the cross-over field H^* at the crossing between the *plateau* and the power law fit. Fig. 7-10a shows the dependence of $\mu_o H^*$ with temperature for sample TFA_{WIRES}. The general dependence of other interfacial nanostructured YBCO thin films analyzed is summarized in the grey band also displayed in the figure. H^* decreases as temperature increases. This dependence is consequence of the relation between cross-over field H^* and the pinning energy of defects [295, 296, 300], since this filed indicates the transition from a regime dominated by vortex-defect interaction to one controlled by vortex-vortex interactions. In the power law regime, the exponent α also depends on temperature as shown in Fig. 7-10b; specifically, α increases with temperature. Distinct reasons have been suggested to explain the dependence α(T). It has been pointed out that it is consequence of a cross over different pinning regimes as temperature increases [124, 296], but it has also been proved that α can change due to the incorporation of extra pinning centres [142, 301] suggesting the dependence of α with type and strength of defects.

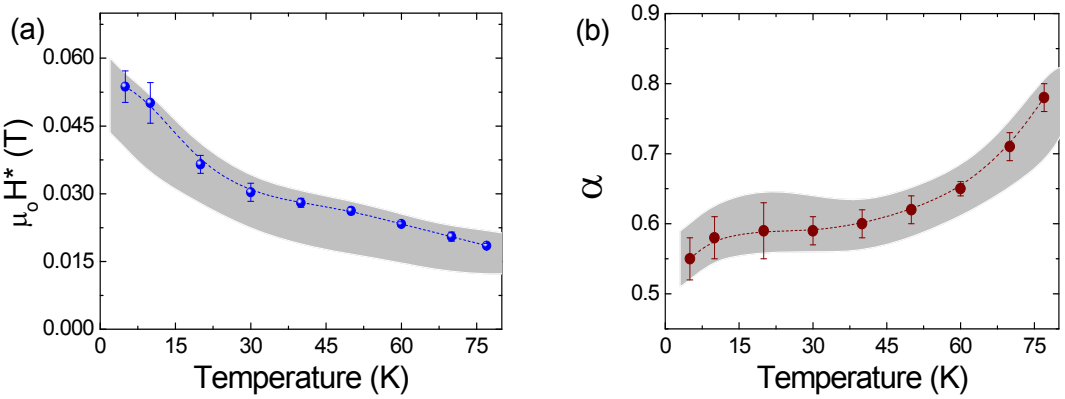

Fig. 7-10: Dependence with temperature of the cross-over field $\mu_0 H^*$ (a) and exponent α (b) for sample TFA_{WIRES} (●); the grey band summarizes the behaviour of other interfacial nanostructured YBCO-TFA thin films analyzed.

Fig. 7-11a compares the dependence $J_c(H)$ at different temperatures of samples TFA_{WIRES} (close symbols) and TFA_{std} (open symbols). We observe that the critical current density at self-field of the nanostructured sample is lower than that of the standard film. This is a characteristic shared by all our interfacial nanostructured YBCO-TFA thin films; analyses of the distinct pinning contributions carried out in subsequent sections will allow us to identify the cause of this decrease. Both samples TFA_{WIRES} and TFA_{std} follow the same trend marked by the three distinct $J_c(H)$ regimes; in general, no significant qualitative differences are appreciated. Observe in Fig. 7-11a that J_c decreases faster for $H>H_2^*$ at high temperature and high magnetic fields for the nanostructured sample compared to the standard one. We notice that in this H-T region (high H, high T) inductive SQUID measurements are strongly influenced by relaxation phenomena associated to flux creep because of the slow time constant of this type of measurements.

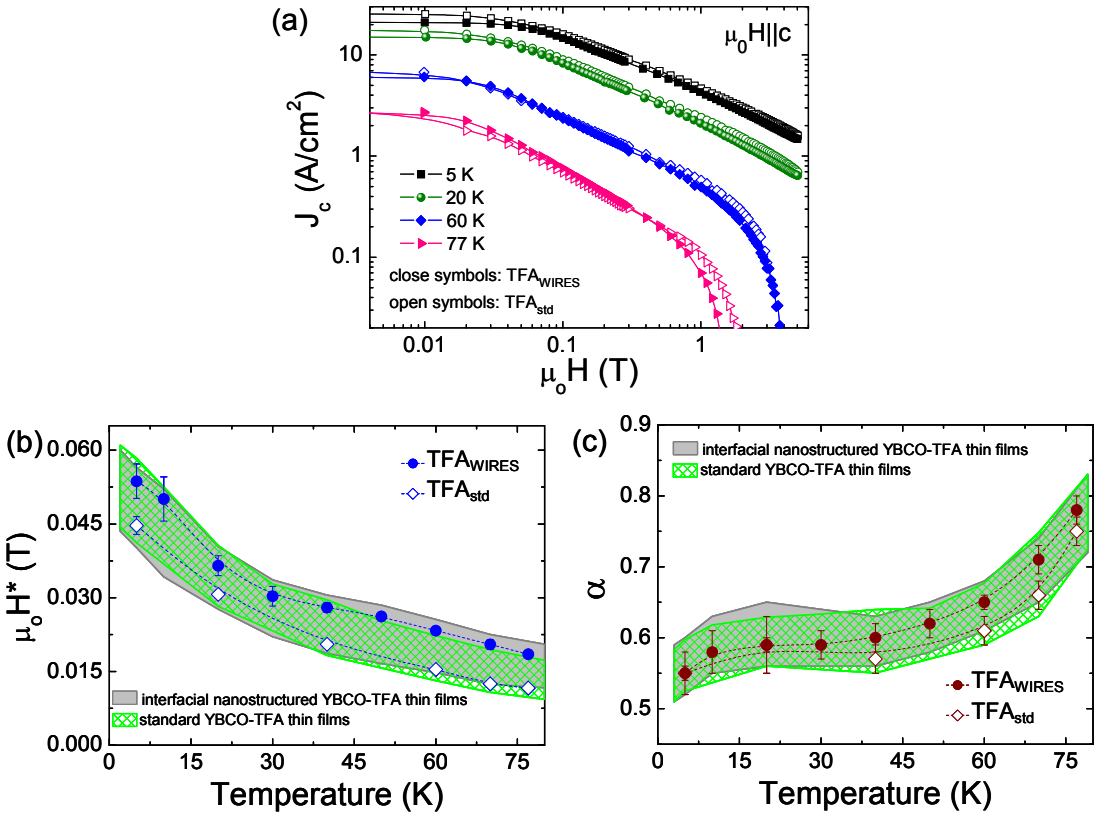

Fig. 7-11: $J_c(H)$ dependence for H||c of samples TFA_{WIRES} (close symbols) and TFA_{std} (open symbols) at 5 K (■), 20 K (●), 60 K (♦) and 77 K (►) (a); and corresponding H*(T) (b) and α(T) (c) dependence. Grey and diamond band summarizes the T-dependence of other interfacial nanostructured and standard YBCO-TFA thin films analyzed, respectively.

In Fig. 7-11b and c we represent the cross-over fields H* and α exponents, respectively, as function of temperature for both samples TFA_{WIRES} and TFA_{std}. For this specific pair of samples, TFA_{WIRES} shows higher H* than TFA_{std}. In contrast, in the power law regime J_c of TFA_{WIRES} is found to decay faster than that of TFA_{std} with the applied magnetic field, as

exemplified by α values in Fig. 7-11c. However, if we compare values of $H^*(T)$ and α(T) for several interfacial nanostructured (grey band) and standard (diamond band) YBCO-TFA thin films we observe that both dependences overlap in most of the cases. So, significant and general differences between the $J_c(H)$ behaviour of interfacial nanostructured YBCO-TFA thin films and standard ones cannot be extracted from inductive measurements. Next, electrical transport measurements will be pursuit to investigate the angular behaviour of J_c with applied magnetic field and temperature, which will evidence significant differences between both sets of samples.

7.3.2 Critical current density dependence for H||c and H||ab: Electrical transport $J_c(H,T)$ measurements

Fig. 7-12 displays the $J_c(H)$ dependence determined from electrical transport measurements at 77 K and H||c for samples TFA_{std}, TFA_{WIRES} and another nanostructured YBCO-TFA film with interfacial (001)CGO nanodots which we refer to as TFA_{DOTS}. First of all, let's point out that both nanostructured YBCO-TFA films show fairly similar magnetic field dependences of J_c for H||c independently of the in-plane anisotropy of interfacial nanoislands, i.e CGO-nanowires or CGO-nanodots, and it is remarkably different from $J_c(H||c)$ of TFA_{std}. So, subsequent analyses (mainly carried out for TFA_{DOTS}) are valid for nanostructured templates with either interfacial nanowires or nanodots. Hence, this indicates that similar pinning centres are induced in the YBCO matrix by both types of interfacial nanostructures.

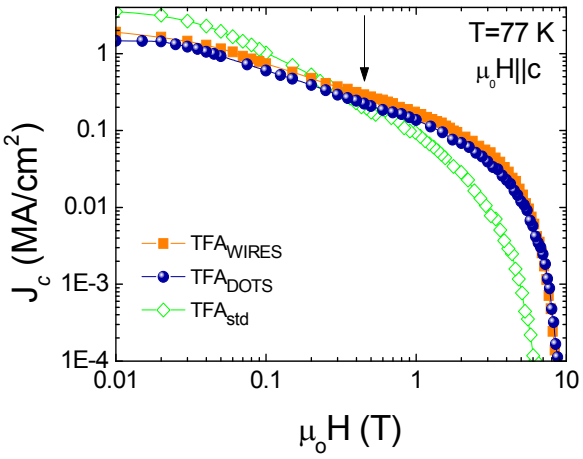

Fig. 7-12: Magnetic field dependence at 77 K for H||c of samples TFA_{WIRES} (■),TFA_{DOTS} (●) and TFA_{std} (◊); data was obtained from electrical transport measurements. The arrow indicates the field where critical current of nanostrucured samples becomes higher than that of the standard sample.

The three distinct $J_c(H)$ previously observed in inductive critical current measurements can also be distinguished now. Results are here presented up to 9 T and with a fast time constant electrical measurement. Clear, differences are appreciated which could not be seen in SQUID measurements up to 5 T. Despite nanostructured films show a lower J_c at self-field, their

dependence with magnetic field is smoother than that of standard sample. This behaviour is illustrated by a lower exponent α for the case of nanostructured samples in the power law regime ($J_c(H) \sim H^{-\alpha}$), i.e. α=0.64 for TFA_{DOTS} and α=0.92 for TFA_{std} at 77 K and H||c. Therefore, interfacial nanostructured thin films result to have a better in-field performance than standard YBCO-TFA samples at high temperature. Moreover, not only $J_c(H)$ dependence is smoother, but the absolute critical current density of interfacial nanostructured films becomes even higher than that of TFA_{std} above μ_oH~0.5 T (this field is indicated with an arrow in Fig. 7-12). For example, at μ_oH=3 T and 77 K, TFA_{DOTS} sample has a $J_c=6.9\cdot10^{-2}$ MA/cm^2, which represents an enhancement of 240% with respect to the standard TFA film.

Let's notice that differences in the in-field performance at 77 K for H||c between nanostructured films and TFA_{std} become especially remarkable at magnetic fields μ_oH>1 T. In this H-T region, inductive measurements are so influenced by flux creep that critical current densities rapidly decrease. That explain why these differences could not be appreciated in SQUID measurements (Fig. 7-11).

The overall improvement of $J_c(H)$ achieved because of the presence of interfacial CGO nanoislands can clearly be seen through the dependence of the pinning force, $F_p=\mu_o(J_c \times H)$, with the applied magnetic field H||c. Fig. 7-13 shows $F_p(H)$ for samples TFA_{WIRES}, TFA_{DOTS} and TFA_{std} at 77 K and H||c. The maximum pinning forces of the nanostructured films are enhanced and shifted to higher magnetic fields. Specifically, F_{p_max}=1.85 GN/m^3 at $\mu_oH_{Fp\_max}$=1.48 T for TFA_{WIRES}, F_{p_max}=1.42 GN/m^3 at $\mu_oH_{Fp\_max}$=1.5 T for TFA_{DOTS} and F_{p_max}=1.09 GN/m^3 at $\mu_oH_{Fp\_max}$=0.36 T for TFA_{std}, which indicates that additional defects have been introduced in interfacial nanostructured films, which additionally display their maximum effectiveness at a much higher magnetic field.

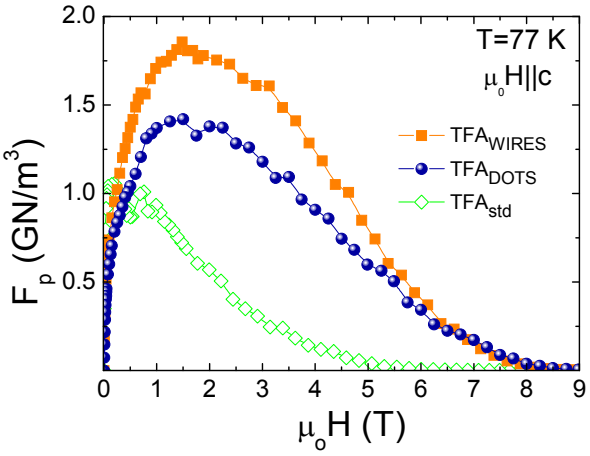

Fig. 7-13: Dependence of pinning force F_P with magnetic field applied μ_oH||c at 77 K for samples TFA_{WIRES} (■),TFA_{DOTS} (●) and TFA_{std} (◊).

An additional distinction in vortex pinning for H||c at 77 K of interfacial nanostructured YBCO films compared to TFA_{std} is given by the irreversibility line. The irreversibility line

separates the region where vortex are pinned in a solid phase from the liquid vortex state where pinning is no more achievable. This transition is strongly influenced by thermal activation processes. Therefore, it depends on the microstructure of the sample and stronger pinning sites would be expected to increase the irreversibility line. Fig. 7-14a displays the irreversibility line of samples TFA_{DOTS} and TFA_{std}. An upward shift of the irreversibility line of the nanostructured sample is observed with respect to the standard film, especially above 1 T. This difference is interpreted in terms of more efficient pinning sites for the magnetic field applied parallel to the c-axis in the case of TFA_{DOTS} [138, 157]. These results are in agreement with the improvement of the $J_c(H)$-dependence for H||c at 77 K (Fig. 7-12) of the interfacial nanostructured films compared to the standard sample. Nonetheless, separation of distinct pinning contributions is required to identify the sort of defects responsible for this behaviour.

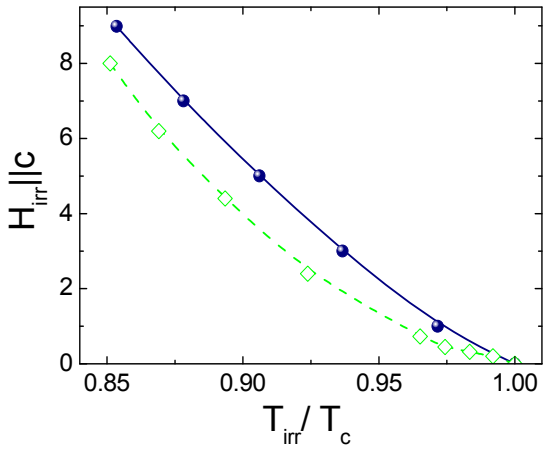

Fig. 7-14: Irreversibility line for H||c of samples TFA_{DOTS} (●) and TFA_{std} (◊).

Thus, through interfacial nanostructuration of YBCO-TFA films we are able to enhance vortex pinning by introducing defects which act effectively when the magnetic field is applied parallel to c-axis. Nonetheless, Fig. 7-15 illustrates that opposite performance is achieved in the same sort of samples when the magnetic field is applied parallel to ab planes. In this H||ab configuration and at 77 K, the critical current density of nanostructured films is always lower than that of TFA_{std}, and it even decreases more rapidly as magnetic field increases. This poorer in-field performance for H||ab at 77 K of TFA_{WIRES} and TFA_{DOTS} compared to TFA_{std} is translated to a decrease of the irreversibility line for interfacial nanostructured samples with respect to standard ones for H||ab. This behaviour could not be specifically measured for our nanostructured samples. Nonetheless, YBCO-TFA thin films grown at ICMAB on top of $La_{0.7}Sr_{0.3}MnO_3$ buffer layers with interfacial $(La,Sr)O_x$ nanoislands that behaved very similarly from the vortex pinning point of view as those presented in this thesis showed an improvement of the irreversibility line for H||c together with a shift downwards of the irreversibility line for H||ab with respect to standard sample [157].

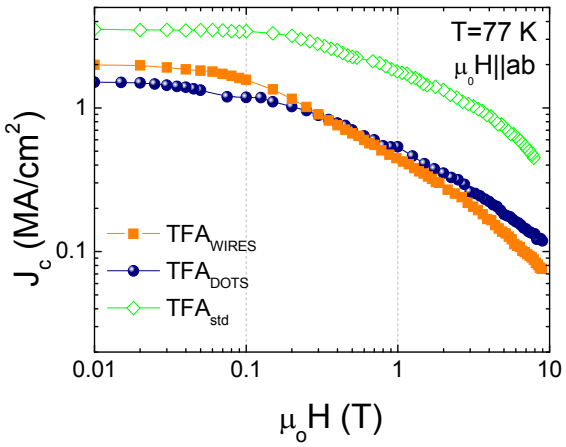

Fig. 7-15: Magnetic field dependence of J_c at 77 K for H||ab of samples TFA_{WIRES} (■),TFA_{DOTS} (●) and TFA_{std} (◊).

Fig. 7-16 displays the dependence of the critical current density with the magnetic field applied H||c and H||ab at 50 K and 35 K for samples TFA_{DOTS} and TFA_{std}. J_c at self-field is lower for the nanostructured sample at all temperatures in agreement with previous results. For H||c (close symbols), the total critical current density of TFA_{DOTS} at 50 K is never greater than J_c of TFA_{std} (Fig. 7-16a). However, its in-field dependence is still better as it is observed in the magnetic field dependence of J_c normalized to the corresponding self-field values (Fig. 7-16b). Similar J_c(H||c) behaviour is observed at 35 K (Fig. 7-16c and d, respectively). For H||ab (open symbols), we observe that the in-field performance of J_c of TFA_{DOTS} approaches that of TFA_{std} as the temperature is decreased, despite still exists a reduction of critical current density at self-field. At 35 K (Fig. 7-16c and d), the in-field dependence for H||ab of both samples is fairly similar till $\mu_0 H \sim 1$ T, suggesting that the pinning mechanisms controlling the critical current density for H||ab at low temperatures are fairly similar for both TFA_{DOTS} and TFA_{std} samples.

Summarizing, the pinning centres introduced by interfacial CGO nanostructures result into an improvement of the critical current density J_c for H||c at expenses of a decrease of J_c for H||ab at 77 K. Reduction of J_c at self-field for the nanostructured samples with respect to the standard ones is observed in all temperature range. For H||c, the efficiency of pinning sites promoted by interfacial nanoislands is higher at high magnetic fields and high temperatures, resulting into a better irreversibility line than in the standard sample. However, the presence of interfacial nanostructures modify somehow the vortex pinning mechanism for H||ab, resulting into stronger decrease of J_c in-field dependence specially at high temperatures and high magnetic fields for H||ab. Consequently, detailed analyses of the angular dependence of critical current density at different temperatures and magnetic fields are required to determine more accurately the type and behaviour of induced defects.

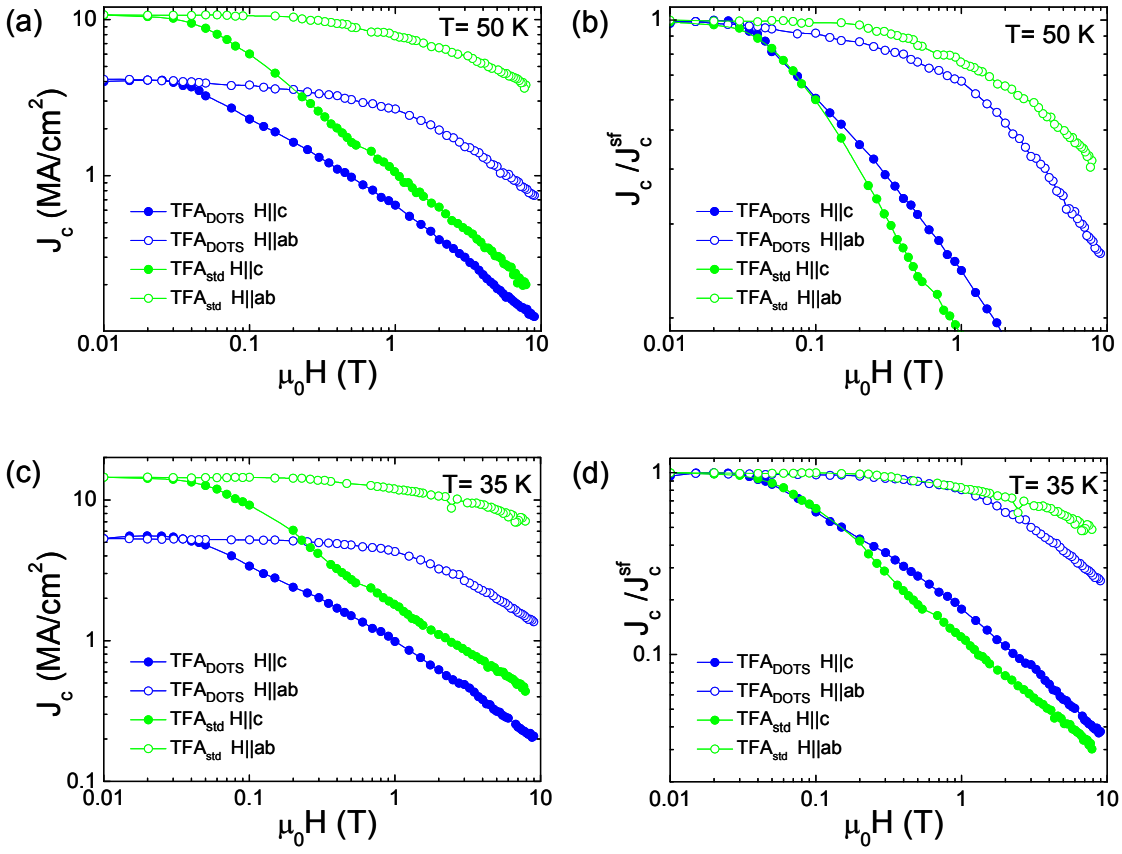

Fig. 7-16: $J_c(H)$ at 50 K (a) and 35 K (c) and of $J_c(H)$-normalized to the corresponding self-field values also at 50 K (b) and 35 K (d) for samples TFA_{DOTS} (blue symbols ●○) and TFA_{std} (green symbols●○). Close symbols correspond to magnetic fields applied H||c, whereas open ones correspond to H||ab.

7.3.3 Angular dependence of transport $J_c(\theta,H,T)$ measurements

Effectiveness of vortex pinning sites changes with temperature and magnetic field intensity and orientation. Therefore, angular transport measurements of critical current densities as function of temperature and magnetic field are a valuable source of information about vortex pinning landscape. In the present subsection, a general analysis of $J_c(\theta,H,T)$ curves is performed and, then, a new methodology developed in our group to discern between the distinct sorts of pinning centres is applied, leading to the construction of H-T vortex pinning diagrams for interfacial nanostructured YBCO-TFA thin films [294].

7.3.3.1 $J_c(\theta,H,T)$ dependence

Fig. 7-17 shows the $J_c(\theta,H)$ curves at 77 K for different applied magnetic fields from μ_oH= 0.1 T to 9 T for sample TFA_{DOTS}. Measurements were performed with the set up described in chapter 2, where θ is defined as the angle between the crystallographic c-axis and the applied magnetic field. Critical current density is found to significantly depend on magnetic field orientation because of the anisotropy of the material and the microstructure of the YBCO

thin film. The general trend followed by $J_c(\theta)$ consists of a sharp maximum when the magnetic field is applied parallel to ab-planes ($\theta=90^o$) and then J_c monotonically decreases till it approaches H||c ($\theta=180^o$), where a small broader peak appears. This second peak becomes more prominent as the magnetic field increases. Part of the angular dependence of J_c is strongly dependent on the electronic mass anisotropy of the material [122, 302]. The first sharp peak for H||ab is also consequence of the anisotropic contribution of pinning sites aligned parallel to ab-planes. Due to the layered structure of the material, Cu-O planes are a source of intrinsic pinning in this direction; but there are as well extrinsic linear or planar defects aligned parallel to ab-planes such as intergrowths or stacking faults which are also contributing to the enhancement of J_c(H||ab) [303-305]. The second peak observed for H||c arises from the anisotropic defect contribution of those pinning sites lying parallel to c-axis, like threading dislocation, twin boundaries, etc. [306-308].

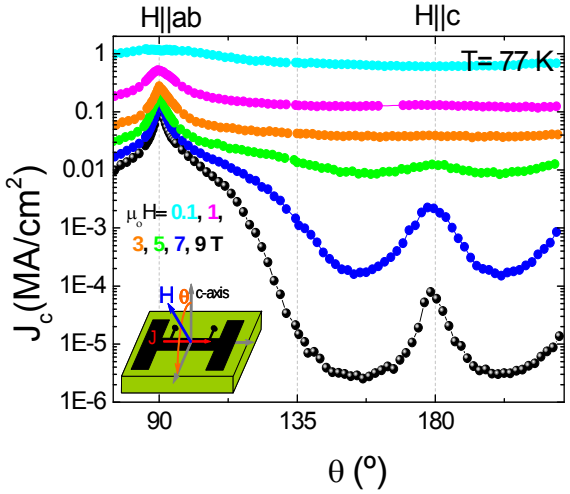

Fig. 7-17: Angular dependence of critical current density $J_c(\theta)$ at 77 K for magnetic fields $\mu_o H$= 0.1, 1, 3, 5, 7 and 9 T of the sample TFA_{DOTS}. The inset shows the measurement configuration.

It must be noticed that the shape of $J_c(\theta,H,T)$ curves is not the same for all the films. It is strongly influenced by the growth technique and particular growth conditions used. $J_c(\theta,H,T)$ curves depend on the microstructure of the film, thus they provide information of variations and modifications of vortex pinning centres as consequence of nanoengineering of thin films. In Fig. 7-18, $J_c(\theta)$-dependence at 77 K and $\mu_o H$=3 and 7 T of sample TFA_{DOTS} (close symbols) is compared with that of standard thin film TFA_{std} (open symbols). At 77 K, the critical current density for fields applied parallel to c-axis is higher for the nanostructured sample than for the standard one, either at 1 T and 5 T, as was previously shown in Fig. 7-12. Nevertheless, for fields applied parallel to ab planes, the critical current density of the standard sample is always higher. In intermediate θ regions, J_c of TFA_{DOTS} is higher in a broaden range away of $\theta=180^o$; this performance extends further at 3 T than at 7 T. The much prominent peak observed at H||c for TFA_{DOTS} suggests the increase of anisotropic pinning parallel to c-axis owing to interfacial

CGO nanostructures. The decrease of J_c for H||ab indicates a reduction of the effectivness of pinning parallel to ab-planes.

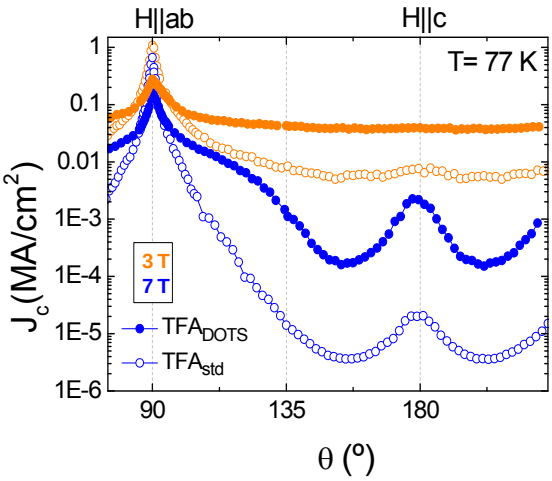

Fig. 7-18: $J_c(\theta)$ at 77 K of samples TFA_{DOTS} (close symbols) and TFA_{std} (open symbols) at $\mu_o H$= 3 T (●) and 7 T (●).

Thus, $J_c(\theta, H)$ curves at 77 K of interfacial nanostructured and standard YBCO-TFA films are different. Therefore, we conclude that the microstructure of both samples is remarkably different. Hence, a detailed analysis of $J_c(\theta, H, T)$ curves is subsequently presented to identify and quantify the kind of pinning mechanisms acting at each region.

7.3.3.2 Electrical transport angular analyses to identify and quantify different vortex pinning contributions: methodology

A new methodology has been developed in our group by Gutiérrez *et al.* [157, 293] to identify and quantify the contribution of distinct pinning centres to flux pinning. As a result, H-T vortex pinning diagrams can be built up. This procedure is essentially based on the angular dependence of $J_c(\theta,T,H)$. The angular dependence of J_c enables the classification of vortex pinning centres into anisotropic and isotropic defects, whereas the temperature dependence of J_c permits to classify them according to their strength into strong and weak pinning centres.

Distinction between isotropic and anisotropic defects is achieved following the isotropic scaling approach proposed by Blatter *et al.* [131], and further developed by Civale *et al.* [308, 309]. Due to the anisotropic layered structure with 3D vortex structure of YBCO, the critical current generated by isotropic defects depends on θ and H only through a unique variable, the so called effective magnetic field

$$H_{eff}(\theta, H) = H\,\varepsilon(\theta, \gamma) \qquad \textbf{Eq. 7-5}$$

where $\varepsilon(\theta, \gamma) = (\cos^2\theta + \gamma^{-2}\sin^2\theta)^{1/2}$ and γ is the mass anisotropy. Typically, γ~5-7 for YBCO. Though, in the present study γ was determined for each film through the collapsing of the irreversibility line at different angles [157].

This scaling is applied to sets of $J_c(\theta)$ data corresponding to different magnetic fields at a given temperature, like those shown in Fig. 7-17. When plotting J_c as function of the effective magnetic field H_{eff} (Fig. 7-19a), those regions where pinning is only generated by isotropic defects collapse, i.e. they present the same $J_c(H_{eff})$ value. Like this, the contribution to the total critical current density due to isotropic pinning sites is determined. Mass anisotropy factor γ=(7±0.5) determined from irreversibility line measurements was used resulting into a good scaling of $J_c(\theta)$ curves as it is evidenced by the solid cyan line in Fig. 7-19a.

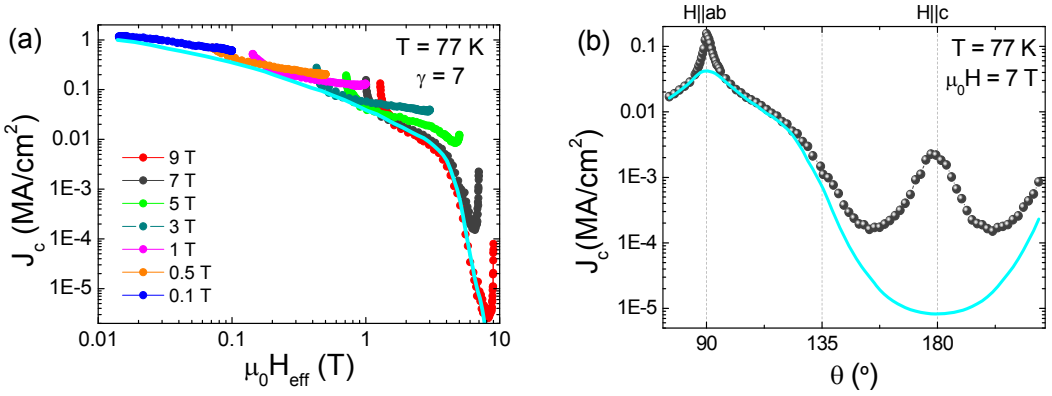

Fig. 7-19: J_c dependence with the effective magnetic field H_{eff} at 77 K (a) and $J_c(\theta)$ at 77 K and μ_oH= 7T (b) for sample TFA_{DOTS}. The solid cyan lines represents the corresponding $J_c^{iso}(H_{eff})$ and $J_c^{iso}(\theta)$ dependence in (a) and (b), respectively.

By deconvoluting $J_c^{iso}(H_{eff})$ for a chosen magnetic field, the contribution to J_c produced by isotropic pinning centres is obtained, $J_c^{iso}(\theta,H,T)$. For example, cyan curve in Fig. 7-19b shows $J_c^{iso}(\theta)$ at 77 K and μ_oH=7 T of nanostructured sample TFA_{DOTS}. Finally, to obtain the anisotropic pinning defect contribution, the isotropic $J_c^{iso}(\theta, H, T)$ curve must be subtracted from the experimental curve, since $J_c(\theta) = J_c^{iso}(\theta) + J_c^{an}(\theta)$. The separation between these two contributions results to be an essential tool to study the isotropic and anisotropic pinning sites in YBCO films, and to compare interfacial nanostructured samples and standard YBCO-TFA films.

Repeating this procedure for distinct temperatures, one obtains separately the dependence of the isotropic and the anisotropic pinning defect contributions as function of the temperature for any magnetic field orientation. The resulting $J_c^{iso}(T)$ and $J_c^{an}(T)$ for a given orientation (H||c in our case) can then be fitted with Eq. 7-3 (weak defects), Eq. 7-4 (strong defects) or with a combination of both. As a result, vortex pinning sites are sorted in a

quantified manner into isotropic and anisotropic, and each of these contributions is separated into weak and strong defects. The quantification of distinct vortex pinning contributions enables the generation of a very complete vortex pinning diagram which reflects the (H,T) landscape for the distinct contributions to the total critical current density of YBCO films.

7.3.3.3 Isotropic-anisotropic and weak-strong defect pinning contributions to J_c

Fig. 7-20 presents the experimental curves $J_c(\theta)$ at 77 K and $\mu_o H$=1 T (a) and 5 T (b) for sample TFA_{DOTS} together with the corresponding contributions to critical current density of isotropic and anisotropic pinning defects. $J_c^{iso}(\theta)$ and $J_c^{an}(\theta)$ were obtained following the previously described methodology based on Blatter scaling approach. We observe that the isotropic defect pinning contribution is a very important source of the modulation of the total critical current with θ. As it has already been pointed out, $J_c^{iso}(\theta)$ also represents an important contribution to the peak observed at H||ab. On the other hand, the anisotropic defect contribution dominates the total critical current in an extended angular region around the c-axis. Particularly, the $J_c(\theta)$ peak arising at H||c is totally due to the contribution of anisotropic pinning centres. From these figures, it is straightforward appreciated that the separation of these two contributions is a powerful tool to understand the behaviour of the pinning defects present in YBCO thin films and, particularly, to the interfacial nanostructured YBCO films.

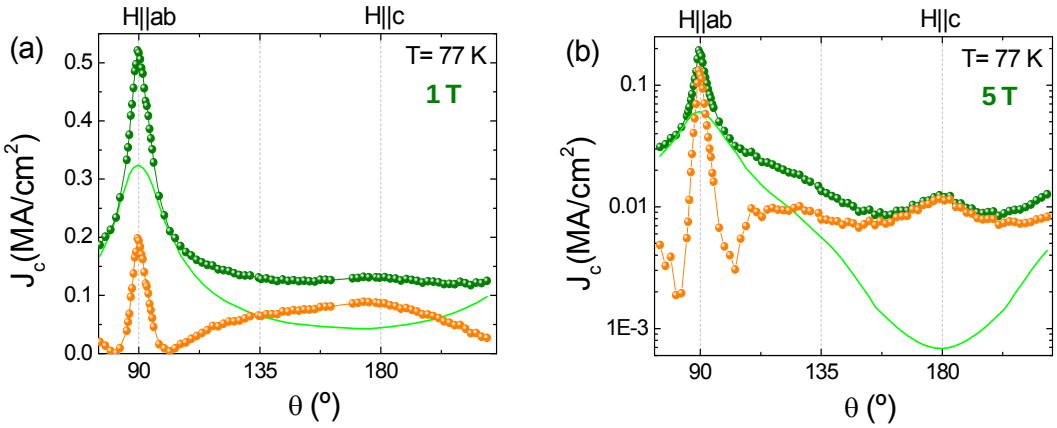

Fig. 7-20: Angular dependence of the critical current density $J_c(\theta)$ (●) and isotropic $J_c^{iso}(\theta)$ (—) and anisotropic $J_c^{an}(\theta)$ (●) pinning contributions to J_c at 77 K and $\mu_o H$=1T (a) and 5 T (b) of TFA_{DOTS}.

From a set of plots like those in Fig. 7-20, we can determine the magnetic field dependence of the isotropic and anisotropic pinning contributions at a given temperature. Since the presence of interfacial oxide nanoislands results into an improvement of the pinning efficiency when the applied magnetic field is aligned parallel to the c-axis of the sample, we will mainly focus on this magnetic field orientation (H||c). In Fig. 7-21 we represent the dependence with H||c of the total critical current and corresponding isotropic and anisotropic

pinning contributions at 77 K for the sample TFA_{DOTS}. It is observed that both pinning contributions, $J_c^{iso}(H)$ and $J_c^{an}(H)$, behave distinctively as function of the applied magnetic field. We also distinguish that the J_c at self-field is controlled by the contribution of isotropic defects. Accordingly, J_c^{iso} is the contribution that has to be improved in order to avoid the decrease in $J_c(sf)$ in interfacial nanostructured films with respect to standard ones. As the magnetic field increases, the anisotropic defect contribution becomes more relevant. For $\mu_oH>0.8$ T, the contribution of anisotropic defects to the total critical current is higher than that of isotropic defects. At $\mu_oH>2$ T, the behaviour of the critical current density is completely governed by J_c^{an}. In next section we will see that in fact both isotropic and anisotropic contribution at 77 K are solely due to isotropic-strong and anisotropic-strong defects, respectively.

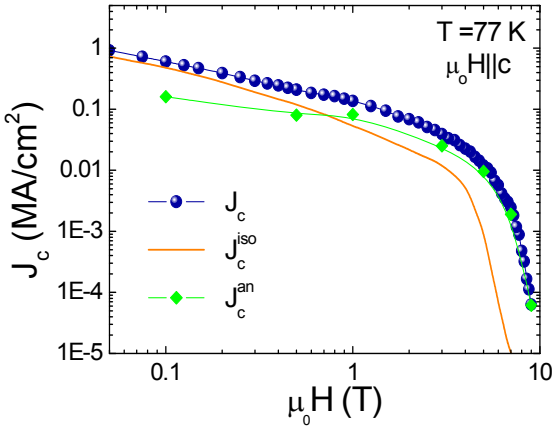

Fig. 7-21: Magnetic field dependence for H||c of J_c (●), J_c^{iso} (—) and J_c^{an} (♦) at 77 K for TFA_{DOTS}.

From previous analyses we know that the improvement of J_c in interfacial nanostructured YBCO films is achieved at high temperatures and high magnetic fields. Therefore, we can now attribute this behaviour to an enhancement of the anisotropic pinning contribution in nanostructured films with respect to standard YBCO-TFA samples. In Fig. 7-22a, it is shown the contribution of anisotropic pinning sites to J_c at 77 K as function of the magnetic field H||c for samples TFA_{DOTS} and TFA_{std}. At low magnetic fields, the anisotropic pinning contribution of both samples is fairly similar. However, J_c^{an} of the nanostructured sample (close diamonds) shows smoother in-field dependence and high values than the standard film (open diamonds). Hence, better in-field dependence at high temperatures and high magnetic fields and consequent improvement of the irreversibility line of TFA_{DOTS} is due to an increase of the anisotropic pinning defect contribution to J_c with respect to TFA_{std}. For example, at 77 K and $\mu_0H||c=4$ T, $J_c^{an}=0.014$ MA/cm^2 for TFA_{DOTS}, which represents an enhancement of 386% with respect to the control sample TFA_{std}.

In Fig. 7-22b, it is compared the anisotropic pinning contribution to J_c for H||ab at 77K for both samples TFA_{DOTS} and TFA_{std}. For H||ab, we observe that J_c^{an} of interfacial nanostructured film is lower than that of the standard sample in all magnetic field range. Thus,

the reduction of the critical current density in nanostructured YBCO-TFA films for H||ab is consequence of a decrease of the anisotropic pinning contribution in these samples fot H||ab. So, we have proved that interfacial nanoislands generate a type of defects that act effectively as anisotropic pinning sites at high temperature and magnetic fields H||c, but depress the anisotropic pinning capabilities for H||ab.

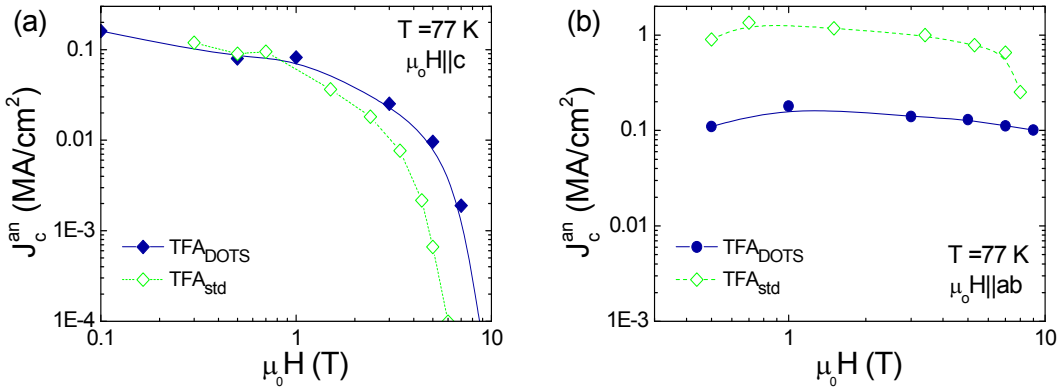

Fig. 7-22: Comparison of J_c^{an} (H||c) (a) and J_c^{an} (H||ab) (b) at 77 K of samples TFA_{DOTS} (♦) and TFA_{std} (◊).

Fig. 7-23 shows that the isotropic and anisotropic pinning contributions to J_c observed for sample with interfacial (001)-nanodots (TFA_{DOTS}) also applies to nanostructured films with interfacial (011)-nanowires (TFA_{WIRES}). In both cases, $J_c(H)$ is governed by the isotropic defect contribution at self-field, whereas the improvement at high magnetic fields is due to the anisotropic pinning contribution to total J_c. Hence, the vortex pinning effect promoted by the presence of interfacial nanostructures is independently of their particular morphology at least in this approximation.

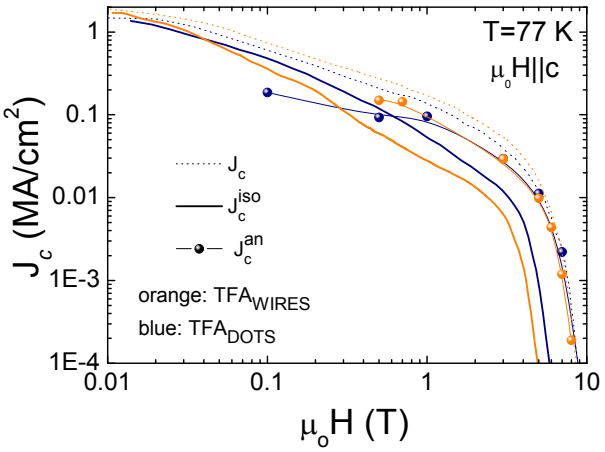

Fig. 7-23: Comparison of the magnetic field dependence for H||c and at 77 K of J_c (···), J_c^{iso} (—) and J_c^{an} (●) for samples TFA_{WIRES} (orange symbols) and TFA_{DOTS} (blue symbols).

Moreover, doing this separation of J_c-contributions for different T, we can investigate the temperature dependence of the isotropic and anisotropic pinning contributions to J_c and discern between the strength of vortex pinning sites involved in each of these contributions. Fig. 7-24 displays a typical example of the dependence with temperature of J_c^{iso} and J_c^{an} contributions at $\mu_o H||c=3$ T for the sample TFA_{DOTS}. The anisotropic defect contribution has a smoother dependence with temperature than the isotropic contribution; this behaviour occurs for all magnetic fields. At low temperatures, the isotropic defect contribution has much higher values than the anisotropic contribution. However, J_c^{an} becomes more important to J_c than J_c^{iso} as temperature is increased. At $\mu_o H||c=3$ T, the anisotropic pinning contribution becomes dominant at T>50 K. It has been observed that the crossover between the distinct regions of dominance occurs at lower temperature as higher is the magnetic field. That is, anisotropic pinning contribution is more relevant at high magnetic fields and high temperatures.

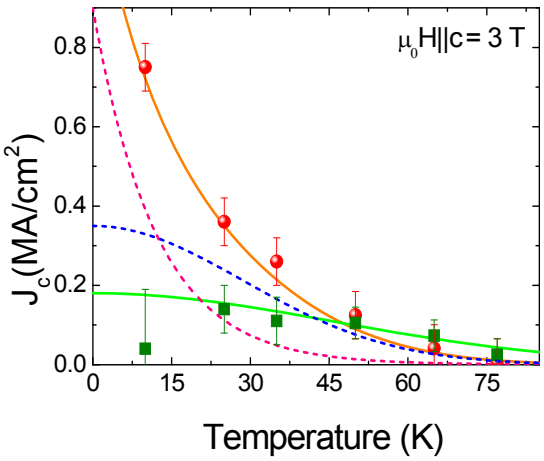

Fig. 7-24: Temperature dependence of the isotropic (●) and anisotropic (■) pinning contributions for sample TFA_{DOTS} at $\mu_o H||c=3$ T. Green line is a fit to Eq. 7-4 ($J_c^{an\text{-}st}$) and orange line a fit to Eq. 7-6; the pink dashed line indicates the $J_c^{iso\text{-}wk}(T)$ contribution and the blue dashed line indicates the $J_c^{iso\text{-}st}(T)$ contribution.

From the temperature dependence of J_c^{iso} and J_c^{an} we can evaluate the strength of defects involved in each contribution. As described by Eq. 7-3 and Eq. 7-4, defects can be classified into weak and strong pinning centres, respectively. Experimental $J_c^{an}(T)$ data can be pretty good fitted to Eq. 7-4, i.e. $J_c(T)= J_c^{st} \exp[-3(T/T^+)^2]$ (green line in Fig. 7-24). So, all anisotropic pinning centres correspond to strong pinning sites, $J_c^{an\text{-}st}$. The isotropic defect contribution cannot be solely described by weak pinning model (Eq. 7-3), as could be a priori expected from its fast dependence with temperature. Experimental $J_c^{iso}(T)$ data can be fitted considering the isotropic pinning contribution as composed by isotropic-weak pinning centres and also isotropic-strong pinning centres. Accordingly, orange line in Fig. 7-24 is a fit to

$$J_c^{iso}(T) = J_c^{iso-wk}(T) + J_c^{iso-st}(T) = J_{c0}^{iso-wk}\, e^{-T/T_0} + J_{c0}^{iso-st}\, e^{-3\left(T/T^+\right)^2} \qquad \textbf{Eq. 7-6}$$

where T^+ is related to the pinning energy of strong isotropic defects. At lower temperatures, the contribution of the isotropic-weak pinning centres (pink dashed line) is the relevant one. At higher temperatures, the isotropic defect contribution is totally governed by the contribution of isotropic strong pinning sites (blue dashed line). So, at 77 K (example displayed in Fig. 7-21a) all isotropic contributions are effectivelly due to isotropic-strong defects.

The relative weight of the distinct pinning contributions (isotropic-weak, isotropic-strong, anisotropic-strong) to the total critical current can be readily appreciated in H-T vortex pinning diagrams. In Fig. 7-25 we show the relative weight of $J_c^{iso\text{-}wk}$ to the total critical current density as function of temperature and applied magnetic field H||c for samples TFA_{DOTS} (a) and TFA_{std} (b). We observe that the isotropic-weak contribution is more relevant in the interfacial nanostructured YBCO thin film than in the standard sample. Even though, above 30 K the contribution $J_c^{iso\text{-}wk}$ is nearly irrelevant in both samples.

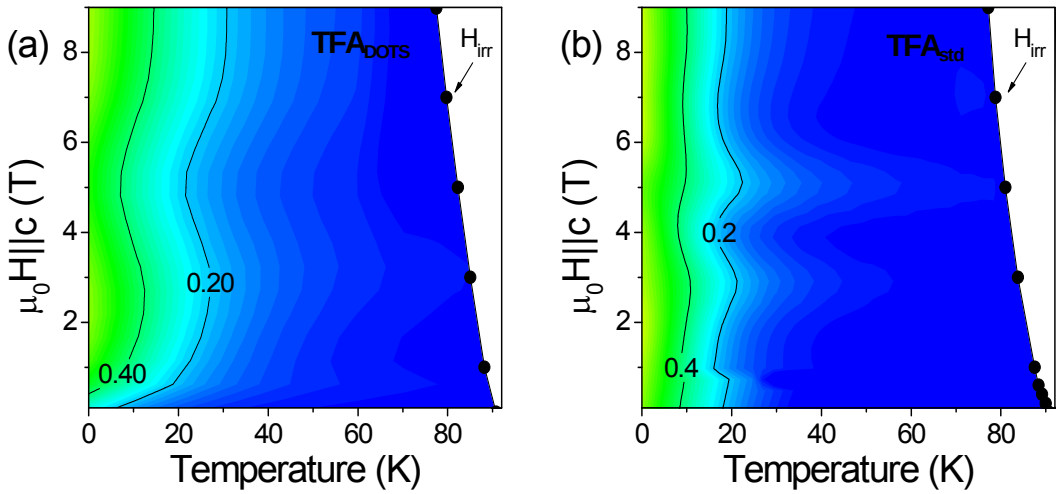

Fig. 7-25: Magnetic field – temperature map of the isotropic-weak pinning contribution $J_c^{iso\text{-}wk}$ in front of the total critical density $J_c=J_c^{iso}+J_c^{an}$, i.e. $J_c^{iso\text{-}wk}/J_c$, of samples TFA_{DOTS} (a) and TFA_{std} (b).

In Fig. 7-26, it is compared the ratio $J_c^{iso\text{-}st}/J_c$ for the interfacial nanostructured sample TFA_{DOTS} (a) and standard film TFA_{std} (b). It is observed that the isotropic-strong pinning contribution of TFA_{DOTS} is strongly diminished with respect to $J_c^{iso\text{-}st}$ contribution in TFA_{std}. At intermediate temperatures and intermediate magnetic fields ($\mu_oH<4T$), $J_c^{iso\text{-}st}$ accounts for more than 60% of total critical current density of TFA_{std}. In contrast, the isotropic-strong contribution of TFA_{DOTS} just reaches values of 60% below $\mu_oH<1T$. Let's point out that the region of dominance of $J_c^{iso\text{-}st}$ is typically at intermediate temperatures and intermediate magnetic fields. On the other hand, let's recall that inductive SQUID measurements mainly measure the contribution of strong pinning sites to J_c. Therefore, depression of isotropic-strong pinning contribution in interfacial nanostructured YBCO thin films is the responsible of the poorer in-

field performance observed in these type of samples with respect to standard ones in $J_c(H)$ values derived from inductive SQUID measurements.

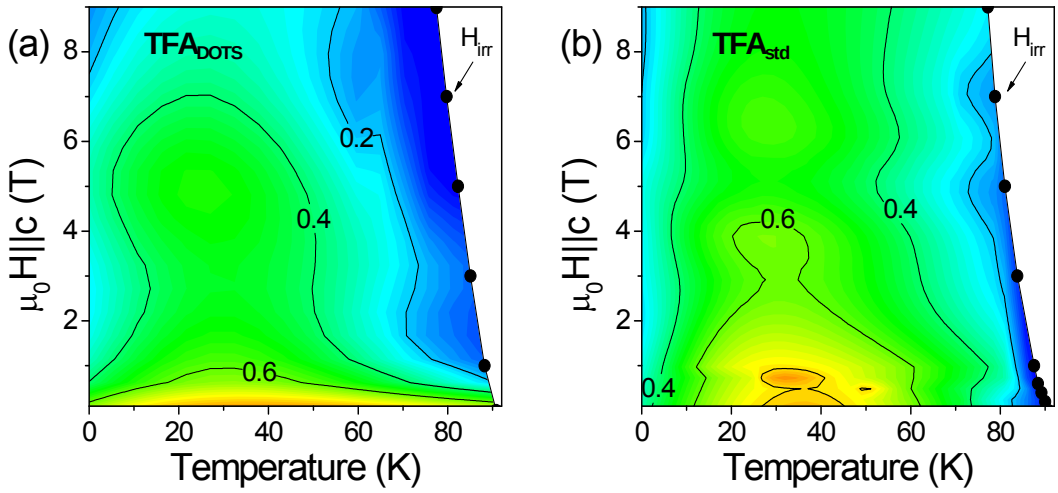

Fig. 7-26: H-T vortex pinning diagram for J_c^{iso-st}/J_c of samples TFA_{DOTS} (a) and TFA_{std} (b).

Finally, in Fig. 7-27 it is compared the relative weight of the anisotropic-strong pinning contribution with respect to the total J_c for samples TFA_{DOTS} (a) and TFA_{std} (b). The anisotropic defect contribution is responsible for the vortex pinning at high temperatures and high magnetic fields. At 60 K, J_c^{an} accounts for ~60% of the total critical current of TFA_{DOTS}; at 75 K and higher magnetic fields it represents more than ~80% of J_c. If we compare these results with the standard sample TFA_{std} (Fig. 7-27b), we observe that the anisotropic-strong defect contribution controls in more than an 80% the total J_c in a reduced region very close to the irreversibility line. Thus, from this H-T map it is readily appreciated that the presence of interfacial oxide nanoislands leads to an enhancement of the anisotropic-strong defect contribution at high temperatures and high magnetic fields H||c.

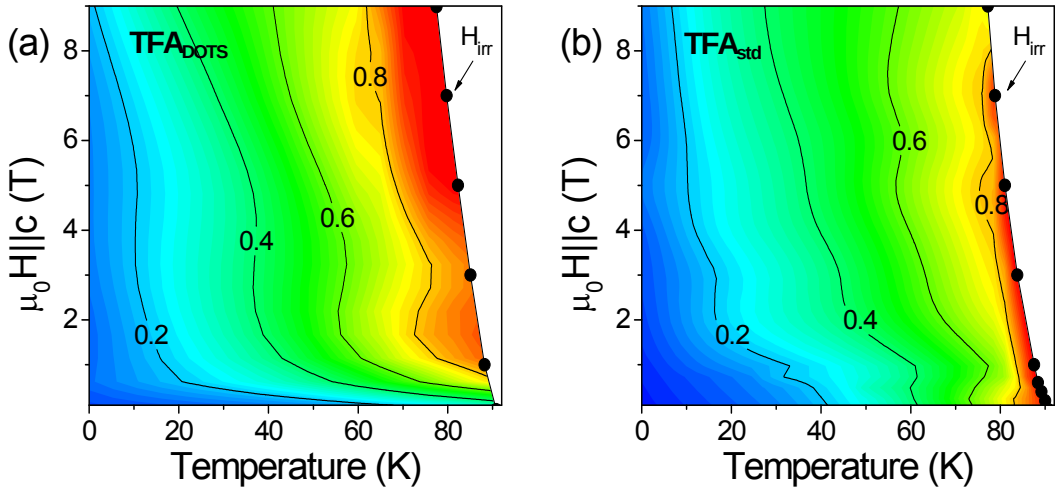

Fig. 7-27: H-T vortex pinning diagram for J_c^{an-st}/J_c of samples TFA_{DOTS} (a) and TFA_{std} (b).

Summarizing, isotropic-weak defects control vortex pinning at lower temperatures, whereas at intermediate temperatures dominate isotropic-strong defects. At higher temperatures and high magnetic fields, the vortex pinning is governed by anisotropic-strong pinning sites. Since the presence of interfacial nanostructures leads to an improvement of the anisotropic pinning contribution, nanostructured YBCO thin films show a better performance as we approach high temperatures close to the irreversibility line. On the other hand, the reduction of J_c at self-field in nanostructured films is due to a decrease in the efficiency or density of isotropic-strong pinning defects. Hence, these results indicate that the presence of interfacial nanostructures leads to an increase of extended defects parallel to H||c, as could be the case of threading dislocations or 2D planar defects parallel to c-axis, such as twin boundaries, antiphase boundaries, ab-planes, etc. However, the presence of these defects efficient for H||c disrupts the pinning capabilities for H||ab of interfacial nanostructured YBCO-TFA thin films. The cause of this deterioration of vortex pinning for H||ab could be associated to the fact that defects efficient for H||c block the proliferation of extended defects along CuO_2 planes of YBCO or break the continuity of ab planes. As mentioned above, the existence of ab-planes result into another mechanism of vortex pinning. They constitute a sort of extended defect efficient for H||c which breaks the coherence along ab; moreover, 90^o grain boundaries are known to not dramatically decrease the critical temperature of the film [310]. In any case, TEM analyses are essential to validate all these hypotheses and determine the source of improved anisotropic pinning contribution.

7.4 Vortex pinning as function of thickness in interfacial nanostructured YBCO-TFA thin films

Interfacial CGO nanoislands have a medium height of ~8 nm, which represents just 3% of the overall thickness of the YBCO-TFA thin films (~275 nm) grown on top. Therefore, once the distinct types of pinning sites present in these interfacial nanostructured YBCO-TFA films have been identified, it appears necessary to study their performance as function of film thickness in order to complete the knowledge on vortex pinning defects generated by oxide nanostructures at the interface.

Because of the chemical nature of TFA-route, very thin films might show a microstructure distinct to that of thicker ones. Growth of thinner films requires the use of diluted solutions; therefore, the amount of precursor to be pyrolyzed changes. The gas-solid process of growth based on the elimination of HF is also modified, since deposited layer is thinner. Moreover, the reactivity of interfacial oxide nanoislands with YBCO precursor solution and growth process may also change when precursor concentration is diluted. Consequently, the resulting landscape of pinning centres might vary between CSD-derived samples of different

thicknesses. All these problems do not arise when YBCO films are grown by physical routes, where the initial growth stages are common for both thin and thicker films. Deposition of the same amount of precursor solution and just carry out partial growth of the resulting YBCO film is a complicated strategy. Therefore, a particular experiment was designed to solve these problems and to also avoid possible uncertainties arising from dealing with different samples. A ~250 nm thick YBCO-TFA thin film was grown on a template with interfacial CGO nanowires, like all examples analysed in previous sections. The film was subsequently patterned with optical lithography with a mask (Fig. 7-28a) with four equal tracks of (20 x 100) μm^2 with their corresponding pads to apply current and measure voltage. Fig. 7-28b shows one of these tracks of ~250 nm thickness. As a result, we had four equivalent YBCO tracks within the same sample to separately diminish to the desired thicknesses and study the critical current dependence with thickness of nanostructured YBCO films. Milling of each single track was carried out by Focused Ion Beam (FIB). A (20 x 40) μm^2 region in the centre of the track was milled in each case, which covered the whole width of the track but not its entire length as shown in Fig. 7-28c. Milling of the complete track was not required, because the thinnest region will be the first to undergo from the superconductor to the normal state and, hence, the one measured. Fig. 7-28c shows a track milled with FIB down to 170 nm. Milling conditions used are summarized in chapter 2.

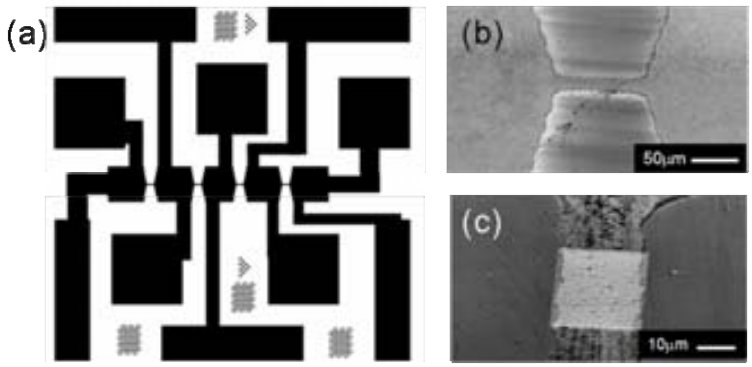

Fig. 7-28: Mask used to defined 4 equivalent tracks of (20 x 100) μm^2 on a nanostructured YBCO film (a). SEM images of a track before (b) and after (c) FIB milling down to 170 nm.

Applying this process to distinct tracks we were able to study the $J_c(\theta)$ dependence at 250 nm, 170 nm and 130 nm; all measurements were done in the same interfacial nanostructured YBCO-TFA thin film. No lower thickness could be measured, since after longer milling times the track suffered a degradation of critical temperature perhaps associate to a high implantation of Ga ions which damaged the YBCO matrix. Fig. 7-29a shows the resistivity ρ dependence with temperature normalized to resistivity at normal state ρ(300K) of tracks TFA_{250}, TFA_{170} and TFA_{130} corresponding to YBCO-TFA film thickness of 250 nm, 170 nm and 130 nm, respectively. No reduction of T_c was experienced by these milled down tracks and a critical temperature of T_c~90.5 K was obtained in all cases. The critical current density at self-

filed was also kept constant after milling as shown in Fig. 7-29b, J_c(sf) ~1.9 MA/cm^2; smaller variations are expected within tracks of the same sample. The no reduction of critical temperature neither of J_c proves that FIB milling approach does not modify the superconductivity of these films and that Ga implantation was avoided.

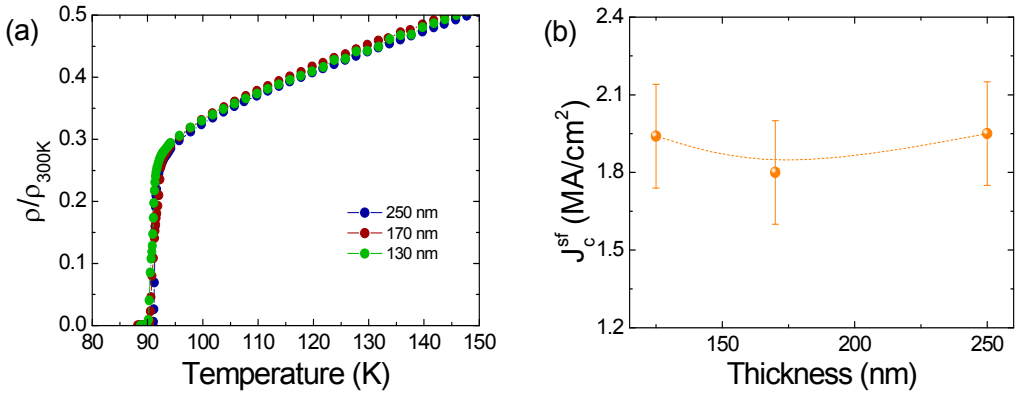

Fig. 7-29: Resistivity normalized to ρ_{300K} as function of temperature of tracks TFA_{250} (●), TFA_{170} (●) and TFA_{130} (●) (a); and their corresponding critical current density at self-field (b).

Fig. 7-30a presents the $J_c(\theta)$ dependence of tracks TFA_{250}, TFA_{170} and TFA_{130} at 77 K, 65 K and 50 K and μ_oH=5 T. As a general trend, all interfacial nanostructured YBCO-TFA films of different thickness follow the angular dependence of J_c typically observed in YBCO-TFA films. A sharp peak appears for magnetic fields applied parallel to ab planes, and then $J_c(\theta)$ monotonically decreases as we separate from θ=90^o; a second smaller and broader peak arises at 77 K for H||c. In previous section, we have noticed the prominence of this peak in nanostructured films in comparison to standard samples because of the enhancement of anisotropic-strong pinning contribution at high temperatures and high fields. Critical current density $J_c(\theta)$ is enhanced as thickness is reduced in almost all θ range; just a reduction of J_c is observed when magnetic field is applied H||ab due to a reduction of anisotropic centres in that orientation as will be seen following. Fig. 7-30b shows a zoomed view of $J_c(\theta)$ for θ close to 90^o.

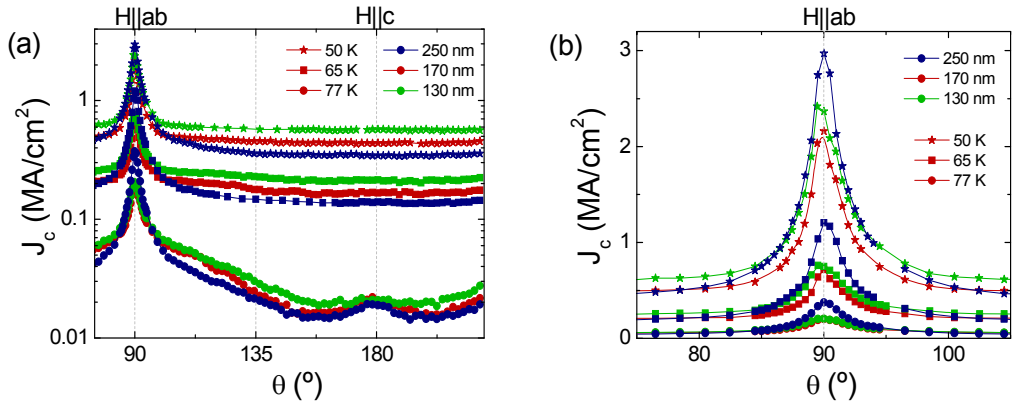

Fig. 7-30: $J_c(\theta)$ dependence at μ_oH=5 T and 77 K (●), 65 K (■) and 50 K (★) of TFA_{250} (●), TFA_{170} (●) and TFA_{130} (●) (a); zoomed view of $J_c(\theta)$ close to θ=90^o (b).

Following the methodology introduced in 7.3.3.2, the distinct vortex pinning contributions to the total critical current are separated. Fig. 7-31a displays the isotropic defect contribution to the critical current at 50 K and $\mu_o H$=5 T as an orange solid line. Subtracting $J_c^{iso}(\theta)$ to the experimental curves, an enhancement of c-axis pinning contribution is observed as thickness is reduced (Fig. 7-31b), indicating that the efficiency of anisotropic defects is reduced as we separate from the interface. So, anisotropic pinning sites induced by interfacial nanoislands act more efficiently close to the islands themselves. The improvement of J_c^{an} for $\mu_o H||c$= 5 T as function of thickness at distinct temperatures is plotted in Fig. 7-31d. In general, for H||c, the anisotropic contribution to the total current density of TFA_{130} is almost twice the contribution of TFA_{250} at the same temperature.

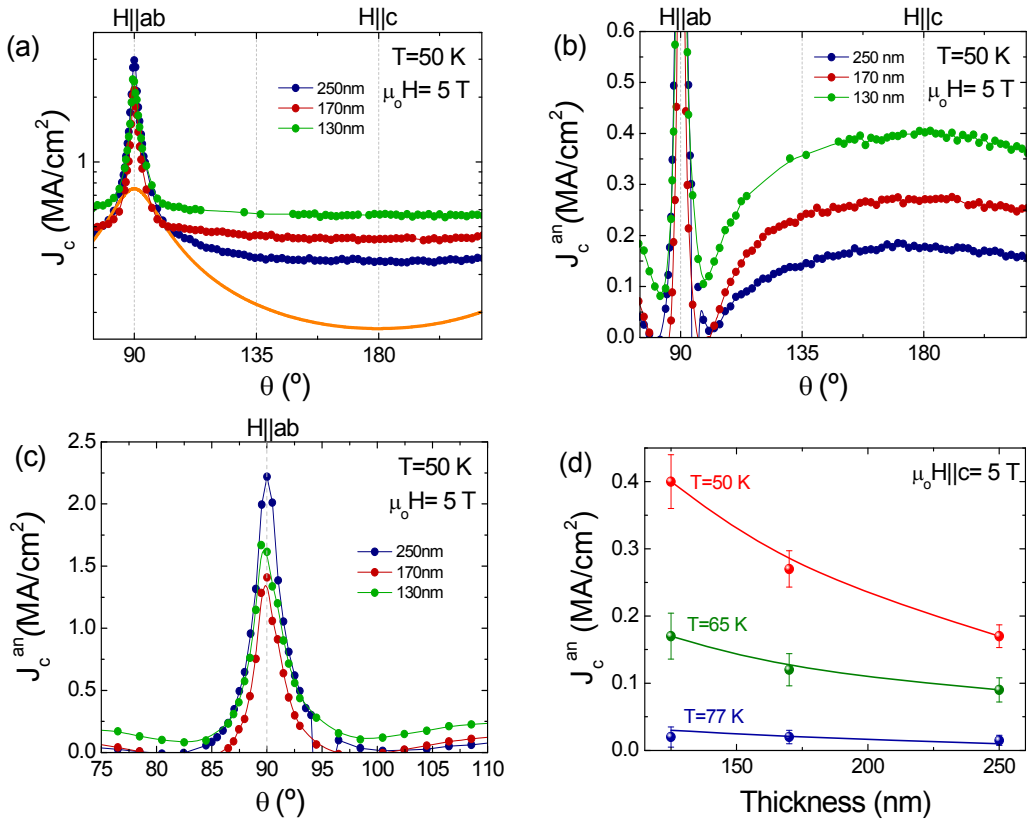

Fig. 7-31: Angular dependence of critical current density at 50 K and $\mu_o H$=5 T of TFA_{250} (●), TFA_{170} (●) and TFA_{130} (●): $J_c(\theta)$ and $J_c^{iso}(\theta)$ (—) dependence (a); anisotropic $J_c^{an}(\theta)$ contribution (b) and anisotropic $J_c^{an}(\theta)$ contribution close to $\mu_o H||ab$ (c). $J_c^{an}(\theta)$ dependence with film thickness for $\mu_o H||c$=5 T and at 77 K (●), 65 K (●) and 50 K (●) (d).

However, despite the improvement of $J_c^{an}(H||c)$, there exists a reduction of $J_c^{an}(H||ab)$, as thickness is reduced, as shown in Fig. 7-31c. Hence, whereas the efficiency of anisotropic vortex pinning for H||c increases as thickness is reduced, the anisotropic pinning contribution for H||ab decreases. A detailed TEM analyses would be required to know the pinning sites responsible for this kind of behaviour. Buckling of ab-planes of YBCO thin films close to interfacial nanoislands could explain part of this reduction of $J_c^{an}(\theta)$ at H||ab, since curved Cu-O

would become less efficient planar pinning centres. The distortion of YBCO ab-planes has a major weight on the overall cross-section of the film as thickness is reduced and, consequently, this effect would be more pronounced in thinner films. ab-planes buckling has been observed on nanostructured YBCO-TFA thin films grown on templates with BZO nanoislands at the interface [153]. This phenomenon has also been reported by YBCO-PLD thin films grown on naturally generated $SrTiO_3$ nanoislands at the buffer layer surface [147] and on CSD-derived MgO nanoislands on STO [288].

7.5 Summary and conclusions

In this chapter we have shown a potential application in the field of high temperature superconductors of the oxide nanostructured templates developed in the present thesis work. Nanostructured templates have been used to nanoengineer superconducting YBCO thin films in order to improve the vortex pinning capabilities of these films. Pushed by the aim to use a low-cost scalable to large areas approach, YBCO thin films were also prepared from a chemical route, MOD-TFA. The high critical current densities (J_c(77K,sf)~ 1.5 MA/cm^2) and the normal to superconductor transition at the expected temperature T_c~91 K prove the high quality of the interfacial nanostructured YBCO-TFA films prepared. So, the presence of interfacial nanostructures does not lead to a degradation of the basic superconducting properties. Just a slight reduction in the critical current at self-field is observed in nanostructured YBCO-TFA films when compared to standard samples (J_c(77K,sf)~ 2 MA/cm^2).

The strong influence of thermal activated processes at high temperature such as flux creep has become a handicap to study the vortex pinning capabilities of nanostructured YBCO films by inductive measurements. Therefore, main characterization of the critical current dependence with magnetic field and temperature has been carried out by electric transport measurements up to 9 T.

Interfacial nanostructured YBCO thin films show a high improvement of vortex pinning capabilities with respect to standard YBCO-TFA films for magnetic fields applied parallel to the c-axis of the sample. At μ_0H||c=5 T, J_c is enhanced from 0.01 to 0.06 MA/cm^2 due to pinning defects induced by interfacial nanoislands. This fact leads to a better in-field performance for H||c and to an enhancement of the irreversibility line for H||c which is as high as 9 T at 77 K for a sample with interfacial nanodots. These behaviours are especially appreciated at high temperatures and high magnetic fields. The improvement of vortex pinning is maintained to a certain deviation H away from the crystallographic c-axis. However, for H||ab it is observed a decrease of the vortex pinning efficiency in comparison to standard samples

We have used a novel methodology previously developed in our group to determine the type of pinning centres responsible of the behaviour of critical current density in nanostructured

films. This method is based on $J_c(\theta,H,T)$ measurements to separate and quantify the distinct pinning contributions. As a result, defects are classified into isotropic and anisotropic pinning centres according to their performance with magnetic field orientation, and they can also be divided depending on their strength into weak or strong defects.

The analysis of the magnetic field dependence of the J_c have pointed out that the increase in vortex pinning for H||c in nanostructured films is due to an improvement of the efficiency or/and density of the anisotropic pinning contribution along c-axis. Since anisotropic pinning contribution governs J_c at high temperatures, it explains why the increase in vortex pinning is especially observed in this region. Dependence of $J_c^{an}(T,H)$ has revealed that all anisotropic sites present in nanostructured films are strong pinning centres. The construction of H-T vortex pinning diagrams have shown that above 75 K and for magnetic fields higher than $\mu_0 H$~5 T, the anisotropic defect contribution represents more than ~80% of the total critical current density. For standard samples, this ratio is just achieved in a reduced region close to the irreversibility line. On the other hand, a reduction of the anisotropic pinning contribution for H||ab in nanostructured samples with respect to standard ones has been found to be the cause of the decrease of J_c for this configuration. The exact sort of pinning site induced by interfacial nanoislands is still unknown at present, TEM analysis are being carried out to determine them.

We have shown that the isotropic pinning contribution in nanostructured films is due to isotropic-weak and isotropic-strong pinning sites; the former dominates at low temperatures and the latter at intermediate temperatures and low fields at high temperatures. The decrease of J_c at self-field is related to a reduction of the isotropic-strong pinning contribution in nanostructured samples compared to standard YBCO-TFA films. Hence, this is the vortex pinning contribution that must be improved to avoid the reduction of J_c at self-field in interfacial nanostructured YBCO films.

Finally, it has been studied the pinning capabilities of interfacial nanostructured thin films as function of the YBCO thickness. Milling of YBCO tracks was done by FIB and the preservation of resistivity and critical current density at self-field proved that samples were not damaged during ion milling process. It is observed that the J_c increases as the thickness is reduced in almost all θ range except for magnetic fields applied close to H||ab. Separation of pinning contributions has shown that the increase of the pinning capabilities as the film is thinned is associated to the anisotropic pinning contribution. Therefore, vortex pinning centres promoted by interfacial nanoislands act more effectively as we approach to the nanoislands themselves. At the same time, the deterioration of the pinning efficiency for H||ab also gets worse.

Hence, we can conclude that interfacial nanoislands can be satisfactory used to improve the vortex pinning capabilities for H||c in YBCO-TFA thin films at high temperatures and high

magnetic fields. The J_c enhancement observed for H||c is similar to that obtained in other works based on surface decoration [116, 117, 147], but the new nanostructured YBCO films presented have the added value to be prepared from an all-chemical route. Results reported, however, do not reach those achieved in YBCO nanocomposites [139-142, 144, 289], the up-to-now considered the most promising approach to high performance of YBCO coated conductors. Nonetheless, in this frame, CSD-prepared nanostructured templates arise as a highly interesting complementary tool to enhance anisotropic vortex pinning for H||c in MOD nanocomposites [144], which already exhibit extremely enhance J_c due to an extraordinary increase of the isotropic-strong contribution and which will result into a highly appealing all-chemically low-cost nanostructured coated conductor.

Chapter 8

General conclusions

Throughout this work, we have shown an innovative methodology for the preparation of oxide nanostructured templates based on self-assembling and self-organizing processes. Specifically, we have grown nanoislands of $BaZrO_3$ (BZO), CeO_2, $Ce_{0.9}Gd_{0.1}O_{2-y}$ (CGO) and La_2O_3 with narrow distribution of sizes and a notable tendency to order on $SrTiO_3$ (STO) and $LaAlO_3$ (LAO) single-crystal substrates. It is especially remarkable the innovative character of the strategy developed based on the deposition of ultradiluted metal-organic chemical solutions as a method to prepare the nanostructured templates. One of the main advantages of this methodology is the possibility to use it for the low-cost nanostructuration of large areas. However, its application has been scarce till the moment and, thus, the methodological and conceptual principles must still be established. The present thesis has been conceived as a contribution to this need. In addition to the experimental work done to prove the capabilities and versatilities of the explored methodology, great effort has also been devoted to the comprehension of the thermodynamic and kinetic processes involved in the formation of the oxide strained nanoislands.

Systematic studies based on modifications of growth conditions (temperature, time, atmosphere, etc.) combined with AFM imaging have proved the possibility to tune the morphology, size, density and distribution of the resulting interfacial oxide nanostructures. Precursor solution's concentration is the main mechanism controlling the amount of deposited material; by reducing the concentration of the metal-organic solution we move from 2D film growth to the formation of 3D nanoislands. We have observed that ultradiluted solutions of the order of $\sim 10^{-3}$ M are required to obtain templates with 3D islands in Volmer-Weber configuration, with a clear observation of substrate steps underneath. Temperature is found to be a crucial parameter to enhance the atomic diffusivity in all investigated systems. Higher temperatures facilitate the crystallization of the amorphous layer, the formation of better defined nanostructures, larger nanoislands, etc. In contrast, the influence of the heat treatment atmosphere on mobility depends on each oxide phase. Atomic mobility of BZO is extremely

slow at low oxygen pressure, whereas the same conditions favours ultrafast kinetics in $Ce_{1-x}Gd_xO_{2-y}$. For La_2O_3, the mobility is not affected by oxygen pressure, at least for the growth conditions investigated. Besides the influence of growth conditions, the main features of interfacial nanoislands (shape, distribution, etc.) are strongly determined by the oxide phase deposited and its epitaxial relation with the substrate. This dictates the misfit strain and settles the surface energies of facets and interface and represents another source to tune islands' characteristics.

BZO nanodots grow cube-on-cube on the also perovskite STO substrate with the epitaxial relation (001)BZO[100]||(001)STO[100]. These interfacial nanoislands exhibit narrow size distribution with mean lateral sizes ~ 40 nm, height ~6 nm and density ~60 dots/μm^2; and they are mainly facetted with {100}-planes. BZO nanodots are preferentially located at the upper edge of lattice steps, probably induced by large strain relief achieved close to these convex regions. Their evolution is very limited, what suggests that they might already exhibit their equilibrium shape. BZO grow in the configuration of lowest lattice mismatch and are facetted with lowest surface energy planes; thus, it seems reasonable that they already attain their lowest energy configuration. However, thermodynamic analyses are required to prove it.

La-based nanoislands on LAO substrates exhibit two distinct shapes associated to distinct crystallographic orientations. Large area rectangular islands with extremely flat terrace at the top are identified with the monoclinic LaOOH phase, which might derive from cubic La_2O_3 exposed to air. Higher dome-shaped islands correspond to a mixture of the two hexagonal phases La_2O_3 and $La_2O_2CO_2$. The regions of these islands identified as La_2O_3 show better defined facets, suggesting that $La_2O_2CO_2$ phase is due to carbon precursors still trapped in the oxide matrix. The high vertical-to-lateral aspect ratios of these islands hint vertical growth as an efficient mechanism of strain relief in this highly strained heteroepitaxial system of dissimilar structures.

$Ce_{1-x}Gd_xO_{2-y}$ system has been analyzed in great detail as a model system to investigate the formation and growth of strain-induced oxide nanoislands by CSD. Particularly, we dealt with the phase $Ce_{0.9}Gd_{0.1}O_{2-y}$ (CGO) instead of pure CeO_2 in order to enhance the number of oxygen vacancies and, thus, to increase mobility. Through oxygen pressure tuning, we can induce the formation of two types of CGO nanoislands on LAO substrates. In O_2, isomorphic nanodots with pretty stable size form. In Ar-5%H_2, anisotropic elongated nanoislands (nanowires) are obtained; they exhibit high tendency to join in labyrinthine structures which rapidly reconstruct into a longer nanowire. Experimentally, it is has been found that the main reason of such distinct CGO nanoislands lies on their particular crystallographic orientation.

Hence, the capability to select interface energy through modification of growth conditions provided us with a powerful tool to investigate the mechanisms leading to the formation and evolution of interfacial oxide nanostructures with distinct degree of in-plane anisotropy.

Isomorphic nanodots grow according to (001)CGO[110]||(001)LAO[100], which bears a lattice mismatch of ε~-1% along the two in-plane growth directions. (001)CGO nanoislands are square-based truncated nanopyramids limited by (111) lateral facets and (001) flat planes at top. They exhibit typical lateral sizes of ~ 50 nm, height ~ 7 nm and density of ~ 80 dots/μm^2. In general, (001)CGO nanodots are ordered into rows along the terraces of vicinal substrates resulting into highly ordered templates. We have shown that this self-organization is the result of the strong confining phenomena that substrate steps exert on dots, despite nanodots are ~ 20 times higher than steps. The high interfacial energy between the fluorite CGO and the perovskite substrate LAO has been signalled as a highly efficient mechanism confining (001)-nanodots in the central part of the terraces. To our knowledge, this is the first time that the ordered arrangement of chemically-derived nanostructures along lattice steps has been observed. Hence, we have introduced a low-cost bottom-up methodology based on CSD and self-organizing principles and which takes advantage of interfacial energies and substrate steps arising from miscut to generate oxide nanostructured templates with high degree of order.

CGO-nanowires are elongated nanostructures with long axis that can measure from 100 nm to 2000 nm long, whereas the short one remains fairly constant with width typically ≤ 50 nm. Moreover, elongation is severely promoted in front of vertical growth and nanowires' height rarely exceeds ~10 nm. Nanowires grow according to the epitaxial relation (011)CGO[0-11]||(001)LAO[010], which results into two distinct in-plane growth directions. Nanowires elongate along CGO[0-11]||LAO[010], which bears a compressive mismatch of just ε~-1%. Their short axis is aligned with CGO[100]||LAO[100]. The misfit along this direction determined through the comparison of lattice parameters would be ε~-30%, which seems physically unreasonable. However, the epitaxial growth can be instead explained though domain matching epitaxy model: 2 fluorite CGO cells fit 3 perovskite LAO cells, leaving a residual misfit strain of ε~+5% and the formation of a misfit dislocation in each domain. These results have been successfully proved through TEM analyses and show the possibility to explain the epitaxial growth of highly incoherent structures. Hence, (011)-nanowires grow under a biaxial anisotropic strain aligning their main axis with the substrate soft directions [100] and [010]. Due to the two-fold symmetry of the (011) orientation, self-organized templates with two families of nanowires orthogonally in-plane oriented are formed. The surface energies of lateral facets are as well anisotropic; nanowires elongate enlarging lateral facets of lowest surface energy (111) and keeping higher energy planes (100) smaller.

Simulation analyses based on thermodynamic models considering constant island's height have demonstrated that distinct strain and surface energies of the two sorts of interfacial CGO nanoislands can explain their different shapes and behaviour.

The isomorphic shape of (001)CGO nanodots on LAO corresponds to the equilibrium shape of these islands for the typical observed sizes, D< 50 nm. For these islands' dimensions, there exists an optimum island size, which proves the thermodynamic stability of (001)CGO dots. Both surface energy and elastic relaxation energy drives small (001)-islands to adopt an isomorphic shape of stable size. However, for large islands, strain energy drives the island to elongate in either of the two in-plane directions. In general, (001)CGO nanodots show very limited coarsening, probably associated to the stability of these islands. However, we have found a specific set of growth conditions which push (001)-islands to grow beyond the critical size and a shape instability might occur leading to the formation of a labyrinth of orthogonal extremely long (001)CGO nanowires, which can reach lengths of > 30 μm keeping their width < 90 nm.

The anisotropic shape of (011)-nanowires also corresponds to their equilibrium shape. Elongation in the direction of lowest misfit strain guaranties the minimization of E_{relax}; at the same time, this direction coincides with the enlargement of lowest surface energy facets and, thus, E_{surf} also favours rectangular shape. In this case, the decrease of the energy per unit volume of the system drives islands to continuously coarse and, as a result, to continuously elongate.

The analyses of all these results, and in particular those referring to (011)CGO nanowires, has gave us a set of strategies to follow in order to generate interfacial nanostructures with high lateral aspect ratios. Relaxation of elastic energy must favour elongation. In general, strained-islands might experience a shape-instability above a critical size D_c, which depends on the trade-off between strain and surface energies. In a biaxial anisotropic stressed system, E_{relax} favours elongation along lowest misfit direction since nucleation. On the other hand, surface energy cannot be a handicap for elongation. In a system with anisotropic surface energies, E_{surf} enhances energy since nucleation as well. We do not know if both conditions are essential. In fact, elongation of (001)-nanoislands has also been observed, but under special combination of growth conditions and in any case it is straightforward. If elongation along lowest misfit direction occurs simultaneously to enlargement of lowest surface energy facets, the driving force leading island's elongation is two-fold: minimization of E_{relax} and E_{surf} is simultaneously guaranteed. This is the key of the formation of extremely long (011)-nanowires in brief periods of time.

Furthermore, the energy per unit volume must continuously decrease as island's elongate, i.e. coarsening phenomena must as well instigate higher lateral aspect ratios so that elongation is continuously promoted. High atomic mobility is also important. Atoms have to

diffuse between islands, and arriving atoms must be able to move to islands' extremes leading to the elongation of the nanowire. Kinetic processes are linked to atomic mobility. We have based on high temperature treatments and high concentration of oxygen vacancies as two paths to enhance mobility. Particularly, we have succeeded to achieve ultrafast mobility through the enhancement of oxygen vacancies in CeO_2 structure by using reducing atmospheres and through Gd-doping. Structural dissimilarities between the fluorite CGO and the perovskite LAO also enhances high concentration of oxygen vacancies at the interface. Several coarsening mechanisms acting concurrently augment as well the rapid formation of long islands. Asymmetric Ostwald ripening, dynamic coalescence and static coalescence are some examples of coarsening processes identified in the systems with (011)CGO nanoislands. Finally, we have reported a non-common path to promote coarsening of interfacial nanoislands: existence of attractive interaction between nanoislands. Combination of tensile and compressive misfit strains in one island and resulting substrate distortions in substrate free regions adjacent to these islands have been signalled as a possible mechanism leading to such rareness and unusual phenomenology. This behaviour could explain the rapid and continuous formation of intricate nanolabyrinthine structures, as well as the formation of extremely long islands in such brief periods of time.

Whereas all these conditions apply satisfactory to the case of (011)CGO nanowires, they are not fulfilled by (001)CGO nanodots. Very large island's sizes are required in this case for the existence of a spontaneous shape-instability due to the isotropy of surface energies and biaxial isotropic stress. The thermodynamic stability of these islands has been suggested as the main cause of their lack of evolution. Moreover, the homogeneous and ordered distribution of (001)CGO nanodots in a single terrace suggest the existence of substrate-mediated repulsive interaction between islands and which would also act against coarsening.

In the last chapter, we have shown a potential application of these oxide nanostructured templates in the field of high temperature superconductors. They have been used as templates to grow YBCO thin films in order to improve the vortex pinning capabilities of these superconducting thin films. Let's notice that the investigation of the influence of artificial vortex pinning centres on the critical currents densities (J_c) of superconductors constitutes nowadays an issue of major interest. We have grown the YBCO films through the chemical route of MOD-TFA, leading to the generation of an all-chemically grown nanostructured superconductor. The interfacial nanostructured YBCO-TFA thin films prepared exhibit high critical current densities and no-degradation of the critical temperature, indicative of their good quality and proving the compatibility between chemically-derived nanostructured templates and YBCO-TFA thin films. The presence of interfacial nanoislands results into an increase of vortex pinning when the magnetic field is applied parallel to c-axis of the film, which results into a

better J_c in-field performance for H||c and an improvement of the irreversibility line for H||c. This effect is especially remarkable at high temperatures and high magnetic fields, and it is consequence of the improvement of the anisotropic-strong contribution to J_c for H||c in interfacial nanostructured YBCO-TFA films as compared to standard ones. This behaviour is attributed to an increase of the number of pre-existing extended defects for H||c. In contrast, our nanostructured samples exhibit a reduction of J_c at self-field for H||c with respect to standard YBCO-TFA films which is due to a reduction of isotropic-strong contribution. We have also observed a decrease of J_c for H||ab associated to a reduction of the J_c^{iso} as well as to reduction of J_c^{an} for H||ab. New processing parameters and strategies should be tested to keep these strong-isotropic defects while increasing the anisotropic ones. We have built up H-T vortex pinning diagrams where it is easily visualized the contributions to J_c of the distinct sorts of pinning centres in interfacial nanostructured and they can be compared to those in standard YBCO-TFA thin films. As a result, they enable us to propose the need of combined defects to further improve performance, especially at self-filed and intermediate temperatures as well as for H||ab.

Analyses of nanostructured YBCO-TFA films of different thickness have shown that the influence on vortex pinning for H||c becomes more important as thinner is the film, whereas the decrease of J_c(H||ab) also gets more pronounced with thickness reduction. These results indicate that the presence of interfacial nanoislands generate a sort of defects which are very effective for H||c but disrupt the pinning capabilities for H||ab. TEM analyses are required to determine the nature of defects generated by the interfacial oxide nanostructures.

Hence, in this work we have shown the possibility to prepare epitaxial interfacial self-assembled oxide nanostructures through the deposition of ultradiluted chemical solutions, which opens a new and attractive bottom-up low-cost fabrication route to large-scale nanostructuration. Oxide nanostructured templates are of high interest at present for the generation of new functionalities and devices in a large variety of fields such as ferroelectricity, ferromagnetism, photovoltaics, optics and, as it has been demonstrated, in superconductivity. Furthermore, let's remark that strategies shown for the generation of highly anisotropic interfacial nanoislands are not limited to oxides and, actually, they can be applied to a large variety of heteroepitaxial systems (semiconductors, metals, etc.).

References

[1] "*Small wonders* (a survey of nanotechnology)", in *The Economist*, (January, 2005).

[2] R. P. Feynman, *Engineering and Science* 23, 22 (1960).

[3] T. Ito and S. Okazaki, *Nature,* 406, 1027 (2000).

[4] Y. Xia, J. A. Rogers, K. E. Paul and G. M. Whitesides, *Chemical Reviews,* 99, 1823 (1999).

[5] J. Skar, *Philosophical Transactions of the Royal Society of London Series a-Mathematical Physical and Engineering Sciences,* 361, 1049 (2003).

[6] M. A. Kessler and B. T. Werner, *Science,* 299, 380 (2003).

[7] "Self-Assembled Nanostructures", Ed. (2006).

[8] H. Nishimori and N. Ouchi, *Physical Review Letters,* 71, 197 (1993).

[9] P. V. Coveney, *Philosophical Transactions of the Royal Society of London Series a-Mathematical Physical and Engineering Sciences,* 361, 1057 (2003).

[10] A. M. Turing, *Philosophical Transactions of the Royal Society of London Series B-Biological Sciences,* 237, 37 (1952).

[11] L. B. Freund and S. Suresh, "*Thin Film Materials: stress, defect formation and surface evolution"*. Cambridge University Press (2003).

[12] B. Voigtländer, *Surface Science Reports,* 43, 127 (2001).

[13] C. Teichert, *Physics Reports-Review Section of Physics Letters,* 365, 335 (2002).

[14] J. Stangl, V. Holy and G. Bauer, *Reviews of Modern Physics,* 76, 725 (2004).

[15] V. A. Shchukin and D. Bimberg, *Reviews of Modern Physics,* 71, 1125 (1999).

[16] D. L. Allara, *Nature,* 437, 638 (2005).

[17] O. E. Shklyaev, M. J. Beck, M. Asta, M. J. Miksis and P. W. Voorhees, *Physical Review Letters,* 94, 176102 (2005).

[18] S. Johansson, M. Christensen and G. Wahnstrom, *Physical Review Letters,* 95, 226108 (2005).

[19] G. Wulf, *Z. Kristallogr.,* 105, 449 (1901).

[20] C. Herring, *Physical Review,* 82, 87 (1951).

[21] F. Silly and M. R. Castell, *Physical Review Letters,* 94, 046103 (2005).

[22] F. C. Frank and J. H. van der Merwe, *Proceedings of the Royal Society of London*, Assadssa, 205 (1949).

[23] M. Volmer and A. Weber, *Z. Phys. Chem. ,* 119, 277 (1926).

[24] I. N. Stranski and L. Krastanow, *Sitzungsber. Akad. Wiss. Wien, Math.-Naturwiss Klasse* 146, 797 (1937).

[25] A. Rastelli, M. Stoffel, J. Tersoff, G. S. Kar and O. G. Schmidt, *Physical Review Letters,* 95, 026103 (2005).

[26] D. T. Tambe and V. B. Shenoy, *Applied Physics Letters,* 85, 1586 (2004).

[27] S. Christiansen, M. Albrecht, H. P. Strunk and H. J. Maier, *Applied Physics Letters,* 64, 3617 (1994).

[28] J. Tersoff and R. M. Tromp, *Physical Review Letters,* 70, 2782 (1993).

[29] P. Muller and R. Kern, *Surface Science,* 457, 229 (2000).

[30] Y. W. Mo, D. E. Savage, B. S. Swartzentruber and M. G. Lagally, *Physical Review Letters,* 65, 1020 (1990).

[31] J. A. Floro, G. A. Lucadamo, E. Chason, L. B. Freund, M. Sinclair, R. D. Twesten and R. Q. Hwang, *Physical Review Letters,* 80, 4717 (1998).

[32] G. Medeiros-Ribeiro, A. M. Bratkovski, T. I. Kamins, D. A. A. Ohlberg and R. S. Williams, *Science,* 279, 353 (1998).

[33] I. Goldfarb, L. Banks-Sills and R. Eliasi, *Physical Review Letters,* 97, 206101 (2006).

[34] I. Daruka, J. Tersoff and A. L. Barabasi, *Physical Review Letters,* 82, 2753 (1999).

[35] G. Costantini, A. Rastelli, C. Manzano, P. Acosta-Diaz, G. Katsaros, R. Songmuang, O. G. Schmidt, H. v. Känel and K. Kern, *Journal of Crystal Growth,* 278, 38 (2005).

[36] Y. Chen and J. Washburn, *Physical Review Letters,* 77, 4046 (1996).

[37] J. Tersoff and F. K. LeGoues, *Physical Review Letters,* 72, 3570 (1994).

[38] I. Goldfarb, *Surface Science,* 601, 2756 (2007).

[39] D. Vanderbilt and L. K. Wickham, "Elastic Relaxation Energies of Coherent Germanium Islands on Silicon," *Materials Research Society*, MRS Proceedings (1991).

[40] M. Meixner, E. Schöll, V. A. Shchukin and D. Bimberg, *Physical Review Letters,* 87, 236101 (2001).

[41] H. T. Johnson and L. B. Freund, *Journal of Applied Physics,* 81, 6081 (1997).

[42] O. L. Alerhand, D. Vanderbilt, R. D. Meade and J. D. Joannopoulos, *Physical Review Letters,* 61, 1973 (1988).

[43] V. I. Marchenko, *Sov. Phys. JETP Lett. ,* 33, 381 (1981).

[44] V. A. Shchukin, N. N. Ledentsov, P. S. Kop'ev and D. Bimberg, *Physical Review Letters,* 75, 2968 (1995).

[45] F. Liu, A. H. Li and M. G. Lagally, *Physical Review Letters,* 87, 126103 (2001).

[46] K. Pohl, M. C. Bartelt, J. de la Figuera, N. C. Bartelt, J. Hrbek and R. Q. Hwang, *Nature,* 397, 238 (1999).

[47] W. Ostwald, *Z. Phys. Chem.,* 22, 189 (1897).

[48] D. Beysens, C. M. Knobler and H. Schaffar, *Physical Review B,* 41, 9814 (1990).

[49] L. Bardotti, M. C. Bartelt, C. J. Jenks, C. R. Stoldt, J. M. Wen, C. M. Zhang, P. A. Thiel and J. W. Evans, *Langmuir,* 14, 1487 (1998).

[50] J. M. Wen, S. L. Chang, J. W. Burnett, J. W. Evans and P. A. Thiel, *Physical Review Letters,* 73, 2591 (1994).

[51] J. M. Wen, J. W. Evans, M. C. Bartelt, J. W. Burnett and P. A. Thiel, *Physical Review Letters,* 76, 652 (1996).

[52] K. Morgenstern, G. Rosenfeld, B. Poelsema and G. Comsa, *Physical Review Letters,* 74, 2058 (1995).

[53] T. Merdzhanova, A. Rastelli, M. Stoffel, S. Kiravittaya and O. G. Schmidt, *Journal of Crystal Growth,* 301-302, 319 (2007).

[54] J. Tersoff, B. J. Spencer, A. Rastelli and H. von Kanel, *Physical Review Letters,* 89, 196104 (2002).

[55] I. Daruka and A. L. Barabási, *Physical Review Letters,* 79, 3708 (1997).

[56] D. E. Jesson, G. Chen, K. M. Chen and S. J. Pennycook, *Physical Review Letters,* 80, 5156 (1998).

[57] S. Günther, E. Kopatzki, M. C. Bartelt, J. W. Evans and R. J. Behm, *Physical Review Letters,* 73, 553 (1994).

[58] M. G. Lagally and Z. Zhang, *Nature,* 417, 907 (2002).

[59] J. V. Barth, G. Costantini and K. Kern, *Nature,* 437, 671 (2005).

[60] R. E. Rudd, G. A. D. Briggs, A. P. Sutton, G. Medeiros-Ribeiro and R. S. Williams, *Physical Review Letters,* 90, 146101 (2003).

[61] F. M. Ross, J. Tersoff and R. M. Tromp, *Physical Review Letters,* 80, 984 (1998).

[62] D. Bimberg, N. Kirstaedter, N. N. Ledentsov, Z. I. Alferov, P. S. Kop'ev and V. M. Ustinov, *Selected Topics in Quantum Electronics, IEEE Journal of,* 3, 196 (1997).

[63] A. Barabasi, *Applied Physics Letters,* 70, 2565 (1997).

[64] H. Usui, H. Yasuda and H. Mori, *Journal of Materials Science-Materials in Electronics,* 19, 131 (2008).

[65] J. T. Robinson, D. A. Walko, D. A. Arms, D. S. Tinberg, P. G. Evans, Y. Cao, J. A. Liddle, A. Rastelli, O. G. Schmidt and O. D. Dubon, *Physical Review Letters,* 98, 106102 (2007).

[66] S. H. Brongersma, M. R. Castell, D. D. Perovic and M. Zinke-Allmang, *Physical Review Letters,* 80, 3795 (1998).

[67] S. Rousset, S. Chiang, D. E. Fowler and D. D. Chambliss, *Physical Review Letters,* 69, 3200 (1992).

[68] A. Li, F. Liu and M. G. Lagally, *Physical Review Letters,* 85, 1922 (2000).

[69] M. T. Middel, H. J. W. Zandvliet and B. Poelsema, *Physical Review Letters,* 88, (2002).

[70] V. A. Shchukin, T. P. Munt, D. E. Jesson and D. Bimberg, *Physical Review B,* 71, 113407 (2005).

[71] J. L. Gray, R. Hull and J. A. Floro, *Applied Physics Letters,* 85, 3253 (2004).

[72] H. Brune, M. Giovannini, K. Bromann and K. Kern, *Nature,* 394, 451 (1998).

[73] B. Voigtländer, G. Meyer and N. M. Amer, *Physical Review B,* 44, 10354 (1991).

[74] T. Yokoyama, S. Yokoyama, T. Kamikado, Y. Okuno and S. Mashiko, *Nature,* 413, 619 (2001).

[75] J. C. Jiang, L. L. Henry, K. I. Gnanasekar, C. L. Chen and E. I. Meletis, *Nano Letters,* 4, 741 (2004).

[76] J. C. Nie, H. Yamasaki and Y. Mawatari, *Physical Review B,* 70, 195421 (2004).

[77] I. Szafraniak, C. Harnagea, R. Scholz, S. Bhattacharyya, D. Hesse and M. Alexe, *Applied Physics Letters,* 83, 2211 (2003).

[78] H. Zheng, J. Wang, S. E. Lofland, Z. Ma, L. Mohaddes-Ardabili, T. Zhao, L. Salamanca-Riba, S. R. Shinde, S. B. Ogale, F. Bai, D. Viehland, Y. Jia, D. G. Schlom, M. Wuttig, A. Roytburd and R. Ramesh, *Science,* 303, 661 (2004).

[79] U. Lüders, F. Sánchez and J. Fontcuberta, *Physical Review B,* 70, 045403 (2004).

[80] E. Vasco, R. Dittmann, S. Karthauser and R. Waser, *Applied Physics Letters,* 82, 2497 (2003).

[81] A. Seifert, A. Vojta, J. S. Speck and F. F. Lange, *Journal of Materials Research,* 11, 1470 (1996).

[82] H. Nonomura, H. Fujisawa, M. Shimizu, H. Niu and K. Honda, *Japanese Journal of Applied Physics Part 1-Regular Papers Short Notes & Review Papers,* 43, 6539 (2004).

[83] R. Bachelet, S. Cottrino, G. Nahelou, V. Coudert, A. Boulle, B. Soulestin, F. Rossignol, R. Guinebretiere and A. Dauger, *Nanotechnology,* 18, 015301 (2007).

[84] M. Alexe, J. F. Scott, C. Curran, N. D. Zakharov, D. Hesse and A. Pignolet, *Applied Physics Letters,* 73, 1592 (1998).

[85] M. L. Calzada, M. Torres, L. E. Fuentes-Cobas, A. Mehta, J. Ricote and L. Pardo, *Nanotechnology,* 18, 375603 (2007).

[86] M. D. Rauscher, A. Boyne, S. A. Dregia and S. A. Akbar, *Advanced Materials,* 20, 1699 (2008).

[87] P. A. Langjahr, T. Wagner, F. F. Lange and M. Ruhle, *Journal of Crystal Growth,* 256, 162 (2003).

[88] P. A. Langjahr, T. Wagner, M. Ruhle and F. F. Lange, *Journal of Materials Research,* 14, 2945 (1999).

[89] V. C. Matijasevic, B. Ilge, B. Stäuble-Pümpin, G. Rietveld, F. Tuinstra and J. E. Mooij, *Physical Review Letters,* 76, 4765 (1996).

[90] G. Ketteler and W. Ranke, *Material Research Society, Symposium Proceedings,* 775, (2003).

[91] A. Roelofs, T. Schneller, K. Szot and R. Waser, *Applied Physics Letters,* 81, 5231 (2002).

[92] M. Dawber, I. Szafraniak, M. Alexe and J. F. Scott, *Journal of Physics-Condensed Matter,* 15, L667 (2003).

[93] I. Vrejoiu, M. Alexe, D. Hesse and U. Gösele, *Advanced Functional Materials,* 18, 3892 (2008).

[94] W. S. Kim, J. W. Kim, H. H. Park and H. N. Lee, *Japanese Journal of Applied Physics,* 39, 7097 (2000).

[95] M. Dawber, K. M. Rabe and J. F. Scott, *Reviews of Modern Physics,* 77, 1083 (2005).

[96] T. Tybell, P. Paruch, T. Giamarchi and J. M. Triscone, *Physical Review Letters,* 89, 097601 (2002).

[97] M. Coll, J. Gazquez, F. Sandiumenge, T. Puig, X. Obradors, J. P. Espinos and R. Huhne, *Nanotechnology,* 19, 395601 (2008).

[98] X. Obradors, T. Puig, A. Pomar, F. Sandiumenge, N. Mestres, M. Coll, A. Cavallaro, N. Roma, J. Gazquez, J. C. Gonzalez, O. Castano, J. Gutierrez, A. Palau, K. Zalamova, S. Morlens, A. Hassini, M. Gibert, S. Ricart, J. M. Moreto, S. Pinol, D. Isfort and J. Bock, *Superconductor Science & Technology,* 19, S13 (2006).

[99] R. W. Schwartz, *Chemistry of Materials,* 9, 2325 (1997).

[100] R. W. Schwartz, T. Schneller and R. Waser, *Comptes Rendus Chimie,* 7, 433 (2004).

[101] G. W. Scherer, *Journal of Sol-Gel Science and Technology,* 8, 353 (1997).

[102] T. Morrison and R. N. Boyd, "*Organic Chemistry"*. Allyn and Bacon, Inc., Boston (1974).

[103] C. Brinker and G. W. Scherer, "*Sol-Gel Science: The Physics and Chemistry of Sol-Gel Processing"*. Academic Press, New York (1990).

[104] P. K. Coffman and S. K. Dey, *Journal of Sol-Gel Science and Tecnology,* 1, 251 (1994).

[105] R. W. Schwartz, R. A. Assink and T. J. Headley, "Solution Chemistry Effects in PZT Thin Film Processing: Spectroscopic and Microstructural Characterization, in Ferroelectric Thin Films II," *Materials Research Society*, Symposium Proceedings 245 (1992).

[106] R. Roy, *Journal of the American Ceramic Society,* 52, 344 (1969).

[107] A. Ponchet, A. L. Corre, H. L. Haridon, B. Lambert and S. Salaun, *Applied Physics Letters,* 67, 1850 (1995).

[108] D. W. Greve, *Materials Science and Engineering B-Solid State Materials for Advanced Technology,* 18, 22 (1993).

[109] M. Hanke, M. Schmidbauer, R. Kohler, F. Syrowatka, A. K. Gerlitzke and T. Boeck, *Applied Physics Letters,* 84, 5228 (2004).

[110] M. Coll, J. Gazquez, A. Pomar, T. Puig, F. Sandiumenge and X. Obradors, *Physical Review B (Condensed Matter and Materials Physics),* 73, 075420 (2006).

[111] A. Seifert, F. F. Lange and J. S. Speck, *Journal of Materials Research,* 10, 680 (1995).

[112] C. Moreno, P. Abellán, A. Hassini, A. Ruyter, A. Pérez del Pino, F. Sandiumenge, J. Santiso, T. Puig and X. Obradors, *to be published*.

[113] C. Mary, R. Guinebretiere, G. Trolliard, B. Soulestin, P. Villechaize and A. Dauger, *Thin Solid Films,* 336, 156 (1998).

[114] S. Clemens, T. Schneller, A. van der Hart, F. Peter and R. Waser, *Advanced Materials,* 17, 1357 (2005).

[115] A. Crisan, S. Fujiwara, J. C. Nie, A. Sundaresan and H. Ihara, *Applied Physics Letters,* 79, 4547 (2001).

[116] J. C. Nie, H. Yamasaki, H. Yamada, Y. Nakagawa, K. Develos-Bagarinao and Y. Mawatari, *Superconductor Science & Technology,* 17, 845 (2004).

[117] P. Mele, K. Matsumoto, T. Horide, O. Miura, A. Ichinose, M. Mukaida, Y. Yoshida and S. Horii, *Superconductor Science & Technology,* 19, 44 (2006).

[118] J. Bardeen, L. N. Cooper and J. R. Schrieffer, *Physical Review,* 108, 1175 (1957).

[119] J. R. Waldram, "*Superconducting of Metals and Cuprates "*. Instiyut of Physics Publishing, London (1996).

[120] L. Y. Vinnikov, J. Karpinski, S. M. Kazakov, J. Jun, J. Anderegg, S. L. Bud'ko and P. C. Canfield, *Physical Review B,* 67, 092512 (2003).

[121] A. A. Abrikosov, *Soviet Physics Jetp-Ussr,* 5, (1957).

[122] G. Blatter, M. V. Feigel'man, V. B. Geshkenbein, A. I. Larkin and V. M. Vinokur, *Reviews of Modern Physics,* 66, 1125 (1994).

[123] M. P. A. Fisher, *Physical Review Letters,* 62, 1415 (1989).

[124] D. R. Nelson and V. M. Vinokur, *Physical Review B,* 48, 13060 (1993).

[125] A. Schilling, R. A. Fisher, N. E. Phillips, U. Welp, D. Dasgupta, W. K. Kwok and G. W. Crabtree, *Nature,* 382, 791 (1996).

[126] A. Soibel, E. Zeldov, M. Rappaport, Y. Myasoedov, T. Tamegai, S. Ooi, M. Konczykowski and V. B. Geshkenbein, *Nature,* 406, 282 (2000).

[127] J. Figueras, T. Puig, X. Obradors, W. K. Kwok, L. Paulius, G. W. Crabtree and G. Deutscher, *Nature Physics,* 2, 402 (2006).

[128] D. Larbalestier, A. Gurevich, D. M. Feldmann and A. Polyanskii, *Nature,* 414, 368 (2001).

[129] V. Breit, P. Schweiss, R. Hauff, H. Wühl, H. Claus, H. Rietschel, A. Erb and G. Müller-Vogt, *Physical Review B,* 52, R15727 (1995).

[130] U. Welp, W. K. Kwok, G. W. Crabtree, K. G. Vandervoort and J. Z. Liu, *Physical Review Letters,* 62, 1908 (1989).

[131] G. Blatter, V. B. Geshkenbein and A. I. Larkin, *Physical Review Letters,* 68, 875 (1992).

[132] S. R. Foltyn, L. Civale, J. L. MacManus-Driscoll, Q. X. Jia, B. Maiorov, H. Wang and M. Maley, *Nat Mater,* 6, (2007).

[133] M. W. Rupich, D. T. Verebelyi, W. Zhang, T. Kodenkandath and X. P. Li, *Mrs Bulletin,* 29, 572 (2004).

[134] B. Dam, J. M. Huijbregtse, F. C. Klaassen, R. C. F. van der Geest, G. Doornbos, J. H. Rector, A. M. Testa, S. Freisem, J. C. Martinez, B. Stauble-Pumpin and R. Griessen, *Nature,* 399, 439 (1999).

[135] J. Giapintzakis, W. C. Lee, J. P. Rice, D. M. Ginsberg, I. M. Robertson, R. Wheeler, M. A. Kirk and M. O. Ruault, *Physical Review B,* 45, 10677 (1992).

[136] L. Civale, A. D. Marwick, M. W. McElfresh, T. K. Worthington, A. P. Malozemoff, F. H. Holtzberg, J. R. Thompson and M. A. Kirk, *Physical Review Letters,* 65, 1164 (1990).

[137] R. B. van Dover, E. M. Gyorgy, L. F. Schneemeyer, J. W. Mitchell, K. V. Rao, R. Puzniak and J. V. Waszczak, *Nature,* 342, 55 (1989).

[138] L. Civale, A. D. Marwick, T. K. Worthington, M. A. Kirk, J. R. Thompson, L. Krusin-Elbaum, Y. Sun, J. R. Clem and F. Holtzberg, *Physical Review Letters,* 67, 648 (1991).

[139] T. Haugan, P. N. Barnes, R. Wheeler, F. Meisenkothen and M. Sumption, *Nature,* 430, 867 (2004).

[140] J. L. MacManus-Driscoll, S. R. Foltyn, Q. X. Jia, H. Wang, A. Serquis, L. Civale, B. Maiorov, M. E. Hawley, M. P. Maley and D. E. Peterson, *Nat Mater,* 3, 439 (2004).

[141] Y. Yamada, K. Takahashi, H. Kobayashi, M. Konishi, T. Watanabe, A. Ibi, T. Muroga, S. Miyata, T. Kato, T. Hirayama and Y. Shiohara, *Applied Physics Letters,* 87, 132502 (2005).

[142] S. Kang, A. Goyal, J. Li, A. A. Gapud, P. M. Martin, L. Heatherly, J. R. Thompson, D. K. Christen, F. A. List, M. Paranthaman and D. F. Lee, *Science,* 311, 1911 (2006).

[143] J. Hanisch, C. Cai, R. Huhne, L. Schultz and B. Holzapfel, *Applied Physics Letters,* 86, 122508 (2005).

[144] J. Gutierrez, A. Llordes, J. Gazquez, M. Gibert, N. Roma, S. Ricart, A. Pomar, F. Sandiumenge, N. Mestres, T. Puig and X. Obradors, *Nature Materials,* 6, 367 (2007).

[145] K. Matsumoto, T. Horide, K. Osamura, M. Mukaida, Y. Yoshida, A. Ichinose and S. Horii, *Physica C-Superconductivity and Its Applications,* 412-14, 1267 (2004).

[146] T. Aytug, M. Paranthaman, A. A. Gapud, S. Kang, H. M. Christen, K. J. Leonard, P. M. Martin, J. R. Thompson, D. K. Christen, R. Meng, I. Rusakova, C. W. Chu and T. H. Johansen, *Journal of Applied Physics,* 98, 114309 (2005).

[147] B. Maiorov, H. Wang, S. R. Foltyn, Y. Li, R. DePaula, L. Stan, P. N. Arendt and L. Civale, *Superconductor Science & Technology,* 19, 891 (2006).

[148] G. Binnig, C. F. Quate and C. Gerber, *Physical Review Letters,* 56, 930 (1986).

[149] "Scanning Probe Microscopy," in *Encyclopedia of Materials: Science and Technology*: Elsevier, 2005, pp. 1-12.

[150] M. G. Lagally and D. E. Savage, *MRS Bulletin,* 24 (January 1993).

[151] B. B. P. He, *Powder Diffraction,* 18, 71 (2003).

[152] K. Helming, M. Lyubchenko, B. He and U. Preckwinkel, *Powder Diffraction,* 18, 99 (2003).

[153] P. Abellán, *Tesina*, "Transmission Electron Microscopy study of nanostructured oxide templates grown by Metal-Organic Decomposition", ICMAB-CSIC, Universitat Autònoma de Barcelona (2008).

[154] C. P. Bean, *Physical Review Letters,* 8, 250 (1962).

[155] C. P. Bean, *Reviews of Modern Physics,* 36, 31 (1964).

[156] A. Sanchez and C. Navau, *Physical Review B,* 64, 214506 (2001).

[157] J. Gutierrez, *Thesis*, "Vortex pinning and critical currents in $YBa_2Cu_3O_{7-x}$ MOD-TFA thin films and Coated Conductors", ICMAB-CSIC, Universitat Autònoma de Barcelona (2008).

[158] J. M. Phillips, *Journal of Applied Physics,* 79, 1829 (1996).

[159] J. Garcia-Barriocanal, A. Rivera-Calzada, M. Varela, Z. Sefrioui, E. Iborra, C. Leon, S. J. Pennycook and J. Santamaria, *Science,* 321, 676 (2008).

[160] H. Zheng, Q. Zhan, F. Zavaliche, M. Sherburne, F. Straub, M. P. Cruz, L.-Q. Chen, U. Dahmen and R. Ramesh, *Nano Letters,* 6, 1401 (2006).

[161] A. Ohtomo and H. Y. Hwang, *Nature,* 427, 423 (2004).

[162] M. Basletic, J. L. Maurice, C. Carretero, G. Herranz, O. Copie, M. Bibes, E. Jacquet, K. Bouzehouane, S. Fusil and A. Barthelemy, *Nat Mater,* 7, 621 (2008).

[163] T. Terashima, K. Iijima, K. Yamamoto, K. Hirata, Y. Bando and T. Takada, *Japanese Journal of Applied Physics Part 2-Letters,* 28, L987 (1989).

[164] M. Kawasaki, K. Takahashi, T. Maeda, R. Tsuchiya, M. Shinohara, O. Ishiyama, T. Yonezawa, M. Yoshimoto and H. Koinuma, *Science,* 266, 1540 (1994).

[165] J. M. Huijbregtse, J. H. Rector and B. Dam, *Physica C,* 351, 183 (2001).

[166] B. Dam, J. M. Huijbregtse and J. H. Rector, *Physical Review B,* 65, 064528 (2002).

[167] Y. S. Kim, D. J. Kim, T. H. Kim, T. W. Noh, J. S. Choi, B. H. Park and J. G. Yoon, *Applied Physics Letters,* 91, 042908 (2007).

[168] R. A. McKee, F. J. Walker and M. F. Chisholm, *Science,* 293, 468 (2001).

[169] J. Fompeyrine, R. Berger, H. P. Lang, J. Perret, E. Machler, C. Gerber and J. P. Locquet, *Applied Physics Letters,* 72, 1697 (1998).

[170] D. H. Lowndes, D. K. Christen, C. E. Klabunde, Z. L. Wang, D. M. Kroeger, J. D. Budai, S. Zhu and D. P. Norton, *Physical Review Letters,* 74, 2355 (1995).

[171] H. Schneidewind, M. Manzel, G. Bruchlos and K. Kirsch, *Superconductor Science & Technology,* 14, 200 (2001).

[172] D. W. Kim, D. H. Kim, B. S. Kang, T. W. Noh, D. R. Lee and K. B. Lee, *Applied Physics Letters,* 74, 2176 (1999).

[173] B. M. Yen and H. Chen, *Journal of Applied Physics,* 85, 853 (1999).

[174] S. Geller and V. B. Bala, *Acta Crystallographica,* 9, 1019 (1956).

[175] S. Bueble, K. Knorr, E. Brecht and W. W. Schmahl, *Surface Science,* 400, 345 (1998).

[176] C. H. Kim, S. Y. Cho, I. T. Kim, W. J. Cho and K. S. Hong, *Materials Research Bulletin,* 36, 1561 (2001).

[177] J. P. Jacobs, M. A. S. Miguel and L. J. Alvarez, *Journal of Molecular Structure: THEOCHEM,* 390, 193 (1997).

[178] G. W. Berkstresser, A. J. Valentino and C. D. Brandle, *Journal of Crystal Growth,* 109, 467 (1991).

[179] C. H. Kim, J. W. Jang, S. Y. Cho, I. T. Kim and K. S. Hong, *Physica B,* 262, 438 (1999).

[180] J. Yao, P. B. Merrill, S. S. Perry, D. Marton and J. W. Rabalais, *Journal of Chemical Physics,* 108, 1645 (1998).

[181] A. Cavallaro, O. Castano, A. Palau, J. C. Gonzalez, M. D. Rossell, T. Puig, F. Sandiumenge, N. Mestres, S. Pinol and X. Obradors, *Journal of the European Ceramic Society,* 24, 1831 (2004).

[182] A. Cavallaro, F. Sandiumenge, J. Gazquez, T. Puig, X. Obradors, J. Arbiol and H. C. Freyhardt, *Advanced Functional Materials,* 16, 1363 (2006).

[183] F. Sandiumenge, A. Cavallaro, J. Gazquez, T. Puig, X. Obradors, J. Arbiol and H. C. Freyhardt, *Nanotechnology,* 16, 1809 (2005).

[184] M. Coll, *Thesis*, "Chemical Solution Deposition of Oxide Buffer and Superconducting Layers for $YBa_2Cu_3O_7$ Coated Conductors", ICMAB-CSIC, Universitat Autònoma de Barcelona (2007).

[185] A. Cavallaro, *Thesis*, "Optimisation of CSD buffer layers for $YBa_2Cu_3O_7$ coated conductors development", ICMAB-CSIC, Universitat Autònoma de Barecelona (2005).

[186] H. Fuji, R. Teranishi, Y. Kito, J. Matsuda, K. Nakaoka, T. Izumi, Y. Shiohara, Y. Yamada, A. Yajima and T. Saitoh, *Physica C-Superconductivity and Its Applications,* 426, 938 (2005).

[187] A. Gupta, R. Jagannathan, E. I. Cooper, E. A. Giess, J. I. Landman and B. W. Hussey, *Applied Physics Letters,* 52, 2077 (1988).

[188] N. Romà, S. Morlens, S. Ricart, K. Zalamova, J. M. Moretó, A. Pomar, T. Puig and X. Obradors, *Superconductor Science & Technology,* 19, 521 (2006).

[189] T. I. Kamins, E. C. Carr, R. S. Williams and S. J. Rosner, *Journal of Applied Physics,* 81, 211 (1997).

[190] M. Hammar, F. K. LeGoues, J. Tersoff, M. C. Reuter and R. M. Tromp, *Surface Science,* 349, 129 (1996).

[191] H. Hu, H. J. Gao and F. Liu, *Physical Review Letters,* 101, 216102 (2008).

[192] Y. J. Kim, Y. Gao, G. S. Herman, S. Thevuthasan, W. Jiang, D. E. McCready and S. A. Chambers, *Journal of Vacuum Science & Technology a-Vacuum Surfaces and Films,* 17, 926 (1999).

[193] "Interfaces in High-T_c superconducting systems", Ed. S. L. Shindé and D. A. Rudam, New York (1994).

[194] J. Narayan and B. C. Larson, *Journal of Applied Physics,* 93, 278 (2003).

[195] S. N. Jacobsen, U. Helmersson, R. Erlandsson, B. Skarman and L. R. Wallenberg, *Surface Science,* 429, 22 (1999).

[196] S. M. Haile, G. Staneff and K. H. Ryu, *Journal of Materials Science,* 36, 1149 (2001).

[197] L. S. Cavalcante, J. C. Sczancoski, V. M. Longo, F. S. De Vicente, J. R. Sambrano, A. T. de Figueiredo, C. J. Dalmaschio, M. S. Li, J. A. Varela and E. Longo, *Optics Communications,* 281, 3715 (2008).

[198] R. Vassen, X. Q. Cao, F. Tietz, D. Basu and D. Stover, *Journal of the American Ceramic Society,* 83, 2023 (2000).

[199] J. J. Urban, W. S. Yun, Q. Gu and H. Park, *Journal of the American Chemical Society,* 124, 1186 (2002).

[200] F. Sanchez, G. Herranz, I. C. Infante, J. Fontcuberta, M. V. Garcia-Cuenca, C. Ferrater and M. Varela, *Applied Physics Letters,* 85, 1981 (2004).

[201] J. L. MacManus-Driscoll, P. Zerrer, H. Y. Wang, H. Yang, J. Yoon, A. Fouchet, R. Yu, M. G. Blamire and Q. X. Jia, *Nature Materials,* 7, 314 (2008).

[202] Y.-M. Chiang, D. P. Birnie and W. D. Kingery, "*Physical Ceramics: Principles for Ceramic Science and Engineering"*. Wiley, John & Sons, Incorporated (1996).

[203] M. Ohring, "*The Materials Science of Thin Films "*. Academic Press (2002).

[204] P. G. Sundell, M. E. Bjorketun and G. Wahnstrom, *Physical Review B,* 73, (2006).

[205] T. Norby and Y. Larring, *Current Opinion in Solid State & Materials Science,* 2, 593 (1997).

[206] A. S. Patnaik and A. V. Virkar, *Journal of the Electrochemical Society,* 153, A1397 (2006).

[207] P. Babilo and S. M. Haile, *Journal of the American Ceramic Society,* 88, 2362 (2005).

[208] A. M. Azad, S. Subramaniam and T. W. Dung, *Journal of Alloys and Compounds,* 334, 118 (2002).

[209] S. S. Pandit, A. Weyl and D. Janke, *Solid State Ionics,* 69, 93 (1994).

[210] P. G. Sundell, M. E. Bjorketun and G. Wahnstrom, *Physical Review B,* 73, 104112 (2006).

[211] J. Padilla and D. Vanderbilt, *Physical Review B,* 56, 1625 (1997).

[212] J. Padilla and D. Vanderbilt, *Surface Science,* 418, 64 (1998).

[213] R. I. Eglitis, *Journal of Physics-Condensed Matter,* 19, 356004 (2007).

[214] P. A. Langjahr, F. F. Lange, T. Wagner and M. Ruhle, *Acta Materialia,* 46, 773 (1998).

[215] A. Pomar, M. Coll, A. Cavallaro, J. Gazquez, J. C. Gonzalez, N. Mestres, F. Sandiumenge, T. Puig and X. Obradors, *Journal of Materials Research,* 21, 1106 (2006).

[216] A. Li, F. Liu, D. Y. Petrovykh, J. L. Lin, J. Viernow, F. J. Himpsel and M. G. Lagally, *Physical Review Letters,* 85, 5380 (2000).

[217] J. De la Figuera, M. A. Huerta-Garnica, J. E. Prieto, c. Ocal and R. Miranda, *Applied Physics Letters,* 66, 1006 (1995).

[218] B. Yang, F. Liu and M. G. Lagally, *Physical Review Letters,* 92, 025502 (2004).

[219] T. I. Kamins and R. S. Williams, *Applied Physics Letters,* 71, 1201 (1997).

[220] A. Pascale, I. Berbezier, A. Ronda and P. C. Kelires, *Physical Review B,* 77, 075311 (2008).

[221] Z. Zhong, A. Halilovic, M. Mühlberger, F. Schäffler and G. Bauer, *Journal of Applied Physics,* 93, 6258 (2003).

[222] J. Zabaleta, *Tesina*, "Autoensamblaje dirigido de nanoestructuras de $Ce_{0.9}Gd_{0.1}O_{2-y}$ crecidas por vía química sobre sustratos nanoindentados", ICMAB-CSIC, Universitat Autònoma de Barcelona (2008).

[223] M. Mogensen, N. M. Sammes and G. A. Tompsett, *Solid State Ionics,* 129, 63 (2000).

[224] A. Trovarelli, *Catalysis Reviews-Science and Engineering,* 38, 439 (1996).

[225] A. H. Morshed, M. E. Moussa, S. M. Bedair, R. Leonard, S. X. Liu and N. ElMasry, *Applied Physics Letters,* 70, 1647 (1997).

[226] C. T. Campbell and C. H. F. Peden, *Science,* 309, 713 (2005).

[227] D. Barreca, A. Gasparotto, C. Maccato, C. Maragno, E. Tondello, E. Comini and G. Sberveglieri, *Nanotechnology,* 18, 125502 (2007).

[228] P. L. Chen and I. W. Chen, *Journal of the American Ceramic Society,* 79, 1793 (1996).

[229] P. L. Chen and W. Chen, *Journal of the American Ceramic Society,* 77, 2289 (1994).

[230] T. H. Etsell and S. N. Flengas, *Chemical Reviews,* 70, 339 (1970).

[231] S. R. Wang, H. Inaba, H. Tagawa, M. Dokiya and T. Hashimoto, *Solid State Ionics,* 107, 73 (1998).

[232] K. Knoth, B. Schlobach, R. Huhne, L. Schultz and B. Holzapfel, *Physica C-Superconductivity and Its Applications,* 426, 979 (2005).

[233] D. X. Huang, C. L. Chen and A. J. Jacobson, *Journal of Applied Physics,* 97, 043506 (2005).

[234] G. Hass, J. B. Ramsey and R. Thun, *Journal of the Optical Society of America,* 49, 116 (1959).

[235] T. Mahalingam, M. Radhakrishnan and C. Balasubramanian, *Thin Solid Films,* 78, 229 (1981).

[236] S. S. Kale, K. R. Jadhav, P. S. Patil, T. P. Gujar and C. D. Lokhande, *Materials Letters,* 59, 3007 (2005).

[237] Y. H. Wu, M. Y. Yang, A. Chin, W. J. Chen and C. M. Kwei, *Ieee Electron Device Letters,* 21, 341 (2000).

[238] X. K. Zhang, A. B. Walters and M. A. Vannice, *Applied Catalysis B-Environmental,* 4, 237 (1994).

[239] Y. M. Gao, P. Wu, K. Dwight and A. Wold, *Journal of Solid State Chemistry,* 90, 228 (1991).

[240] M. Nieminen, M. Putkonen and L. Niinisto, *Applied Surface Science,* 174, 155 (2001).

[241] E. P. Murray, T. Tsai and S. A. Barnett, *Nature,* 400, 649 (1999).

[242] A. Corma, P. Atienzar, H. Garcia and J. Y. Chane-Ching, *Nature Materials,* 3, 394 (2004).

[243] D. P. Norton, A. Goyal, J. D. Budai, D. K. Christen, D. M. Kroeger, E. D. Specht, Q. He, B. Saffian, M. Paranthaman, C. E. Klabunde, D. F. Lee, B. C. Sales and F. A. List, *Science,* 274, 755 (1996).

[244] R. D. Shannon and C. T. Prewitt, *Acta Crystallographica Section B-Structural Crystallography and Crystal Chemistry,* B 25, 925 (1969).

[245] J. W. Matthews, "*Epitaxial Growth, Part B"*. Academic Press, New York (1975).

[246] P. A. Langjahr, F. F. Lange, T. Wagner and M. Rühle, *Acta Materialia,* 44, 773 (1998).

[247] T. X. T. Sayle, S. C. Parker and C. R. A. Catlow, *Surface Science,* 316, 329 (1994).

[248] J. C. Conesa, *Surface Science,* 339, 337 (1995).

[249] C. Noguera, *Journal of Physics-Condensed Matter,* 12, R367 (2000).

[250] C. Noguera, "*Physics and Chemistry at Oxide Surfaces"*. Cambridge University Press (1996).

[251] W. D. Callister, "*Fundamentals of Materials Science and Engineering"*. John Wiley & Sons, Inc. Danvers (2005).

[252] K. Creath and J. C. Wyant, "Moiré and Fringe Projection Techniques", in *Optical Shop Testing*, John Wiley & Sons, (1992).

[253] M. A. Arranz, B. Holzapfel, N. Reger, J. Eickemeyer and L. Schultz, *Physica C,* 366, 109 (2002).

[254] S. H. Overbury, D. R. Huntley, D. R. Mullins, K. S. Ailey and P. V. Radulovic, *Journal of Vacuum Science & Technology a-Vacuum Surfaces and Films,* 15, 1647 (1997).

[255] Y. Gao, G. S. Herman, S. Thevuthasan, C. H. F. Peden and S. A. Chambers, *Journal of Vacuum Science & Technology A,* 17, 961 (1999).

[256] A. N. Khodan, J. P. Contour, D. Michel, O. Durand, R. Lyonnet and M. Mihet, *Journal of Crystal Growth,* 209, 828 (2000).

[257] T. Yamada, N. Wakiya, K. Shinozaki and N. Mizutani, *Applied Physics Letters,* 83, 4815 (2003).

[258] M. Gibert, T. Puig, X. Obradors, A. Benedetti, F. Sandiumenge and R. Hühne, *Advanced Materials,* 19, 3937 (2007).

[259] F. Patella, F. Arciprete, E. Placidi, S. Nufris, M. Fanfoni, A. Sgarlata, D. Schiumarini and A. Balzarotti, *Applied Physics Letters,* 81, 2270 (2002).

[260] P. Gambardella, M. Blanc, H. Brune, K. Kuhnke and K. Kern, *Physical Review B,* 61, 2254 (2000).

[261] S. Funaki, Y. Yoshida, Y. Ichino, M. Miura, Y. Takai, K. Matsumoto, A. Ichinose, M. Mukaida and S. Horii, *Physica C,* 463, (2007).

[262] F. Silly, A. C. Powell, M. G. Martin and M. R. Castell, *Physical Review B,* 72, 165403 (2005).

[263] R. Teranishi, J. Matsuda, K. Nakaoka, T. Izumi, Y. Shiohara, N. Mori and M. Mukaida, *Ieee Transactions on Applied Superconductivity,* 17, 3317 (2007).

[264] P. Zeppenfeld, M. Krzyzowski, C. Romainczyk, G. Comsa and M. G. Lagally, *Physical Review Letters,* 72, 2737 (1994).

[265] T. Maekawa, K. Kurosaki and S. Yamanaka, *Journal of Alloys and Compounds,* 416, 214 (2006).

[266] T. Maekawa, K. Kurosaki and S. Yamanaka, *Journal of Alloys and Compounds,* 407, 44 (2006).

[267] S. Yamanaka, T. Maekawa, H. Muta, T. Matsuda, S. Kobayashi and K. Kurosaki, *Journal of Alloys and Compounds,* 381, 295 (2004).

[268] W. Ma, D. E. Mack, R. Vassen and D. Stover, *Journal of the American Ceramic Society,* 91, 2630 (2008).

[269] N. C. Bartelt, R. M. Tromp and E. D. Williams, *Physical Review Letters,* 73, 1656 (1994).

[270] D. C. Schlößer, L. K. Verheij, G. Rosenfeld and G. Comsa, *Physical Review Letters,* 82, 3843 (1999).

[271] F. Silly and M. R. Castell, *Physical Review Letters,* 96, 086104 (2006).

[272] F. Silly and M. R. Castell, *Applied Physics Letters,* 87, 063106 (2005).

[273] D. Bimberg, M. Grundmann, N. N. Ledentsov, S. S. Ruvimov, P. Werner, U. Richter, J. Heydenreich, V. M. Ustinov, P. S. Kopev and Z. I. Alferov, *Thin Solid Films,* 267, 36 (1995).

[274] M. Iwatsuki, T. Sato and Y. Yamamoto, *Applied Surface Science,* 92, 321 (1996).

[275] B. C. Harrison and J. J. Boland, *Surface Science,* 594, 93 (2005).

[276] H. L. Marsh, D. S. Deak, F. Silly, A. I. Kirkland and M. R. Castell, *Nanotechnology,* 17, 3543 (2006).

[277] J. Broekmaat, A. Brinkman, D. H. A. Blank and G. Rijnders, *Applied Physics Letters,* 92, 043102 (2008).

[278] D. D. Vvedensky, *Journal of Physics-Condensed Matter,* 16, R1537 (2004).

[279] P. W. Anderson, *Physical Review Letters,* 9, 309 (1962).

[280] P. W. Anderson and Y. B. Kim, *Reviews of Modern Physics,* 36, 39 (1964).

[281] "Basic Research Needs in Superconductivity, Report on the Basic Energy Sciences Workshop on Superconductivity", http://www.sc.doe.gov/bes/reports/files/SC_rpt.pdf (2006)

[282] K. Traito, M. Peurla, H. Huhtinen, Y. P. P. Stepanov, M. Safonchik, Y. Y. Tse, P. Paturi and R. Laiho, *Physical Review B (Condensed Matter and Materials Physics),* 73, 224522 (2006).

[283] P. Mele, K. Matsumoto, T. Horide, A. Ichinose, M. Mukaida, Y. Yoshida, S. Horii and R. Kita, *Superconductor Science & Technology,* 21, 032002 (2008).

[284] C. V. Varanasi, J. Burke, L. Brunke, H. Wang, M. Sumption and P. N. Barnes, *Journal of Applied Physics,* 102, (2007).

[285] A. A. Gapud, D. Kumar, S. K. Viswanathan, C. Cantoni, M. Varela, J. Abiade, S. J. Pennycook and D. K. Christen, *Superconductor Science & Technology,* 18, 1502 (2005).

[286] C. Cai, B. Holzapfel, J. Hanisch, L. Fernandez and L. Schultz, *Applied Physics Letters,* 84, 377 (2004).

[287] J. L. MacManus-Driscoll, S. R. Foltyn, Q. X. Jia, H. Wang, A. Serquis, B. Maiorov, L. Civale, Y. Lin, M. E. Hawley, M. P. Maley and D. E. Peterson, *Applied Physics Letters,* 84, 5329 (2004).

[288] T. Aytug, M. Paranthaman, K. J. Leonard, S. Kang, P. M. Martin, L. Heatherly, A. Goyal, A. O. Ijaduola, J. R. Thompson, D. K. Christen, R. Meng, I. Rusakova and C. W. Chu, *Physical Review B* 74, 184505 (2006).

[289] S. Engel, T. Thersleff, R. Huhne, L. Schultz and B. Holzapfel, *Applied Physics Letters,* 90, 102505 (2007).

[290] P. Mele, K. Matsumoto, T. Horide, O. Miura, A. Ichinose, M. Mukaida, Y. Yoshida and S. Horii, *Physica C-Superconductivity and Its Applications,* 445, 648 (2006).

[291] J. C. Nie, H. Yamasaki, H. Yamada, K. Develos-Bagarinao, Y. Nakagawa and Y. Mawatari, *Physica C: Superconductivity,* 412-414, 1272 (2004).

[292] H. Wang, S. R. Foltyn, P. N. Arendt, Q. X. Jia, J. L. MacManus-Driscoll, L. Stan, Y. Li, X. Zhang and P. C. Dowden, *Journal of Materials Research,* 19, 1869 (2004).

[293] J. Gutierrez, T. Puig and X. Obradors, *Applied Physics Letters,* 90, 162514 (2007).

[294] T. Puig, J. Gutierrez, A. Pomar, A. Llordes, J. Gazquez, S. Ricart, F. Sandiumenge and X. Obradors, *Superconductor Science & Technology,* 21, 034008 (2008).

[295] C. J. van der Beek, M. Konczykowski, A. Abal'oshev, I. Abal'osheva, P. Gierlowski, S. J. Lewandowski, M. V. Indenbom and S. Barbanera, *Physical Review B,* 66, 024523 (2002).

[296] F. C. Klaassen, G. Doornbos, J. M. Huijbregtse, R. C. F. van der Geest, B. Dam and R. Griessen, *Physical Review B,* 64, 184523 (2001).

[297] A. M. Campbell and J. E. Evetts, *Advances in Physics,* 21, 199 (1972).

[298] T. G. Holesinger, L. Civale, B. Maiorov, D. M. Feldmann, J. Y. Coulter, D. J. Miller, V. A. Maroni, Z. Chen, D. C. Larbalestier, R. Feenstra, X. Li, Y. Huang, T. Kodenkandath, W. Zhang, M. W. Rupich and A. P. Malozemoff, *Advanced Materials,* 20, 391 (2008).

[299] A. Palau, T. Puig, J. Gutierrez, X. Obradors and F. de la Cruz, *Physical Review B,* 73, (2006).

[300] A. O. Ijaduola, J. R. Thompson, R. Feenstra, D. K. Christen, A. A. Gapud and X. Song, *Physical Review B (Condensed Matter and Materials Physics),* 73, 134502 (2006).

[301] D. M. Feldmann, O. Ugurlu, B. Maiorov, L. Stan, T. G. Holesinger, L. Civale, S. R. Foltyn and Q. X. Jia, *Applied Physics Letters,* 91, 162501 (2007).

[302] Y. N. Ovchinnikov and B. I. Ivlev, *Physical Review B,* 43, 8024 (1991).

[303] L. Civale, B. Maiorov, A. Serquis, S. R. Foltyn, Q. X. Jia, P. N. Arendt, H. Wang, J. O. Willis, J. Y. Coulter, T. G. Holesinger, J. L. MacManus-Driscoll, M. W. Rupich, W. Zhang and X. Li, *Physica C-Superconductivity and Its Applications,* 412-14, 976 (2004).

[304] L. Civale, B. Maiorov, J. L. MacManus-Driscoll, H. Wang, T. G. Holesinger, S. R. Foltyn, A. Serquis and R. N. Arendt, *Ieee Transactions on Applied Superconductivity,* 15, 2808 (2005).

[305] M. Tachiki and S. Takahashi, *Solid State Communications,* 72, 1083 (1989).

[306] J. Figueras, T. Puig, X. Obradors, R. J. Olsson, W. K. Kwok and G. W. Crabtree, *Superconductor Science & Technology,* 21, 025002 (2008).

[307] A. Díaz, L. Mechin, P. Berghuis and J. E. Evetts, *Physical Review Letters,* 80, 3855 (1998).

[308] L. Civale, B. Maiorov, A. Serquis, J. O. Willis, J. Y. Coulter, H. Wang, Q. X. Jia, P. N. Arendt, J. L. MacManus-Driscoll, M. P. Maley and S. R. Foltyn, *Applied Physics Letters,* 84, 2121 (2004).

[309] L. Civale, B. Maiorov, A. Serquis, J. O. Willis, J. Y. Coulter, H. Wang, Q. X. Jia, P. N. Arendt, M. Jaime, J. L. MacManus-Driscoll, M. P. Maley and S. R. Foltyn, *Journal of Low Temperature Physics,* 135, 87 (2004).

[310] H. Hilgenkamp and J. Mannhart, *Reviews of Modern Physics,* 74, 485 (2002).